Grinding of Cement Clinkers: Linking Multi-Scale Fracture Properties to System Chemistry, Mineralogy and Microstructure

by

William Wilson

Bachelier en génie civil de l'Université de Sherbrooke (2009)
Maître ès sciences en génie civil de l'Université de Sherbrooke (2011)

Submitted to the Department of Civil and Environmental Engineering
in partial fulfillment of the requirements for the degree of

Master of Science in Civil and Environmental Engineering

at the

MASSACHUSETTS INSTITUTE OF TECHNOLOGY

June 2013

Signature of Author .....
Department of Civil and Environmental Engineering
May 1, 2013

Certified by .....
Franz-Josef Ulm
Professor of Civil and Environmental Engineering
Thesis Supervisor

Accepted by .....
Heidi M. Nepf
Chair, Departmental Committee for Graduate Students

Grinding of Cement Clinkers: Linking Multi-Scale Fracture Properties to System Chemistry, Mineralogy and Microstructure

by

William Wilson

Submitted to the Department of Civil and Environmental Engineering
on May 1, 2013, in partial fulfillment of the
requirements for the degree of
Master of Science in Civil and Environmental Engineering

Abstract

Growing environmental concerns encourage the cement industry to improve its environmental performance, which in turn renews the interest in clinker grinding efficiency. Current knowledge on clinker grinding was built over the past decades, but contributions from fracture mechanics remained limited. This research aimed to contribute to this field by investigating industrial clinkers with innovative techniques such as multi-scale microscratching and statistical electron-probe microanalysis (EPMA). Microstructure investigations were first performed with scanning electron microscopy (SEM), and three characteristic length scales were defined for clinkers: the nodules at the macroscale, the clinker matrix and porosity at the intermediate scale, and the clinker phases at the microscale. A statistical EPMA method was developed to allow simultaneous determination of the clinker bulk chemistry, the chemistry of the clinker phases, and their abundance. The microscratch test method was downscaled to measure the fracture properties at each characteristic scale of clinkers. Measurements on single silicate grains provided access to the intrinsic fracture toughness, which was three to four time lower than the macroscale fracture toughness. A combination of microstructure effects and toughening mechanisms (crack deflection, crack tip shielding by microcracks, crack trapping, and crack pinning) explained this behavior. Comparison of industrial clinkers showed that higher macroscale toughness (i.e., poor coarse grindability) was associated with oversized alite crystals, which was explained by the increase of microcracks toughening with larger grain size. In contrast, lower macroscale fracture toughness (i.e., better coarse grindability) was associated with either poorly burned clinkers showing excessive porosity or well burned clinkers having a good repartition of small silicates. However, difficulties in fine grinding were expected for the poorly burned clinkers because of the increased amounts of clustered belite. Overall, this thesis presents new experimental methods to investigate clinkers, as well as links between clinkers properties and grindability, both of which hold interest to the scientific community and the cement industry.

Thesis Supervisor: Franz-Josef Ulm
Title: Professor of Civil and Environmental Engineering

Contents

List of Figures

List of Tables

Acknowledgments

First, I would like to thank Prof. Franz-Josef Ulm for providing me with the opportunity to pursue this degree in his team and for his continuous support. I am also very thankful to Dr. Konrad J. Krakowiak for his guidance in this project, his will to push my learning further and his essential role in our laboratory.

I would also like to acknowledge the financial support of the CSHub@MIT, with sponsorship provided by the Portland Cement Association (PCA) and the Ready Mixed Concrete (RMC) Research & Education Foundation. I am very grateful for this support.

This multi-technique experimental project was made possible by the precious collaboration of experts in different fields and I am greatly thankful for their availability and contributions to my work. Dr. Scott Speakman at the MIT Center for Materials Science and Engineering (CMSE) has been for me an invaluable resource with respect to X-ray diffraction and Rietveld refinements. Dr. Shiahn Chen and Patrick Boisvert guided me in the electron facility (CMSE), sharing their knowledge in order to optimize my analyses. Dr. Nilanjan Chatterjee (Department of Earth, Atmospheric, and Planetary Sciences) contributed to this work with his knowledge on electron probe microanalyses. Ange-Therese Akono was our reference for the scratch test, providing inputs and ideas to overcome certain difficulties. To all of you, thank you for your contributions to this work.

I would also like to thank my colleagues and friends of the research group for adding a great social aspect to my experience at MIT. Special thanks also go to Nicolas and Christian for the discussions and inputs on this project, as well as to Christian and Dieter who helped proof-read this thesis.

Finally, my deepest gratitude goes to my family, and especially to my wife Kristell and my daughter Claire. They were always there for me, bringing happiness in each and every day. This was a key factor of success, thank you for guiding me into a balanced and efficient life.

Part I

General Presentation

Chapter 1

Introduction

1.1 Industrial Context

In modern societies, concrete has become an essential construction material because of its unique properties such as workability, strength and durability. Thus, Portland cement, the main reactive ingredient of concrete, has been produced at an increasingly fast rate over the past century, as shown in Fig. 1.1. In addition, estimates indicate that world cement production will continue to grow until at least 2050, because of rapid economic growth in Asia and expected growth of other emerging countries [56].

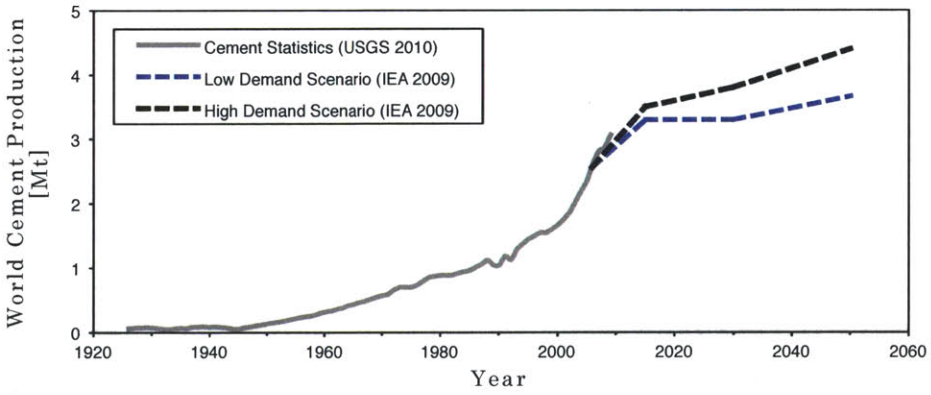

Fig. 1.1. History of world cement production [127] and future estimates scenarios [56]. The impressive growth observed in the last century is expected to continue until at least 2050.

At the same time, the cement industry is facing the challenge of reducing its environmental footprint, as cement production accounts each year for approximately 5% of global man-made CO_2 emissions [56]. As part of a global approach to address this issue, a topic of interest is the optimization of energy efficiency in the process of clinker grinding.

To obtain reactive cement, hard cement clinkers produced in cement kilns must be ground from nodules of several centimeters into a fine powder. Standard specification for Portland cements (types I to V) requires the fineness to be higher than 280 m^2/kg, as measured with the Blaine air permeability apparatus [10]. A recent survey [14] showed that U.S. producers are grinding most cements even finer to approximately 380 m^2/kg (and up to 550 m^2/kg for high early strength type III cements), which corresponds to 95% of particles being smaller than 45 μm (up to 98% for type III cements).

This intensive grinding process accounts for roughly one third of the approximately 100 kWh electrical energy required for the production of each ton of cement [107]. In addition, it has been shown that overall efficiency of grinding is between 1% and 5%: almost all energy is lost in heat, and only a very small percentage is directly used for particle size reduction [107]. Thus, improvement in clinker grinding and reduction in energy consumption is of high interest for the cement industry.

1.2 Research Objectives

Over the past decades, several publications were devoted to clinker grinding [52,51,107,119,53,91,74,130,112,92,77,42,123], and this resulted in efficiency improvements at the industrial cement plants. The vast majority of these studies aimed at establishing relationships between clinker characteristics and grinding energy. Some studies were dedicated to new grinding technologies, and a few were focused on fracture mechanisms of clinkers. In a recent publication on sustainable cement production, Schneider et al. [107] indicate that "certainly, fracture mechanics has not given sufficient understanding with respect to clinker and other cement constituents."

Thus, this current study aims to improve the understanding of the multi-scale fracture behavior of clinkers. In addition, the goal of this study is to develop experimental inference of the link between fracture properties of cement clinker and its chemo-physical properties. The following research question will therefore be addressed: *How are chemistry, mineralogy and microstructure of cement clinkers related to fracture properties at the different characteristic scales?*

This question is answered by pursuing the following objectives: (1) characterize the microstructure of industrial clinkers with respect to the characteristic scales and

particularities of the constituting crystals, (2) investigate average chemistry and mineralogy of industrial clinkers, as well as chemistry of the constituting phases, and (3) adapt the microscratch test method for investigation of fracture properties of heterogeneous industrial clinkers at their different characteristic scales.

1.3 Approach

To fulfill the research objectives, the methodology schematized in Fig. 1.2 is implemented. Four different types of industrial Portland cement clinkers are compared throughout the study. Before testing, specimens are carefully prepared for each type of experiment. Experiments on bulk powders are first performed to investigate the average chemistry (X-ray fluorescence) and mineralogy (X-ray diffraction) of the studied clinkers. Polished surfaces are then prepared to analyze the microstructure (scanning electron microscopy with backscattered electron imaging), with respect to porosity and phase particularities. These polished surfaces are also used for chemical analyses of the clinker phases (statistical electron probe microanalyses) and a method is developed to extract bulk chemistry and mineralogy from the same measurements. In addition, fracture properties are measured at different scales on polished surfaces (multi-scale microscratch test). Finally, the results from these complementary methods are compared and assembled to answer the research question.

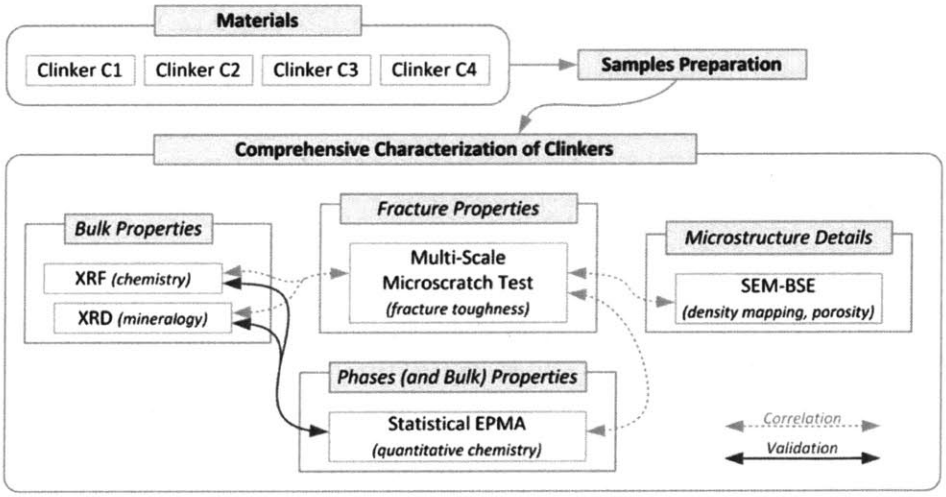

Fig. 1.2. Schematic representation of the methodology implemented in this project.

1.4 Outline

Following the general presentation (Part I), which includes the introduction (Chapter 1) and a review of the existing knowledge (Chapter 2), this document is separated into three parts focusing on materials and methods (Part II), results and discussion (Part III) and conclusions (Part IV).

In Part II, the materials are first presented (Chapter 3), followed by a description of the experimental methods commonly used for clinker characterization (Chapter 4), i.e., scanning electron microscopy, X-ray diffraction and X-ray fluorescence. Experimental details of an alternative clinker analysis method (statistical electron probe microanalyses) are then described in Chapter 5. The microscratching method is presented in Chapter 6, along with the work performed to minimize the experimental errors and to adapt the method for use at smaller scales.

Part III first presents the results regarding the characteristic scales and the microstructure of the studied clinkers (Chapter 7), and the qualitative and quantitative mineralogy (Chapter 8), along with the assessment of the non-quantified content (amorphous + residuals). In addition, bulk chemistry is measured and used to complement the mineralogy results, in order to distinguish the particularities of each studied clinker. An innovative clinker analysis method is also presented (Chapter 9). The method uses a single measurement (statistical EPMA) to extract simultaneously the chemistry of single phases, their abundance and the bulk chemistry. Chapter 10 focuses on the fracture toughness results measured on the four industrial clinkers at their characteristic scales, as previously defined. To complete Part III, Chapter 11 presents a discussion linking the measured characteristics to the clinker-grinding problem.

Finally, Chapter 12 concludes with a summary of the results and the contributions of this project, along with the industrial benefits and the perspectives for further developments.

Chapter 2

Existing Knowledge

Clinker grinding has been in the focus of the cement industry for several decades, which led to great improvements in grinding methods and efficiency. This chapter proposes a review of the literature published on the subject. The basics of clinker grinding are first presented to introduce the clinker phases, their mechanical properties, the successive stages in clinker grinding and the grinding technologies. Qualitative and quantitative correlations between clinker characteristics and their grindability are then described.

2.1 Basics of Clinker Grinding

Portland cement clinker is produced by burning a proportioned mix of ground limestone, clay, quartz and scrap metal. When the kiln temperatures reach 1450°C, these elements recombine and the four major clinker phases are formed: alite and belite, impure polymorphs of C_3S and C_2S (as abbreviated in cement chemistry and corresponding to chemical compositions $[CaO]_3.SiO_2$ and $[CaO]_2.SiO_2$, respectively); aluminate, C_3A; and ferrite, C_4AF ($[CaO]_3.Al_2O_3$ and $[CaO]_4.Al_2O_3.Fe_2O_3$, respectively). The hot clinker is then air quenched to preserve reactive polymorphs at room temperature, and nodules of up to several centimeters are formed. These nodules are co-grinded with gypsum into a cement powder with ~95% of particles passing the 45 μm sieve. Cement grinding depends mainly on the clinker properties, as gypsum requires less energy to grind.

2.1.1 Mechanical Properties of the Clinker Phases

In clinker nodules, relatively large crystals of silicates (i.e., alite and belite) form the matrix which is filled with an interstitial phase composed of aluminate and ferrite. Velez et al. [130] measured hardness, H, and elastic modulus, E, for each clinker phase by nanoindentation with a Berkovich probe. It was found that C_3A *is* the hardest phase,

(H = 10.8 GPa; E = 145 Gpa), compared to the other three phases (H = [8.8, 9.5] GPa; E = [125, 135] GPa). Slightly different results were obtained by de Souza et al. [112], who measured higher hardness for C_4AF than C_3A with a Vickers probe. These authors also measured lower elastic moduli in silicate phases ($E \approx 125$ GPa) compared to aluminate and ferrite phases ($E \approx 140$ GPa).

The influence of impurities embedded in silicates on mechanical properties has been studied, but there is no agreement on the results from different authors. Velez et al. [130] experiments showed no significant effect of impurities on mechanical properties of silicates. Atomistic simulations performed by Manzano et al. [77] agreed with these results regarding alite, however these authors suggested a 20% reduction of the elastic modulus when comparing pure C_2S to belite with 3% Mg^{2+}, Al^{3+} or Fe^{3+} ions. Phenomenological relationships based on average composition of clinkers have been proposed. De Souza et al. [113] mesured that the microhardness of silicates was proportional to the barium and iron contents, and inversely proportional to transition metals, aluminium and alkali contents. Opoczky and Gavel [92] observed an improved grindability for all trace elements they studied (Cr, Zn, Ba, Ti, P).

2.1.2 Fracture Properties of Clinker

In addition to hardness and elasticity, fracture toughness (or fracture energy) is an important characteristic to consider with respect to clinker grinding. Clinker is a brittle material to which the concepts of Linear-Elastic Fracture Mechanics (LEFM) may be applied. Initially proposed by Griffith [47], and further refined others authors such as Irwin [57], the framework of LEFM recognizes the pre-existence of flaws in materials and the failure is associated with the propagation of cracks from these defects. The energy release rate G is defined as the potential energy stored in the system, which is released when the crack propagates by $d\ell$. Griffith initially defined the following crack propagation criterion:

$$G \geq 2\gamma \leftrightarrow d\ell \geq 0; \quad G < 2\gamma \leftrightarrow d\ell = 0; \tag{2.1}$$

where 2γ is the surface energy of the two free surfaces created by the crack. To extend the theory to ductile materials, Irwin and coworkers introduced the concept of plastic zone developing at the crack tip. This led to the definition of a new crack propagation threshold,

the fracture energy $G_f = 2\gamma + G_p$, which accounts for the plastic dissipation G_p in addition to the energy of surface creation.

A complementary local approach focuses on the stress concentration at the crack tip, which is described by the stress intensity factor K. The crack propagates if K reaches a critical threshold, the fracture toughness K_C. In fact, both approaches share the same threshold, as the application of Irwin's formula establish a direct link between the fracture toughness and the fracture energy:

$$G_f = (\kappa/E)K_c^2 \tag{2.2}$$

where E is the Young's modulus, $\kappa = 1$ for plane stress and $\kappa = 1 - \nu^2$ for plane strain (ν is the Poisson's ratio).

Hornain and Regourd [53] measured the specific fracture energy γ on notched samples made of sintered clinker. Their results indicate that γ is an order of magnitude higher for the polycrystalline clinker (12 to 22 J/m²) compared to single crystals of C_3S (~1.0 J/m²) and C_3A (~1.4 J/m²). This higher resistance to fracture of a polycrystalline material, compared to its constituting crystals, is relatively common. It is associated with the presence of discontinuities, at the grain boundaries and in the pores [53].

In addition, Hornain and Regourd [53] determined the fracture toughness of the main clinker phases by measurements of radiating cracks from microindentations with a Vickers indenter probe. Their results show that the alite phase has the lowest fracture toughness of K_C = 1.7 MPa.m^{½}, in comparison to K_C = 3.1 MPa.m^{½} for the aluminate phase and K_C = 3.7 MPa.m^{½} for the belite phase (radiating cracks were not observed for ferrite in their experiments). These results are supported by the analysis of fractured clinkers surfaces. Cracks were observed to propagate mainly in the alite crystals and at the boundaries between phases. The cracks were usually stopped or deviated when reaching phases with higher toughness (belite crystals or interstitial phases). In addition, the authors explain the weakness of the alite crystals with the preferential cleavage planes and the anisotropic thermal dilation. Alite thermal dilation differs in magnitude from that of the crystallized liquid phase. Tensile stresses are thus created during quenching of clinkers, which results in microcracking. Following this work by Hornain and Regourd [53], the analysis of the

clinker-grinding problem based on fracture mechanics has not been further developed by other authors. This lack of scientific knowledge motivates much of this study.

2.1.3 Stages in Grinding

Tavares et al. [119] suggested a separation of grinding in three stages and correlated governing factors to each stage. Coarse grinding from nodules down to 1 mm particles is mainly governed by porosity and consists of breaking aggregates of crystals. Fine grinding down to cement particle size depends on properties of the individual phases and seems to be mainly influenced by aluminate and ferrite contents. An intermediate phase may also exist in between where alite content has the largest influence. Other authors have proposed different governing factors detailed in section 2.2.2.

2.1.4 Industrial Grinding

Industrial clinker grinding has evolved over the past decades in order to improve the energy efficiency, but equipment wear and final product quality have been limiting factors for the adoption of new technologies. Ball mills are still used for cement grinding, even if the energy use is far from optimal with this technology [111]. However, these mills are slowly being replaced by efficient technologies such as high pressure grinding rolls (HPGR), horizontal roller mill and vertical roller mill.

2.1.4.1 Collision Mills

The ball mill is the simplest type of collision mill and it has been widely used for clinker grinding because the maintenance is relatively easy. Steel balls (the grinding media) are placed in a rotating tube mill with a rippled profile to optimize lifting. The speed of the mill is adjusted so balls are lifted to a certain point before falling, as shown in Fig. 2.1a.

Two mechanisms are responsible for particle size reduction (Fig. 2.1b): the collision forces imposed to clinker particles fracture the grains, and the friction between particles creates attrition of softer particles. This combination of mechanisms is useful for cement grinding as the particle size distribution of the final product is wide, thus void ratio is low and water demand during the mixing of concrete is minimal. However, this kind of mill is not energy efficient because of the multiple impacts and the cushioning effects [20].

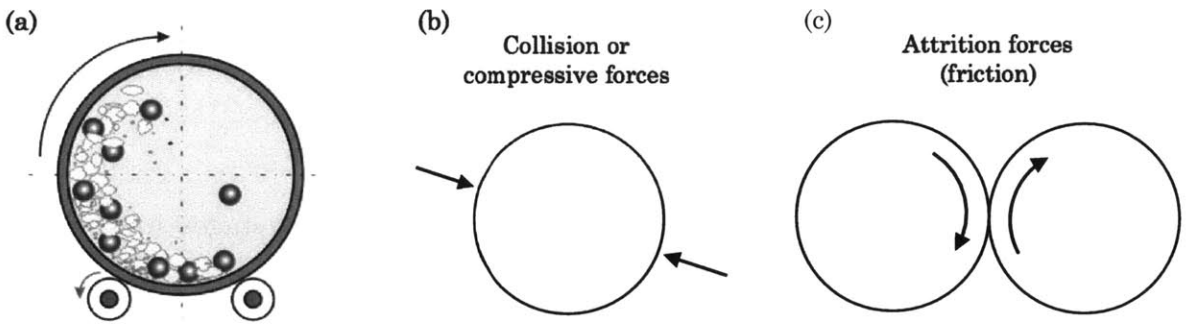

Fig. 2.1. (a) Schematic of the operation of a ball mill [55] and (b) representation of the forces acting on particles during grinding.

2.1.4.2 Compressive Mills

The concept behind compressive mills is the breakage of each crystal or aggregate of crystals separately by simple cleavage [20]. Different technologies, such as HPGR and roller mills, have been adapted to apply this concept to clinker grinding and they share these common characteristics.

First, the efficiency is greatly increased compared to ball milling because greater stress is directly applied with single-particle breakage. Unsuccessful impacts characteristic of ball mills are minimized, and the energy lost as heat is thus reduced [117]. The wear of the equipment and the complexity of maintenance were issues that needed to be addressed before large-scale adoption of these technologies, as clinker particles are very hard and abrasive. Another concern regarding the compressive mills is that cements may have different properties, when compared to those produced with ball mills. These cements usually have a narrower particle size distribution, as shown in Fig. 2.2. This leads to higher strength for the same fineness because the average particle size is lower. At the same time, the water demand is higher, which is not desirable [107]. In addition, particles of gypsum are coarser and less dehydrated because of lower grinding temperatures with these types of mills. Initial setting time can be significantly reduced if this behavior is not considered in gypsum proportioning [20].

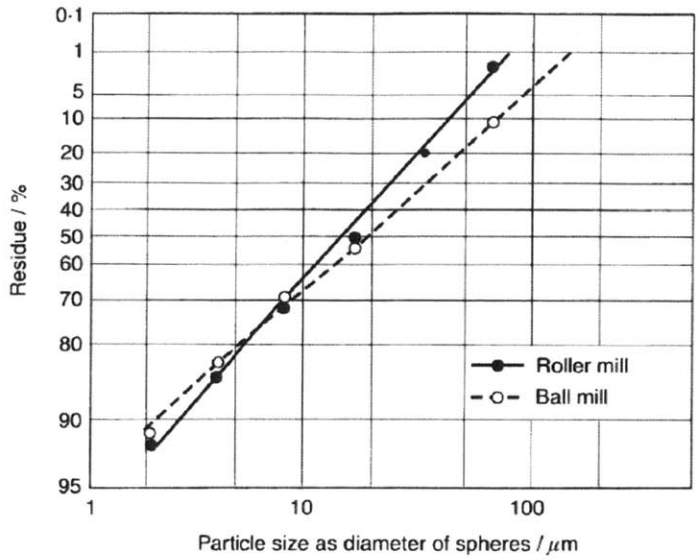

Fig. 2.2. Effect of mill type on the particle size distribution of cement with a Blaine surface area of 280 m^2/kg, plotted on a Rosin-Rammler-Sperling-Bennett grid [20].

High pressure grinding rolls

High pressure grinding rolls (HPGR) consist of two counter-rotating rollers delivering high pressure (more than 50 MPa) on particles, see Fig. 2.3a. A rotating motion brings material between rollers where compressive forces cause size reduction and extensive micro fracturing of the grains. Compacted "cakes" exit the HPGR and they can either be disagglomerated or further grinded. To prevent narrow particle size distributions, HPGRs are often used in the cement industry for pre-grinding and intermediate grinding. Fine grinding is then performed with conventional ball mills. However, the technology can also be used as a single-stage process up to fine grinding [111].

Microscopic observations performed by Celik [23] on fractured surfaces showed that higher loads applied by HPGRs result in a rougher surface texture, preferential fracturing along grain boundaries and fissures on the surface of particles. This leads to greater specific surface areas in comparison to similarly sized ball mill particles, which are formed by repeated collisions and transgranular fracture.

Horizontal roller mills

Horizontal roller mills are a hybrid solution between tube mill and HPGR fracturing. As shown in Fig. 2.3b, particles are pressed between a cylindrical roller and the surface of a

tube mill. Particles stay in the mill for multiple cycles of pressing until sufficient fineness is achieved. This kind of mill can be used for a single-stage grinding process, with energy savings up to 50% compared to ball milling [111].

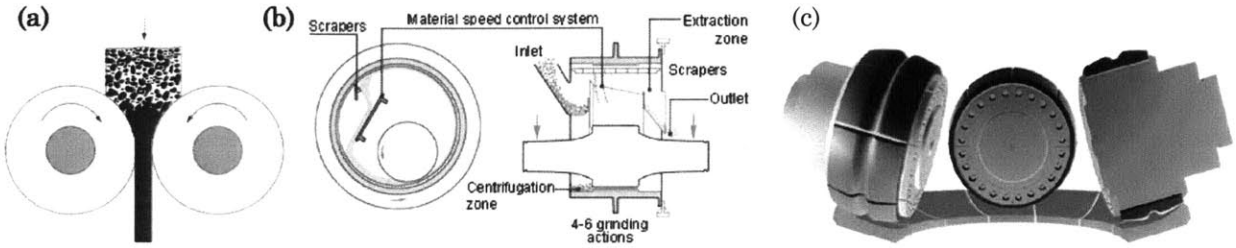

Fig. 2.3. Schematized grinding mechanisms of (a) HPGR [20], (b) horizontal roller mill [35] and (c) vertical roller mill [109].

Vertical roller mills

Vertical roller mills also take advantage of a concentration of compressive forces over a thin layer of material. Particles are ground on a rotating table by rollers applying compressive forces (see Fig. 2.3c). Centrifugal forces bring material under the rollers and then out of the table, where airstreams bring the particles to a classifier above grinding table. Particles of adequate sizes are collected as final product and coarser particles are returned on the table for further grinding. This kind of mill can be used for a single-stage grinding, with energy savings up to 40% compared to ball milling [111].

2.2 Empirical Correlations Based on Clinker Characteristics

Several experimental studies performed over the last decades focused on the impact of clinker characteristics on its grindability. Extensive literature reviews were published in 1995 and 2007 by the Portland Cement Association [52,51]. The general trends described in the following paragraphs are derived from these studies. The term "grindability" is defined such as clinkers with higher grindability requires less grinding energy.

2.2.1 Laboratory Techniques for Grindability Measurement

The most common way of measuring grindability is the use of small laboratory mills. The grinding energy can then be related to the fineness measured by air permeability with the Blaine apparatus [12]. Zeisel's method [139], a variation of Hardgroove test used in the

cement industry, defines specific grindability as the consumed grinding energy per unit mass of sample required to obtain a specific Blaine fineness (usually around 300 m^2/kg). The Bond's ball mill grindability test [15] is another widely used method that simulates closed circuit dry milling. Cycles of grinding and sieving are performed with a miniature ball mill, until equilibrium state is reached. Bond's work index can be calculated from sieve opening and percentage passing at equilibrium. A higher work index corresponds to a lower grindability.

Miniature laboratory mills and the methods described above are very useful to measure fine grindability. The drop weight test is more adequate to determine coarse grindability [42,112]. In this test, the resistance to impact breakage is determined from data obtained in single particle breakage tests for a range of particle sizes. Other laboratory measurements such as optical microscopy, mineralogical and chemical analyses can be used to estimate clinker grindability with the help of empirical correlations, as detailed in section 2.2.3.

2.2.2 Effects of Clinker Characteristics on Grindability

Influence of Silicate Phases

Published experimental results generally agree on the importance of the proportions of silicate phases, higher alite and lower belite contents result in a clinker that is easier to grind. This behavior can be explained by crystal toughness. Alite crystals contain micro-cracks and are prone to crack propagation, whereas belite crystals are rounder and more ductile [132,118].

In addition, it was found that small silicate crystals result in improved grindability. As suggested by Viggh [132], larger crystals not only require more energy to fracture, but the resulting fractured particles are charged and may have a higher tendency to agglomerate than similarly sized small alite crystals. Another possible explanation is that large silicate crystals may encourage dust formation, which has a negative impact on grinding [80].

Agglomeration and adhesion to grinding media is also a source of decreased grindability. The tendency to agglomerate is lower for alite than belite (the β belite polymorph has the highest tendency).

Another important parameter is the distribution of belite. Clusters, or nests, can be formed because of larger quartz particles in raw mix. These clusters are harder to grind than individual belite grains, and they increase the energy required for fine grinding [74].

Influence of Interstitial Phase

The interstitial phase is composed of C_3A and C_4AF, which are the hardest compounds of clinker and may thus be responsible for reduced fine grindability [119]. However, other authors suggest that an increased interstitial phase content is favorable to grinding [132]. Overall, there is no agreement in the literature regarding the effect of the interstitial phase [52].

Nevertheless, it was found that crystallized interstitial phases were easier to grind than vitreous liquid phases resulting from excessively rapid cooling of clinker [46]. In addition, large volume shrinkage occurs from the crystallization of the interstitial phase, which exerts tensile stresses on alite crystals and enhances its microcracking [74]. This indirectly improves grindability, by weakening of the alite crystals.

Influence of Other Parameters

General agreement exists regarding the possible improvement of coarse grinding with increased porosity. Smaller and well distributed pores seem to be preferable to large pores [93,40], but the reasons behind this observed trend are not explained. The influence of MgO content is also not clearly understood. Some authors suggest that periclase has a negative effect on grindability because of its hardness is higher than that of alite and belite [13]. However, other authors have measured an improvement in fine grindability with the increase in periclase content [112]. In contrast, good agreement exists on the positive effect of free lime particles. They do not bond firmly to the surrounding materials and this creates weakness in clinker mass [97]. Dusty clinkers and clinkers with large nodules were also found to be harder to grind [95,80].

2.2.3 Empirical Correlations for Estimation of Grinding Energy

Over the years, authors have proposed different correlations, fitted from a large number of data, to link clinker characteristics to grindability. Ono [90] established an empirical relation between grindability and analyses of silicates under an optical microscope.

Grindability is measured with Blaine fineness, *Bl*, obtained after 45 minutes of grinding in a prescribed laboratory mill. A correlation is drawn with alite size *AS*, alite birefringence *AB*, belite size *BS* and belite color *BC*:

$$Bl = 1251 + 218AS + 239AB + 287BS + 2.1BC \tag{2.3}$$

This relation was also used by Kawamura [63], who obtained good fits of his data with some adjustment of the empirical coefficients.

Other authors [105,132] prefer a correlation between the Zeisel grindability, *P'*, at 3200 cm^2/g and the belite corrected specific alite content, *Ak* (a function of silicates contents and sizes):

$$\begin{aligned} P'(KWh/t) &= -20.7 * lnAk + 57.9 \\ Ak &= C_3S\%/C_3Ssize - C_2S\% * C_2Ssize/1000 \end{aligned} \tag{2.4}$$

Venkateswaran and Gore [131] proposed the same relations for belite-rich clinkers with Bond's mill test. For such types of clinkers, a revision for *Ak* was formulated:

$$Ak = \frac{C_3S\%/C_3Ssize}{C_2S\% * C_2Ssize/1000} \tag{2.5}$$

Theisen [123] developed relations by adopting a different methodological approach. Alite intersections, N_{C3S}, and porosity, *p*, were measured by microscopic point count over random lines. Empirical relations were then fitted with silicate contents and power consumption, P_{350}, required to reach a fineness of 350 m^2/kg. One of the relations they fitted reads as:

$$\begin{aligned} P_{350} &= 30.2 + 0.34 * C_3S_N + 0.38 * C_2S\% - 11.5 * TEA \\ C_3S_N &= C_3S\% * 20 * (1 - p)/N_{C3S} \end{aligned} \tag{2.6}$$

where TEA is a grinding aid. In a recent study, Genc and Benzer [42] proposed relations between single particle impact breakage parameters and silicate contents. Specific comminution energy, E_{cs} (kWh/t), of the drop weight test was related to t_{10} (amount of material passing $1/10^{th}$ of the original size) in order to calculate breakage parameters *A* and *b*. The resistance to impact breakage was reported as *A*b* (higher values indicate lower resistances), and correlated with silicates contents:

$$t_{10} = A * (1 - e^{-b*E_{cs}})$$
$$A * b = 333 - 5.8 * (C_2S\%) - 3.4 * (C_3S\%) \quad (2.7)$$

Similar tests were performed by Tavares et al. [119] who established a relationship of proportionality between breakage parameters $A*b$ and the percentage of porosity. The Bond's workability index, Wi, was measured for different sieve sizes (75, 150 and 300μm). They obtained the following correlations which suggest different governing factors for different grinding stages:

$$Wi(300\mu m) = 76.4 - 0.50 * Porosity - 0.74 * C_3S\%$$
$$Wi(150\mu m) = 55.6 - 0.46 * C_3S\% - 1.39 * C_3A\% - 0.54 * C_4AF\% \quad (2.8)$$
$$Wi(75\mu m) = 42.8 - 2.79 * C_3A\% - 1.36 * C_4AF\%$$

All these empirical correlations can be useful to estimate the grindability of clinker, but may not be applicable to clinkers produced in different contexts without adjustment of the empirical coefficients. However, these relations add quantitative evidence to the role of alite and belite contents and sizes as important clinker characteristics with respect to grindability.

2.3 Chapter Summary

This chapter presented a review of existing technology and literature on Portland cement clinker. The problem was discussed from different perspectives including characterization of clinker phases, grinding technologies, and fracture mechanisms.

Authors generally agree that coarse fracture of clinker nodules originates mainly in microcracks and weak cleavage planes of brittle alite crystals. Cracks would then propagate in porosity and at grains boundaries, contour the rounded belite crystals and sometimes terminate in the harder interstitial phase. On the other hand, fine grinding is controlled by characteristics of individual phases, as they have already been separated. Experimental observations and empirical correlations showed strong evidence that grindability was improved with an increase in alite content and a decrease in belite content. Other characteristics such as large crystal sizes, agglomeration tendency or an amorphous state of the interstitial phase were also found to reduce grindability.

Clinker grinding is usually performed at the industrial scale either by impact breakage (and attrition) in ball mills, or more efficiently, by pressure fracturing in different types of compressive mills. To date, clinker-grinding optimization was mostly based on phenomenological studies. To advance this research, a deeper knowledge of clinkers from a fracture mechanics perspective is required. This motivates the following investigation, which aims at providing a better understanding of clinker fracture, by using multi-scale experimental methods applied to industrial clinkers.

Part II

Materials and Methods

Chapter 3

Materials

The aim of this study is to characterize normal cement clinkers from new perspectives. Investigations are performed on clinkers samples provided by our industrial partners. Thanks to this partnership, we are able to work with clinkers sampled directly from the production line of different cement plants. Two different types of sample preparation are performed to produce powdered samples and polished surfaces, respectively.

3.1 Studied Clinkers

Four industrial cement clinkers are investigated in this work. These were obtained from four distinct cement plants and labeled as *C1*, *C2*, *C3* and *C4*. The samples were received in the form of nodules with diameters generally below 50 mm. In order to ensure integrity, the samples were stored in doubled plastic bags and placed in an environment with controlled temperature and humidity.

No information was provided regarding material properties and manufacturing conditions. However, significant difference in nodules shape, size, color and resistance to handling, suggested that the four clinkers were produced in significantly different manufacturing conditions. Further description is presented in the microstructure investigations (Chapter 7.

3.2 Sample Preparation

3.2.1 Powdered Samples

Powdered samples were prepared for X-ray diffraction (XRD) analyses by manual grinding of the studied clinkers. A representative sample of 30 grams was randomly selected for each clinker after homogenization. The samples were coarsely ground in an agate mortar for 10 minutes per 5 grams, then dried for 12 hours at 110°C, and finally cooled in desiccator for

30 minutes. After homogenization, 4 subsamples of 2 grams were finely ground for each clinker in the agate mortar for 3 minutes per 0.4 grams. The coarsely ground and finely ground powders were dried, and then stored in hermetic bottles placed in a desiccator.

3.2.2 Epoxy-Embedded Polished Surfaces

One of the requirements for scanning electron microscopy (SEM) and electron probe microanalyses (EPMA) is a flat polish (< 1 μm) of the specimen surface [45]. To fulfill this condition and minimize the influence of surface geometry on the measurements, clinkers samples were impregnated in epoxy and polished with a semi-automatic procedure optimized for hard and porous clinker samples. This preparation procedure was also applied to the samples used for microscratching.

The bulk samples (*B* series) were prepared with clinker nodules of 20-30 mm in diameter. A low speed diamond saw (IsoMet, Buehler, USA) was used to cut slices of 12 mm thickness, which was found to be adequate for complete epoxy impregnation of the pores. Each slice was placed in a cylindrical mold inside a vacuum impregnation device, as shown in Fig. 3.1. A vacuum of 26" Hg was created in the chamber and the mold was filled with epoxy (EpoThin, Buehler, USA). To allow complete impregnation of the pores, 5 pressure cycles were performed, each cycle consisting in 1 minute under vacuum followed by 1 min at atmospheric pressure, as suggested in [18].

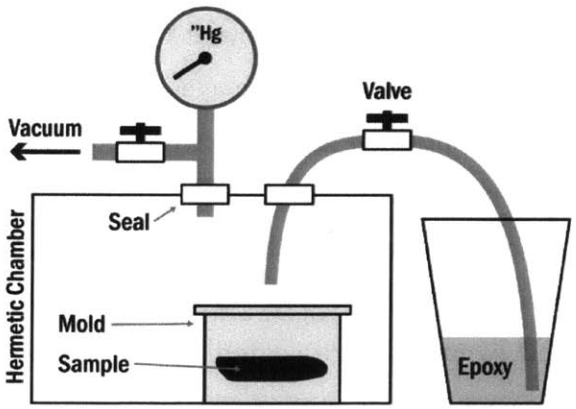

Fig. 3.1. Epoxy impregnation setup. The sample is placed in a mold inside a hermetic chamber, a vacuum of 26" Hg is created and the epoxy is poured into the mold by suction. Pressure cycles are then performed to remove the air from porosity.

After hardening, slices of ~12 mm in diameter by 4 mm in height were cut with the slow speed saw, and then mounted with cyanoacrylate glue on standard AFM bases of 15 mm diameter (Ted Pella, USA). Mounted samples were automatically leveled and ground with a specially designed jig and post system, as described elsewhere [81] and schematized in Fig. 3.2. This system was used on a turntable with a hard perforated cloth (TexMetP, Buehler, USA) and a 9 μm oil-based diamond suspension (MetaDi, Buehler, USA). Leveling of samples was usually achieved within 20 min.

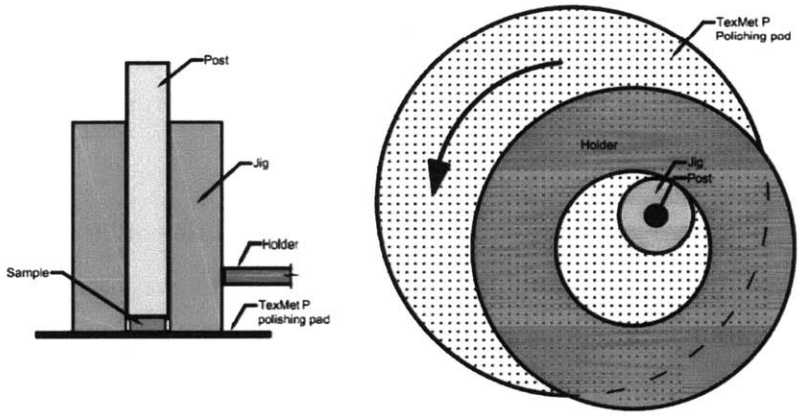

Fig. 3.2. Schematic of the leveling setup by Abuhaikal and Ulm [1]: (a) cross section of the jig and post system, (b) top view of the system used with a turntable and a circular holder allowing oscillation of the jig.

Leveled samples were polished in 2 steps with dry abrasive discs (FibrMet, Buehler, USA): 1 min polishing on a 3 μm diamond pad was followed by 1 min on a 1 μm alumina oxide pad. After each polishing step, 3 min of ultrasonic cleaning in n-Decane (TCI, Japan) was performed. The final surfaces obtained are characterized by rare occurrence of surface irregularities visible under 20x and 50x objectives of the optical microscope, and by a high mirror-like reflectivity of the surface, as illustrated in Fig. 3.3. After final ultrasonic cleaning, samples were dried in an oven at 40°C for 12 hours, and then stored in a desiccator. Finally, polished samples were coated with a 25 nm carbon layer prior to the electron microscopy investigations.

Fig. 3.3. Typical polished clinker sample. After epoxy impregnation and cutting, samples are glued on AFM disks, automatically leveled and manually polished to a mirror-like surface.

In addition to bulk samples (*B*- Series), two series of epoxy impregnated samples were prepared with the powdered samples initially prepared for XRD analyses: a first series with the coarsely ground clinkers (*C*- Series) and a second series with the finely ground clinkers (*F*- Series). For each sample, 2 grams were compacted with a post in a cylindrical mold of 12 mm in diameter. Epoxy impregnation and sample polishing were performed similarly as for bulk samples, with the difference that the dry abrasive disks used were alumina oxide pads of sizes 9 μm, 3 μm and 1 μm (FibrMet, Buehler, USA). Diamond polishing pads were found to be too aggressive, leading to removal of surface grains and generating irregularities on the surface.

3.3 Chapter Summary

Four industrial cement clinkers provided by industrial partners were first presented. Powdered samples were then prepared in an agate mortar for use in X-ray diffraction. In addition, polished surfaces of clinkers (bulk and powders) embedded in epoxy were prepared by automatic leveling and manual fine polishing. The polishing procedure was optimized for preparation of samples for use with SEM, EPMA and the microscratch test.

Chapter 4

Clinker Characterization

As previously discussed in Chapter 2, cement grinding is closely related to clinker properties such as microstructure, mineral composition and chemical composition. A complete characterization of the studied clinkers is thus of prime importance for this study. Based on techniques used in the cement industry, this chapter presents the methodology used to investigate (1) the microstructure with scanning electron microscopy, (2) the mineralogical composition with X-ray diffraction and the Rietveld method, and (3) the chemical and mineralogical compositions with X-ray fluorescence and the Bogue calculation.

4.1 Scanning Electron Microscopy

Optical microscopy and scanning electron microscopy (SEM) is extensively used for clinker characterization, as observation of microstructure is of great importance to improve the general understanding of clinkers. Thanks to Dr. Campbell who regrouped findings from hundreds of publications [22], microstructure observations can be linked to particular grinding behaviors, cement reactivity, and kiln operation conditions. In this study, SEM analyses are used to characterize the particularities of clinker phases (e.g., size, repartition, microcracking), as well as the porosity and the apparent size distributions of the powdered samples embedded in epoxy.

4.1.1 Experimental Protocol

Epoxy-embedded polished surfaces were analyzed with a JEOL 5910 scanning electron microscope (SEM). Backscattered electron (BSE) imaging mode was chosen to provide contrast between the crystal phases, and for easy identification of pores and grain boundaries. Analyses were performed with different magnifications (100X, 250X, 500X, 1000X and 2000X) and an accelerating voltage of 15 kV.

4.1.2 Identification of Clinker Phases Particularities

As illustrated in Fig. 4.1, SEM-BSE imaging of a clinker surface results in a grayscale image with clear distinction between the main clinker phases. The measured gray level depends on the backscatter coefficient, η, which is a direct function of the mean atomic number, $\bar{Z}$, of the probed phase [45]. As presented in Table 4.1, backscatter coefficients for the major clinker phases are sufficiently different to allow phase identification with an adequate adjustment of brightness and contrast of the instrument. The backscattered coefficients of belite and aluminate are too similar for distinction. This limit is overcome with the use of the characteristic shapes associated with these phases. The belite crystals are usually rounded whereas aluminate crystals are generally of smaller dimension and intermixed with ferrite crystals.

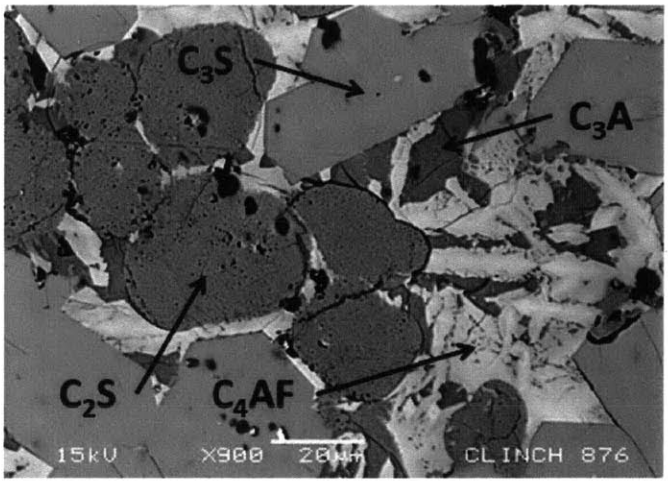

Fig. 4.1. BSE image of a clinker sample by Abuhaikal and Ulm [1] with clear distinction between the phases: alite (~C_3S), belite (~C_2S), aluminate (C_3A) and ferrite (C_4AF).

Phase	ρ (g/cm^3)	$\bar{Z}$	η
Alite (C_3S)	3.15	15.057	0.174
Belite (C_2S)	3.28	14.562	0.166
Aluminate (C_3A)	3.03	14.339	0.164
Ferrite (C_4AF)	3.80	16.651	0.186
Free Lime (CaO)	3.32	-	-

Table 4.1. Physical properties of the main clinker phases: usual values for density ρ [22,20], mean atomic number $\bar{Z}$ and backscatter coefficient η calculated with Monte Carlo simulations by Wong and Buenfeld [136].

After identification, the characteristic crystal size of each phase can be determined by direct measurement. In addition, the presence of microcracks (created by differential thermal volumetric changes upon quenching of clinker) is identified by visual observation of the crystals and their boundaries.

4.1.3 Image Analysis and Apparent Size Distributions

Quantitative analyses of the surface were carried out to investigate porosity domains and particle size distributions of the powdered samples. In both cases, parameters of the SEM were adjusted to maximize contrast between the gray bulk surfaces and the black porosity filled with epoxy. Typical images used in the analyses are presented in Fig. 4.2.

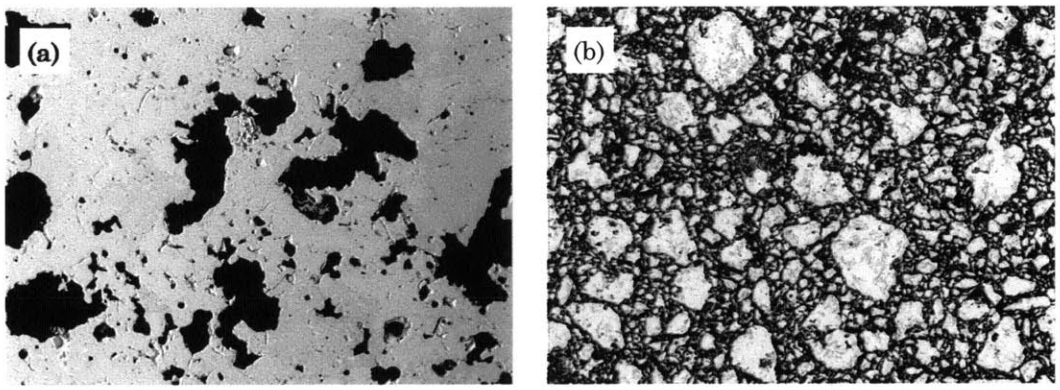

Fig. 4.2. BSE imaging of polished surfaces with brightness and contrast adjusted for optimal separation between porosity and matrix/particles. (a) Bulk sample of clinker C1 and (b) coarsely powdered sample of clinker C1. Magnification is set to 100X and each image represents an area of ~1.3 mm by ~1 mm.

With the aim to characterize the surfaces (and not the 3D microstructure), apparent size distributions were extracted from 2D cross-sections without any application of stereology to estimate the 3D pore/particles size distributions. Nevertheless, total porosity/particle volume was approximated based on the Delesse principle [84] which stipulates, that the volume fraction, f_{Vi}, of a phase i is equal to its area fraction, f_{Ai}:

$$f_{Vi} = \frac{V_i}{V_{total}} \equiv \frac{A_i}{A_{total}} = f_{Ai} \tag{4.1}$$

ImageJ, a non-commercial image analysis package [19], was used for processing of the micrographs (smoothing, flat-field subtraction, manual binary thresholding) and for

determination of the particles boundaries and surface areas, A. Equivalent particle diameters were calculated assuming circular particles, $d_{eq} = 2 * (A/\pi)^{1/2}$, and apparent pore/particle size distributions were compiled. To avoid sampling effects, the analyses were performed on several randomly selected images to investigate surfaces much larger (by at least one order of magnitude) than the largest heterogeneities.

4.2 X-Ray Diffraction and Rietveld Analyses

Mineralogical composition of the studied clinkers was assessed with X-ray diffraction (XRD) measurements performed on finely powdered samples. Qualitative analyses allowed the identification of the crystalline phases, and the Rietveld method provided a quantitative estimation of their relative abundance. In addition, the internal and external standards methods were used to determine the amorphous content for each sample. The methodology presented in the following paragraphs was developed in collaboration with Nicolas Venkovic, using insightful advices from Dr. Scott Speakman, research specialist at the X-ray Diffraction Facility of the Center for Materials Science and Engineering, at MIT.

4.2.1 Experimental Protocol

XRD analyses were performed with a *PANalytical X'Pert Pro Multipurpose Diffractometer* equipped with a copper source, an open Eularian cradle and high-speed Bragg-Brentano optics, as illustrated in Fig. 4.3. The incident beam was focused with a 0.04 radian soller slit, a 0.5° fixed divergence slit, a 1° anti-scatter slit, and a 15 mm limiting beam mask. The diffracted beam was focused with a 0.02 radian soller slit and a 0.5° anti-scatter slit. The detector was a *X'Celerator* with an acquisition time set to 50 seconds per step of 2.122°2θ, for angles ranging from 10°2θ to 70°2θ. The total duration of each scan was around 25 minutes. This was determined to be adequate to obtain sufficient intensities over background for the smallest peaks [114,94].

Before each XRD scan, the subsample to be tested was homogenized, and then a 27 mm circular sample holder was backfilled and compacted in three layers with the set of tools shown in Fig. 4.4. Such a procedure was found to be optimal to meet the XRD surface requirement which is a homogeneous, densely packed and smooth flat surface with randomly oriented grains [94].

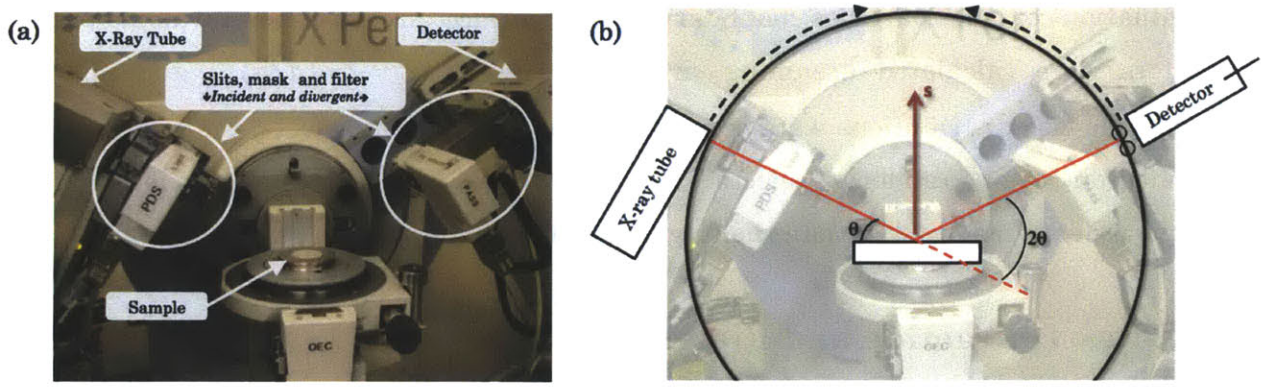

Fig. 4.3. (a) PANalytical X'Pert Pro Multipurpose Diffractometer showing the sample, the X-ray tube, the detector, the slits, the mask and the filter. (b) Bragg-Brentano geometry: the X-ray tube and the detector move symmetrically to ensure equality between incident and divergent θ angles.

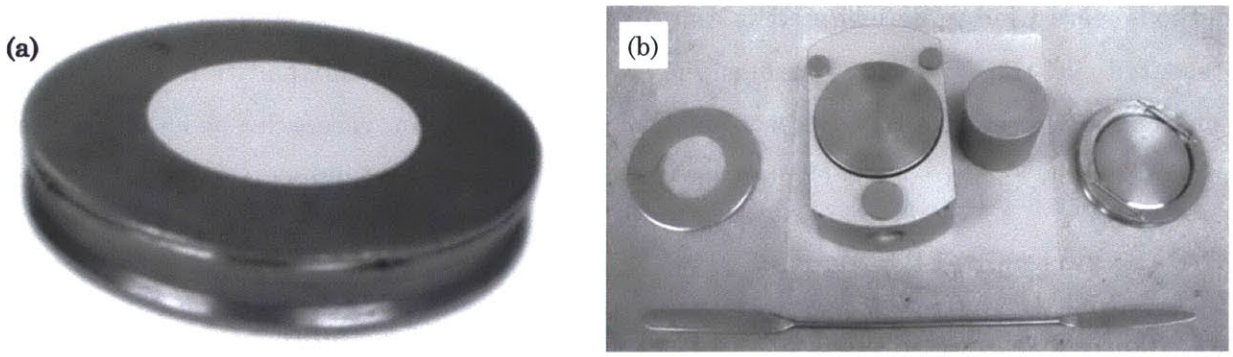

Fig. 4.4. (a) Perfectly leveled surface of a powdered sample backfilled in a 27 mm circular sample holder. (b) Set of tools used for backfilling of the sample holder.

4.2.2 Qualitative Analyses

The qualitative phase identification was performed with the help of the software High Score Plus. Best matches were identified between the experimental spectra and the patterns from the *Powder Diffraction File* (PDF) database published by the *International Centre for Diffraction Data* (ICDD). All experimental peaks were identified and validated against results presented by Taylor [121]. Fig. 4.5 shows the phase identification for a XRD scan of the NIST reference clinker SRM 2688. The peaks for the four major clinker phases are labeled in the figure, i.e., alite, *A*, belite, *B*, aluminate, *C*, and ferrite, *F*. In addition, typical angles for periclase, *P*, and free lime, *L*, are identified, even if the intensity for these phases is negligible in this reference clinker.

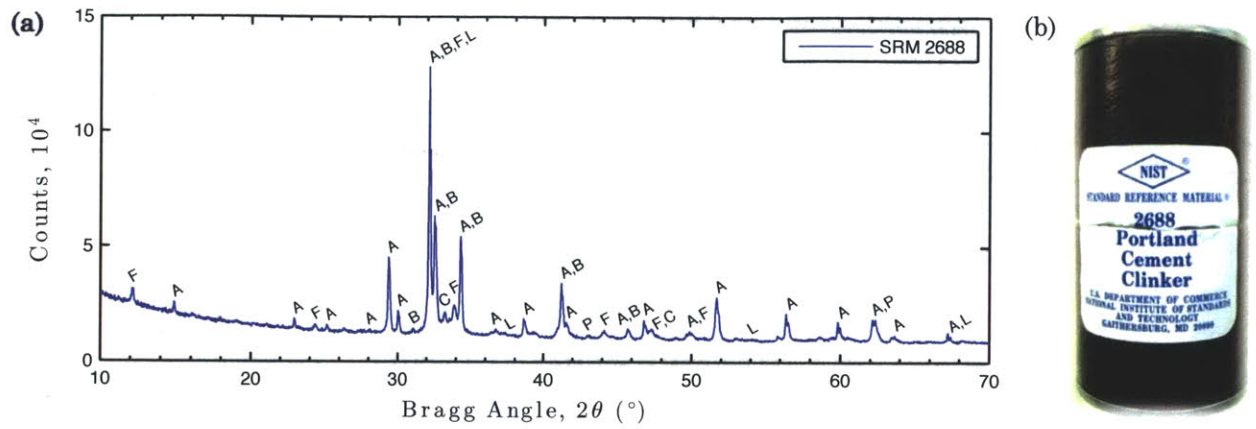

Fig. 4.5. (a) Qualitative phase identification for the X-ray diffraction scan of the NIST reference clinker SRM 2688. Major phases identified are alite, *A*, belite, *B*, aluminate, *C*, ferrite, *F*, with possible trace amounts of periclase, *P*, and free lime, *L*. (b) Container of the reference clinker SRM 2688 provided by NIST.

4.2.3 Quantitative Rietveld Analyses

The full profile refinement was performed with the Rietveld method to quantify the relative amounts of the main clinker phases. The clinker components identified in qualitative analyses were used for the Rietveld fitting. As different crystal structures were available in literature for each clinker phase, two different sets were investigated in order to determine the most appropriate structures. A first set, *S1*, was inspired from structure choices by Le Saoût [103] and a second set, *S2*, from a combination of other publications [59,116]. Both sets of crystal structures are presented in Table 4.2.

The refinement procedure was iteratively developed and a 5 steps process was defined. Special care was given as not to favor any crystal structure and to limit the refined parameters [94,43,103]. The first step consists of refining the global shift with the specimen displacement parameter, the background with a Chebyshev II polynomial (refining flat background + 9 coefficients) and the scale factor for each crystal structure. Then, lattice parameters for all structures are added to a second step of refinement. In the third step, lattice parameters are turned off and preferred orientation is refined for alite structures, to account for distortions in alite peaks relative intensities. Steps 4 and 5 consists of refining peak shapes for phases occurring in amounts higher than 10% (peak shape should not be refined for minor phases because fitting may results in erroneous modeling of background

with these phases [114,138]). The peak width W parameter and one peak shape parameter are successively turned on and off during the two last steps.

Phase	Formula	Crystal system	Set	PDF Code	Reference
Alite	Ca_3SiO_5	Monoclinic/M_3	S1	01-070-8632	De la Torre *et al.* [69]
			S2	04-009-5560	Nishi *et al.* [88]
		Monoclinic/<M_1>	S1, S2	–	Noirfontaine *et al.* [89]
Belite	C_2SiO_4	Monoclinic/β	S1	01-083-0460	Tsurumi *et al.* [126]
			S2	04-008-8073	Jost *et al.* [61]
		Orthorhombic/α′	S1, S2	04-012-6734	Mumme *et al.* [85]
Aluminate	$Ca_3Al_2O_6$	Cubic	S1, S2	04-008-8069	Mondal & Jeffrey [83]
	$Ca_{8.5}NaAl_6O_{18}$	Orthorhombic	S1, S2	04-012-8663	Nishi & Takeuchi [87]
Ferrite	Ca_2AlFeO_5	Orthorhombic	S1	04-006-8923	Colville & Geller [25]
			S2	04-011-5939	Jupe *et al.* [62]
Free Lime	CaO	Cubic	S1, S2	01-082-1691	Huang *et al.* [54]
Periclase	MgO	Cubic	S1, S2	04-004-8990	Taylor [120]

Table 4.2. Sets of crystal structures investigated for optimal Rietveld refinements of clinkers. The set S1 is inspired by Le Saoût [103] and the set S2 is a combination of crystal structures used in other publications [59,116].

The quality of each refinement is determined both by visual and quantitative assessment of the residuals. Careful visual inspection of the calculated profile, along with the experimental profile and their difference (the residual profile), is essential to validate adequate modeling of all experimental peaks. The weighted residual profile, R_{wp}, is used for quantitative evaluation of the fit. This figure of merit is calculated with Eq. (4.2), in which y_{Ei} is the experimental intensity of the i^{th} data point on 2θ, y_{Ci} is the calculated intensity and w_i the weight for this same point (usually $w_i = 1/y_{Ei}$) [94]. Although there is no universal critical value for R_{wp}, a reasonable criterion is $R_{wp} < 10\%$, considering the experimental parameters used in this study [114].

$$R_{wp} = \sqrt{\frac{\sum w_i(y_{Ei} - y_{Ci})^2}{\sum w_i(y_{Ei})^2}} \tag{4.2}$$

The choice of crystal structures and the refinement procedure were validated according to ASTM standard C1365-06 [11], with the NIST reference clinker SRM 2688. Three XRD spectra of the reference were recorded and analyzed with the procedure defined above to measure repeatability. Accuracy was determined with comparison to known values provided with the reference clinker.

As presented in Table 4.3, the repeatability criterion was met with both sets of crystals, since the variation between two tests executed by the same operator, *d2s*, was below the limiting value $d2s_{lim}$ for all phases. Accuracy was insufficient when the set S1 was used. The difference $\Delta\bar{x_1}$ between the measured mean value $\bar{x_1}$ and the know certified value $\bar{x_0}$ was superior to the limit $\Delta\bar{x}_{lim}$ imposed in the ASTM standard for tests performed on three replicates. On the other hand, the good accuracy obtained with the set S2 validated the use of the proposed refinement procedure with these crystal structures.

Phase	NIST	ASTM C1365-06		Set S1			Set S2		
	$\bar{x_0}$	$d2s_{lim}$	$\Delta\bar{x}_{lim}$	$\bar{x_1}$	$d2s_1$	$\Delta\bar{x_1}$	$\bar{x_2}$	$d2s_2$	$\Delta\bar{x_2}$
Alite (wt%)	65.0	*2.0*	4.9	69.5	*1.1*	4.6	65.6	*0.6*	0.6
Belite (wt%)	17.5	*1.8*	2.7	13.4	*0.7*	4	19.3	*1.7*	1.9
Aluminate (wt%)	5.0	*1.3*	1.6	2.5	*0.9*	2.5	3.7	*0.6*	1.3
Ferrite (wt%)	12.2	*1.4*	1.8	14.2	*1.1*	2	11.4	*0.6*	0.8
Lime (wt%)	0.0	-	-	0.3	*0*	0.3	0	*0*	0
Periclase (wt%)	0.0	*0.6*	0.6	0	*0*	0	0	*0*	0
R_{wp} (%)				(7.2 < 10)			(5.8 < 10)		

Table 4.3. Validation of the refinement procedure and selection of the optimal set of crystal structures. NIST certified composition of reference clinker SRM 2688 [86] is presented along with the ASTM C1365-06 [11] criteria for repeatability, $d2s_{lim}$, and accuracy, $\Delta\bar{x}_{lim}$. Rietveld refinement results obtained for three replicates with the two set of crystal structures are presented and confronted to the ASTM criteria.

Quantitative Rietveld refinements results are expressed in weight fractions, $\hat{\pi}^j_{wt}$, for each j=1...n crystalline phase. To allow further comparison with other methods, results are also be converted into volumetric fractions, $\hat{\pi}^j_{vol}$, with the use of Eq. (4.3) and the typical density of the clinker phases, ρ_j, presented in Table 4.1.

$$\hat{\pi}^j_{vol} = \frac{\hat{\pi}^j_{wt}/\rho_j}{\sum_{j=1}^{n}(\hat{\pi}^j_{wt}/\rho_j)} \tag{4.3}$$

4.2.4 Assessment of Non-Quantified Content

Quantitative Rietveld analyses are normalized to the crystalline phases identified and considered in the refinement. The results do not account for contributions of non-quantified content such as amorphous material, non-detected crystalline phases and residuals from fitting. To determine this non-quantified content and the absolute quantitative phase

composition, the internal standard and the external standard methods were investigated using the SRM 674 α-alumina corundum standard from NIST.

Internal Standard Method

As previously used for clinkers by different authors [82,133,116], the internal standard method consists of mixing prescribed proportions of the tested sample with a standard of known crystalline content. Rietveld refinement of the mixture is performed and calibrated with the known quantity of crystalline standard. The absolute content of each crystalline phase is then determined, and the non-quantified content is finally calculated as the difference between 100% and the sum of the crystalline phases.

Preliminary trials with this method resulted in unexpectedly high levels of non-quantified contents, which were explained by microabsorption effects. Probing a mixture of phases having strong differences in their linear attenuation coefficients, μ, can lead to an underestimation of the phases with high μ coefficients, due to absorption of the X-ray [71]. As described by Brindley [17], microabsorption effects occur only if a critical particle size is exceeded and it can be mitigated with a correction method incorporating μ coefficients and particle sizes. However, investigation of this correction method by other authors [135] lead to the conclusion that additional error may easily be introduced, because of the high sensitivity to the estimated particle size. To avoid this correction, on can perform an ultra-fine grinding of the sample.

In the current study, the chosen corundum standard has a smaller linear attenuation coefficient than those of the clinker phases, as shown in Table 4.4.

Phase	ρ (g/cm^3)	μ^* (cm^2/g)	μ (cm^{-1})
Corundum	3.98	30.9	123
Alite, M_3	3.17	97.9	311
Alite, $<M_1>$	3.14	97.9	310
Belite, β	3.31	90.6	302
Belite, α'	3.29	90.6	298
$Alum_{cubic}$	3.04	86.7	264
$Alum_{ortho}$	3.06	83.1	255
Ferrite	3.74	134.6	504
Free Lime	3.35	120.5	403
Periclase	3.58	27.9	100

Table 4.4. Physical properties of clinker phases determined from the crystal structures used in this study (set S2): density ρ, mass attenuation coefficient μ^*, and linear attenuation coefficient $\mu = \rho\mu^*$.

The high measured levels of non-quantified contents can be explained by an underestimation of the absolute content of clinker phases (having higher μ coefficients). Because of controversy regarding the Brindley correction and the technical limitations with respect to grinding, the internal standard method was not further pursued in this study.

External Standard Method

The external standard method consists of separately measuring the diffraction profile of the studied sample and the standard, in the same machine conditions. Conventional Rietveld refinements are then performed on both scans and the results are post-processed, as described by Jansen *et al.* [59]. The diffractometer constant, G, is first calculated with Eq. (4.4) using the refinement results obtained for the standard, i.e., the scale factor S_{st}, the density ρ_{st} of the unit cell, the volume V_{st} of the unit cell, the mass attenuation coefficient μ_{st}, and the known weight fraction of the crystalline phase in the standard π_{st} (sometimes assumed to be 100%).

$$G = \frac{S_{st}\rho_{st}V_{st}^2\mu_{st}}{\pi_{st}} \tag{4.4}$$

The absolute weight fraction, π_j, is then calculated for each j=1...n crystalline phase of the sample with Eq. (4.5) along with the refinement results (S_j, ρ_j and V_j) used as inputs. The mass attenuation coefficient of the sample, μ_{mix}, is either calculated from chemical composition measured with X-ray fluorescence, or estimated with a weighted average over the crystalline phases, $\mu_{mix} \approx \sum_j^n \hat{\pi}_j\mu_j$ [108].

$$\pi_j = \frac{S_j\rho_jV_j^2\mu_{mix}}{G} \tag{4.5}$$

After determination of absolute proportions for all crystalline phases, π_j, the non-quantified content π_{nc} is determined by difference, as shown in Eq. (4.6).

$$\pi_{nc} = 1 - \sum_j^n \pi_j \tag{4.6}$$

In this study, the standard is the NIST α-alumina corundum (SRM 674, further distributed as SRM 676). Crystalline content of this standard was not initially included in its certificate, and values ranging between ~91.8% and ~98.2% are found in different

publications [135,133,24,82]. In light of this variability, lower and upper bounds were calculated for non-quantified contents measured in this study, along with an average value.

As presented in Table 4.5, results for the reference clinker SRM 2688 indicate an average non-quantified content of 10.7%±1.8%. This result is in general agreement with the literature where amorphous contents for clinkers usually range between 3.3% and 25% [72,116,133,82,68,60,65]. More precisely, values of 7.3%±2.1% [116] and 8.0%±0.5% [68] were published for the NIST RM-8488, a discontinued reference clinker superseded by the SRM 2688. These values point toward the lower bound measured in this study, which is consistent as the authors do not specify the amorphous content of their α-alumina standard (thus probably assuming it to be null). This comparison thus supports our procedure for estimation of the non-quantified content.

Parameter	Lower Bound	Average	Upper Bound
π_{st} (%)	98.2	95.0	91.8
π_{nc} (% ± 95 CI)	7.6 ± 1.8	10.7 ± 1.8	13.7 ± 1.7

Table 4.5. Non-quantified content determined for reference clinker SRM 2688 with the external method. Disagreement in literature about exact crystalline content of the NIST α-alumina corundum is responsible for lower and upper bounds. Confidence interval, *CI*, of 95% is obtained with combinations of three scans for the reference clinker and three scans for the standard.

4.3 X-Ray Fluorescence and the Bogue Calculation

X-ray fluorescence (XRF) analyses were performed to measure bulk chemical composition of the studied clinkers and to attempt to derive their mineralogical composition with the Bogue calculation. As no XRF instrument was directly available, samples were sent at two external laboratories: a laboratory providing general analytical services, lab L1, and an associated laboratory at commercial cement plant, lab L2.

4.3.1 Bulk Chemistry

In order to validate the measurements of the external laboratory, the NIST reference clinker SRM 2688 was sent for analysis along with the studied samples. The oxide composition provided by the two laboratories, x_{L1} and x_{L2}, are presented in Table 4.6 along

with the information values published in the NIST certificate, x_0 [86]. The relative error, δx, is calculated for each phase and laboratory, considering x_0 values as the true values.

Oxides *(wt%)*	NIST	Lab L1		Lab L2	
	x_0	x_{L1}	δx_{L1} (%)	x_{L2}	δx_{L2} (%)
CaO	66.50	70.26	*6*	66.77	*0*
SiO_2	22.68	19.63	*-13*	21.71	*-4*
Al_2O_3	4.90	3.80	*-22*	4.64	*-5*
Fe_2O_3	4.07	4.37	*7*	3.98	*-2*
MgO	0.98	0.69	*-30*	0.90	*-9*
SO_3	0.31	0.24	*-23*	0.33	*6*
Na_2O	0.11	0.11	*0*	0.22	*104*
K_2O	0.35	0.40	*14*	0.41	*16*
TiO_2	0.24	0.25	*4*	0.21	*-12*
P_2O_5	0.08	0.07	*-13*	0.08	*1*
Mn_2O_3	0.03	-	-	0.02	*-32*
SrO	0.13	0.17	*31*	0.17	*27*
LOI	0.21	-	-	0.52	*148*
Na_2O_{eq}	0.34	0.37	*10*	0.49	*44*

Table 4.6. Oxides weight percent measured by XRF and loss on ignition, *LOI*, for the NIST reference clinker SRM 2688. Information values provided in the NIST certificate, x_0, [86] are compared with the results provided by to external laboratories, x_{L1} and x_{L2}. The relative error, δx, is calculated considering the NIST values as the true values and equivalent alkalis are calculated according to ASTM C150-04 [10]: $Na_2O_{eq} = Na_2O + 0.658K_2O$.

As expected, the cement plant laboratory L2 provided results with good accuracy. The relative error is 5% or less on the main four clinker oxides. On the other hand, the laboratory L2 performed poorly with errors reaching more than 20% for the same phases. In light of these results, only measurements from the lab L2 are further considered in this study. However, it is worth noting that the error on minor and trace elements may be elevated, particularly for Na_2O and loss on ignition, *LOI*, which are overestimated by more than 100%.

4.3.2 Clinker Composition Parameters and The Bogue Calculation

Clinker bulk compositions measured by XRF are commonly interpreted in the cement industry with composition parameters and the Bogue calculation. As defined in Taylor [121], the composition parameters are also used for reverse calculation of the raw materials proportions required to obtain predetermined clinker compositions.

A first important parameter is the lime saturation factor *LSF* as detailed in Eq. (4.7), in which the chemical formulas also represent the weight percentages of the given phases.

Typical *LSF* values for clinkers are between 0.92 and 0.98 (up to 1.02 is considered acceptable for modern clinkers). This parameter governs the alite to belite ratio and values over 1.0 indicate that free lime is likely to be present in the clinker. However, the LSF is only an approximation, in part because it neglects minors constituent and do not account for ionic substitutions. The modified *LSF** is a variation which accounts for Mg substitution in alite, as detailed in Eq. (4.8).

$$LSF = \frac{CaO}{2.8SiO_2 + 1.2Al_2O_3 + 0.65Fe_2O_3} \tag{4.7}$$

$$LSF^* = \begin{cases} LSF * \dfrac{CaO + 0.75MgO}{CaO} & for\ MgO < 2\% \\ LSF * \dfrac{CaO + 1.50MgO}{CaO} & for\ MgO > 2\% \end{cases} \tag{4.8}$$

The other two composition parameters are the silica ratio *SR* and the alumina ratio *AR*, as described in Eq. (4.9) and Eq. (4.10) [121]. The *SR* characterizes the proportion of silicates in the clinker and values between 2.0 and 3.0 are obtained for normal types of clinkers. Higher values indicate low amount of liquid phases in the kiln, which makes the clinker harder to burn. On the other hand, the *AR* governs the ratio of aluminate to ferrite phases in the clinker, and values between 1.0 and 4.0 are typical of conventional clinkers.

$$SR = \frac{SiO_2}{Al_2O_3 + Fe_2O_3} \tag{4.9}$$

$$AR = Al_2O_3/Fe_2O_3 \tag{4.10}$$

In addition to composition parameters, the Bogue calculation is used to determine the potential phase composition of clinkers from their bulk chemistry. Different variants exist for this calculation and the version used in this study is described in the ASTM standard C150-04 [10]. In this version, the ideal chemistry is assumed for the four major phases (C_3S, C_2S, C_3A and C_4AF) and free lime is not subtracted from the CaO content.

Table 4.7 presents results for the reference clinker SRM 2688 calculated from the bulk chemistries provided by NIST and by the external laboratory L2. If the experimental composition parameters are in good agreement with the reference values (error $\delta x_{L2} \leq 5\%$), it is not the case with the phase composition determined with the Bogue calculation.

Parameter	NIST	Lab L2	
	x_0	x_{L2}	δx_{L2} (%)
Composition Parameters			
LSF	0.91	0.95	*5*
LSF*	0.92	0.96	*5*
SR	2.53	2.52	*0*
AF	1.20	1.17	*-3*
The Bogue Calculation (wt%)			
C_3S	58.7	69.0	*17*
C_2S	20.7	10.2	*-51*
C_3A	6.1	5.6	*-9*
C_4AF	12.4	12.1	*-2*

Table 4.7. Composition parameters and results of the Bogue calculation for the NIST reference clinker SRM 2688. The composition parameters, as described by Taylor [121], include the lime saturation factor *LSF*, the modified *LSF** which allow for Mg substitution in alite, the silica ratio *SR* and the alumina ratio *AR*. The Bogue calculation is performed according to ASTM C150-04 [10].

The results indicate that the Bogue method is very sensitive to the error in the input values: propagation of errors smaller than 5% for bulk composition resulted in errors reaching 50% in the phase composition. Following this observation, the Bogue calculation was not further investigated nor used for comparison in this study. Also, it was not considered worth investigating variants of method (e.g., the modified Bogue calculation [122]) to improve the accuracy of the calculation itself, as the propagation of errors would be similar with these variants.

4.4 Chapter Summary

In this chapter, experimental methods typically used in the cement industry for clinker characterization were described. First, scanning electron microscope imaging was detailed for investigation of clinker microstructure (i.e., phases particularities, porosity, particles sizes). Automated image analysis was also implemented to measure apparent size distributions. Second, X-ray diffraction and the Rietveld refinement method were described to identify and quantify the mineralogical phases. The reference clinker material NIST SRM 2688 was used to validate both the refinement procedure and the external standard method used to assess the non-quantified content. Third, X-ray fluorescence was performed at external laboratories to measure the bulk chemistry. Accuracy was investigated with the NIST reference clinker SRM 2688 and relatively low error ($\leq$ 5%) was found for the four

main clinker oxides. However, estimation of potential phase composition with the Bogue calculation was found to be inadequate. The propagation of errors resulted in errors up to 50% for the four main phases. Overall, the methods presented in this chapter are those generally used in the characterization of cement clinkers.

Chapter 5

Statistical Electron Micro-Probe Analyses

Quality control of clinkers at cement plants is usually limited to the assessment of the bulk chemistry and the abundance of the main phases (i.e., alite, belite, aluminate, and ferrite). However, new developments in clinker engineering have shown that cements with lower grinding energy and higher reactivity can be obtained by chemical substitutions in the clinker main phases [70,77]. Monitoring of the chemistry of the clinker phases may thus become part of the quality control. In this context, a new method is proposed to assess in a single experiment the chemistry of clinker phases, their relative abundance and the bulk chemistry of the clinker. As presented in the following chapter, the method is based on statistical interpretations of electron microprobe spot analyses performed over a representative sample surface. This chapter focuses on the identification of the phases based on their chemistry. Additional analyses regarding the abundance of the phases and the bulk chemistry are further detailed with clinker results in Chapter 9.

5.1 Experimental Protocol

Chemical analyses were performed on the polished samples with a *JEOL JXA-8200 Superprobe* electron probe microanalyzer coupled with a wavelength dispersive X-ray spectrometer. The accelerating voltage was set to 15 kV and the beam current to 10 nA. The beam diameter was 1 μm and the counting time was 10 s per element. The following elements were measured for each spot analysis on the polished surface, after background correction: *Ca*, *Si*, *Al*, *Fe*, *S*, *Mg*, *Na*, *K*, and *O*. The calibration of the instrument was performed with the following standards: synthetic diopside for *Al*, *Na*, *Si*, *Ca* and *Mg*; high purity hematite for *Fe* and *O*; nickel sulfide for *S*; and synthetic orthoclase for *K*.

The raw data was corrected for matrix effects with the CITZAF package implemented in the probe software [8], using the $\phi(\rho z)$-method: stopping power, back-scatter corrections and $\phi(0)$

from Love and Scott; mean ionization potential from Berger and Seltzer; Heinrich's tabulation of mass absorption coefficients; and Armstrong's modified equations for absorption and fluorescence corrections [49,45]. Preliminary testing revealed large deviations in the quantitative determination of the oxygen content, which appeared to be very sensitive to local surface defects, such as grain boundaries or cracks. The oxygen was alternatively determined from stoichiometry, which was possible because of the anhydrous nature of the probed material.

5.2 Application to Heterogeneous Materials

5.2.1 Interaction Volume

Each EPMA spot analysis is assumed to be representative of an interaction volume, which corresponds to the extent of the energy distribution exciting the X-rays inside the bulk of the sample. This interaction volume is a function of the accelerating voltage and the composition and density of the probed material [45]. Monte Carlo simulations were performed with the non-commercial program CASINO [30] to determine the interaction volume for cement clinker with an accelerating voltage of 15 kV. As illustrated in Fig. 5.1a, the interaction volume is characterized by trajectories of scattered electrons. The density of these electrons decreases as the distance from the electron beam increases. There is no unique definition for the size of the interaction volume, but the measurements are usually less sensitive to the last 10% of electron trajectories, as stated by Goldstein [45]. The interaction radius is defined in this study as the radius including 90% to 95% of emitted X-rays for all elements measured, as illustrated in Fig. 5.1b for pure C_3S.

The interaction volume radii simulated for the main pure clinker phases are presented in Table 5.1. Thus, the interaction radius for clinker range between 0.5 and 0.75 μm, when probing a polished surface with a 15kV electron beam.

Phase	C_3S	C_2S	C_3A	C_4AF
$R_{90\%}$ (μm)	0.57	0.53	0.55	0.49
$R_{95\%}$ (μm)	0.73	0.69	0.71	0.64

Table 5.1. Interaction volume radii for the pure main clinker phases. The bounds for radii are associated to interaction volumes including 90% and 95% of the emitted X-rays for all elements of the probed phase.

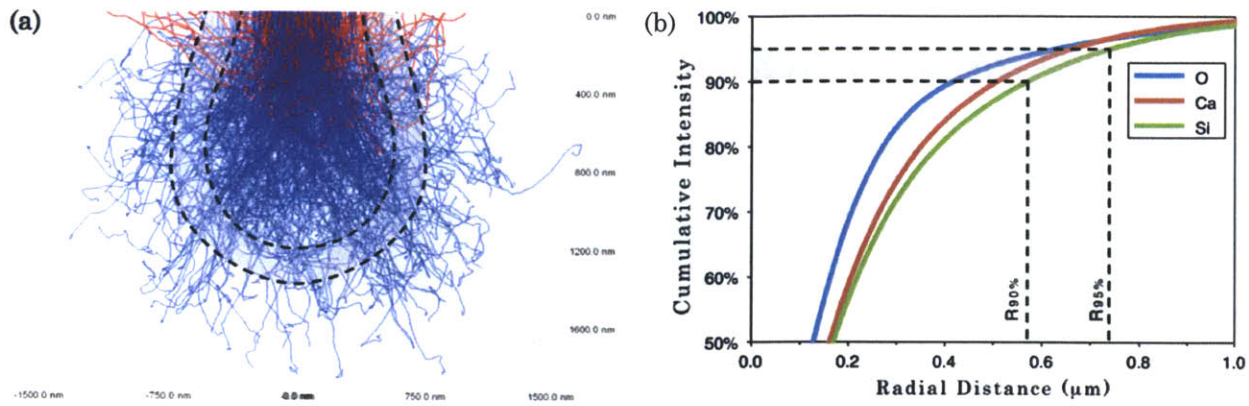

Fig. 5.1. (a) Trajectories of 500 electrons simulated with CASINO for a 15kV electron beam probing pure C_3S. (b) Cumulative intensity of electron trajectories as a function of radial distance from the electron beam (simulation with CASINO for 10^5 electrons with a 15kV beam probing pure C_3S). The gray bands on both figures represent the bounds including 90% to 95% of the emitted characteristic X-rays for silicon, the element with the largest interaction volume.

5.2.2 Statistical Grid Measurements

In heterogeneous materials such as clinkers, a mixture of phases is measured when the interaction volume is not entirely inscribed in the domain of a single phase. If the scale of the heterogeneities is much larger than that of the interaction volume, imaging can be used to focus spot measurements on a single phase within acceptable error. In the case of similar scaling, an alternative method is the random probing at discrete locations on a grid l_xxl_y that spans a specific region on a material surface L_xxL_y (e.g., Fig. 5.2). This method results in probing both pure phases and mixtures of phases. The estimation of statistically distinct chemical species and their properties can then be performed with advanced statistical tools.

In this work, the total number of grid points, N, was set to 1024 to obtain a statistically adequate number of measurements. The grid spacing, L, was adjusted to ensure that each grid covers a representative surface defined by the criterion $d \ll L\sqrt{N}$, in which d is the characteristic size of largest heterogeneities in the sample. Therefore, a 60 μm spacing was used for bulk and coarsely powdered samples, and a 30 μm spacing for finely powdered samples, covering surfaces of ~2x2 mm² and ~1x1 mm², respectively. As illustrated in Fig. 5.2 for bulk sample *B-C3*, the sampling grid covers a surface much greater than the largest heterogeneities, i.e., pores. Finally, replicate analyses are performed at random locations on

each sample. The replicate grids are identified with lowercase letters following sample name (e.g., grid *C-C2b* is the second grid done on coarsely ground sample of clinker *C2*).

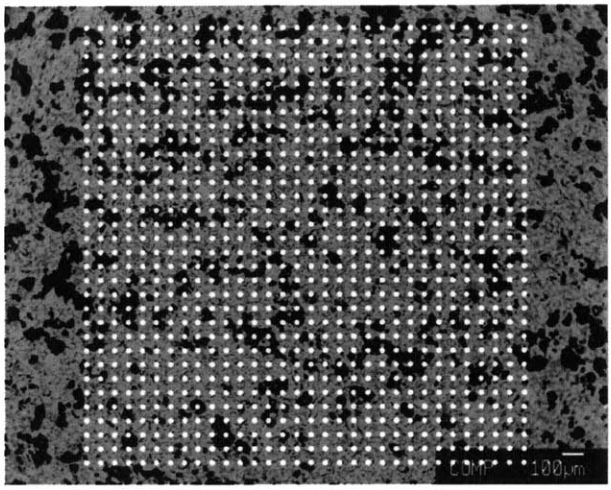

Fig. 5.2. Schematic of the EPMA grid superposed on a BSE image of bulk sample *B-C3*. The white dots represent the sampling grid, which covers a clinker surface composed of the clinker matrix in gray and the porosity in black.

5.3 Statistical Data Analyses

After measurement of chemical composition for each grid, the data is sieved to remove noise and a clustering algorithm is used to identify the different phases probed.

5.3.1 Data Sieving: "Signal" and "Noise" Separation

Each $i=1...N_0$ data point is validated with a criterion applied to its analytical total, T_i, defined as $T_i = \sum_{k=1}^{p} c_{ik}$, where c_{ik} is the weight fraction of the $k=1...p$ measured element. If all the elements are measured (and adequately calibrated), the analytical total for valid probes should be $T_i \in [100 \pm 2]\%$ [45]. A perfectly flat surface as well as a homogenous material within the interaction volume are required to meet this range of analytical totals, which is likely not to be the case of our heterogeneous epoxy-impregnated specimens. Measurements on epoxy are expected to give lower analytical totals because epoxy contains carbon, which is not measured in the EPMA analyses. In addition, deviations in analytical totals may be associated with surface irregularities generated during polishing at the interfaces between clinker and epoxy.

A different approach is developed to sieve the "signal" (valid probes of the clinker matrix) from the "noise" (probes with significant deviation of the analytical total). The distribution of T_i is assumed to follow a Gaussian mixture model [124,78] of two components. As illustrated in Fig. 5.3a, the first component is the "signal", which consists of a number of points associated with a sharp peak having low deviation. On the contrary, the "noise" component is assumed to represent the fraction of the measurements contributing to the wide spread in the analytical totals. Then, clustering is performed to determine the bounds separating the N valid points of the "signal" from the N_0-N epoxy related "noise" points (see Fig. 5.3b).

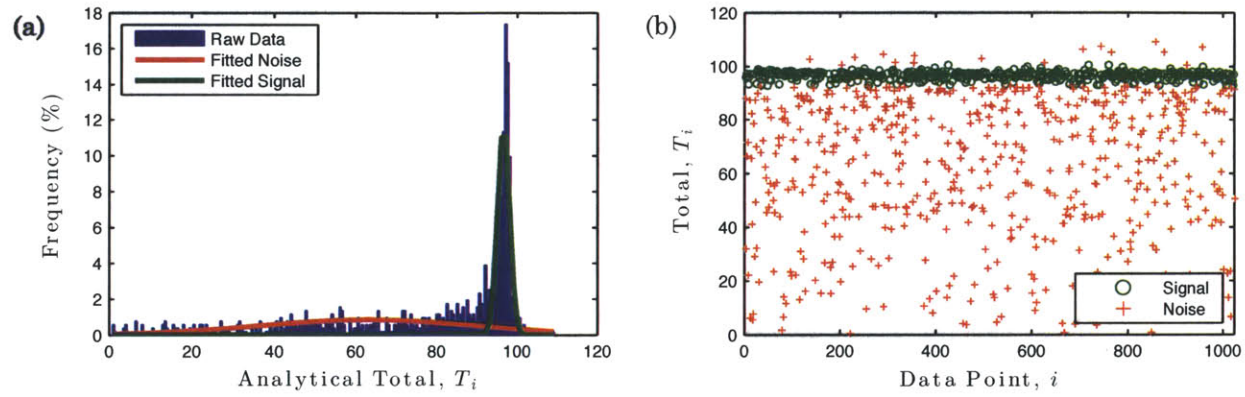

Fig. 5.3. (a) Histogram of analytical totals for the N_0 data points probed on the coarsely ground sample *C-C2a*, with an overlay of the fitted two components Gaussian mixture distribution. (b) Results of the clustering applied to sieve the "signal" from the "noise".

5.3.2 Phases Clustering

Following data sieving, each $i=1...N$ data point is expressed in atomic percent with its chemical composition vector $\boldsymbol{x}_i=[Ca_i; Si_i; Al_i; Fe_i; S_i; Mg_i; Na_i; K_i; O_i]$. In addition, each of these data points may belong to one $j=1...n$ chemical phase having the average composition vector $\boldsymbol{\mu}_j$. Hence, statistical analysis is carried out on the grid dataset with the aim to estimate the number of statistically significant phases, as well as their vector of mean composition $\boldsymbol{\mu}_j$, their covariance matrix $\boldsymbol{\Sigma}_j$ and their associated fraction π_j. Recent literature reports a variety of deconvolution strategies applied to achieve similar clustering [26,128,129]. We employ here multivariate mixture modeling supported with the Bayesian Information Criterion (BIC) [38]. Based on Finite Gaussians Mixture Model, *FGMM* (see Eq. (5.1) and (5.2)), the estimation of the parameters is carried out according to the

Maximum Likelihood (ML) function, via the Expectation Maximization (EM) algorithm [29], with the aid of the publicly available *R* package called MCLUST [37,36]. The clustering is carried out with respect to the four main elements of cement clinkers: *Ca*, *Si*, *Al* and *Fe*.

$$f(\boldsymbol{x};\boldsymbol{\psi}) = \sum_{j=1}^{n} \pi_j f_j(\boldsymbol{x};\boldsymbol{\mu}_j,\boldsymbol{\Sigma}_i) \tag{5.1}$$

$$\sum_{j=1}^{n} \pi_j = 1,\ \pi_j \geq 0 \tag{5.2}$$

5.4 Chapter Summary

This chapter describes a method to assess the chemical composition of clinker phases with the combined use of electron probe microanalyzes (EPMA) and advanced statistical tools. Experimental details were first presented followed by the implications of probing heterogeneous materials. The interaction volume radius was simulated to be between 0.5 and 0.75 μm when probing clinker phases. Randomly located probes can therefore represent either a single phase or a mixture of phases. To identify the number of pure phases and their properties, a statistically relevant number of probes need to be performed over a representative surface of each sample. The datasets can then be deconvoluted with the MCLUST algorithm. An intermediate data-sieving step was also proposed based on Gaussian mixture clustering. This sieving is applied to the analytical totals in order to separate the "signal" from the "noise" (associated with significant deviation of the analytical totals). Finally, this chapter consisted of a general presentation of the method, which will be further extended based on the results for clinkers in Chapter 9.

Chapter 6

The Microscratch Test

The fracture toughness, K_c, is a material property that quantifies the ability to resist fracture propagation from existing cracks (or defects). This property is of prime importance for all problems related to linear-elastic fracture, whether fracture is considered desirable (e.g., grinding) or not (e.g., airplane integrity). If conventional fracture testing methods are available (e.g., the three-point bending test or the Vickers indentation test), their use for multi-scale investigations of materials like cement clinkers is limited. A potential alternative method is the use of the microscratch test, as developed for homogeneous materials by Akono *et al.* [5,7,4,6]. This method has the potential to be extended to a large range of scales, with variations of the experimental protocol. Different variants are investigated in this study with the objective to adapt the method for measuring fracture properties of heterogeneous clinkers at their different characteristic scales.

6.1 Microscratching Basics

The theoretical basics of microscratching are presented in this section, based on the developments by Akono *et al.* [5,7,4,6]. The schematic in Fig. 6.1 shows the microscratch test performed with an axisymmetric indenter probe forced at a fixed velocity over a surface in the x direction to create a scratch path. A progressively increasing vertical force, F_V, is prescribed and the resulting horizontal force, F_T, is recorded along with the penetration depth of the indenter tip, d. The following sections describe the method employed to calculate the fracture toughness from the measured quantities (d and F_T) and the tip geometry, using the linear elastic fracture mechanics (LEFM).

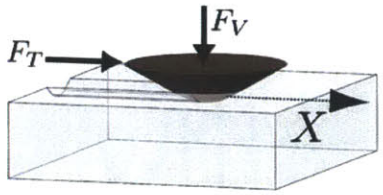

Fig. 6.1. Three dimensional schematic of the microscratch test [4]. An indenter tip is forced into a surface in the x direction with prescribed velocity and vertical force F_V. The resulting horizontal force F_T and the penetration depth d are recorded during the experiment.

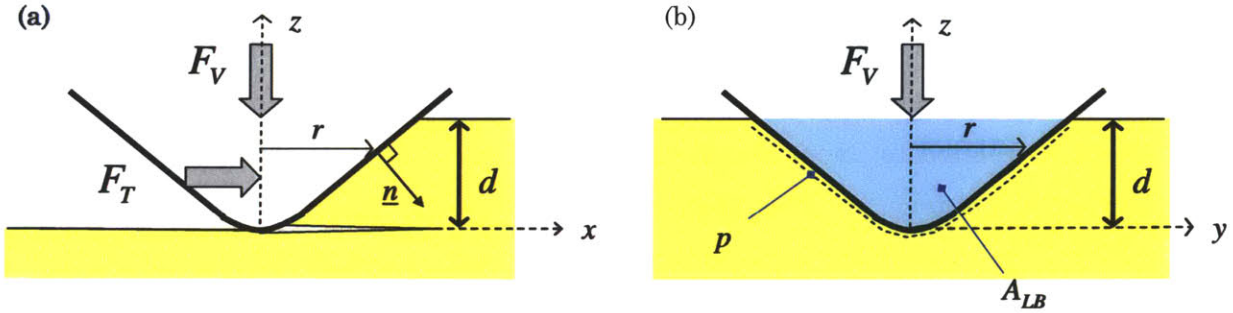

Fig. 6.2. Schematics of the microscratch test with an axisymmetric probe [6]: (a) side view and (b) front view. A semi-circular horizontal crack plane is assumed at the probe tip, which is forced into the surface at a penetration depth d.

6.1.1 General Axisymmetric Probe

The scratch test model is developed considering an axisymmetric probe. A single variable monomial function describes the probe shape in a coordinate system having origin at the probe tip:

$$z = Br^{\epsilon} \tag{6.1}$$

where B is the height at unit radius and ϵ is the degree of the homogeneous function. The application is focused on the conical ($\epsilon = 1$; $B = \cot\theta$) and the spherical ($\epsilon = 2$; $B = 0.5/\mathrm{R}$) probes. To determine geometric quantities useful in further development, the outward unit normal $\underline{n}$ is developed:

$$\underline{n} = -\frac{\epsilon B r^{\epsilon-1}\cos\phi}{\sqrt{1+(\epsilon B r^{\epsilon-1})^2}}\underline{e}_r + \frac{1}{\sqrt{1+(\epsilon B r^{\epsilon-1})^2}}\underline{e}_z \tag{6.2}$$

for $r \in [0, (d/B)^{1/\epsilon}]$ and $\phi \in [-\pi/2, \pi/2]$, along with the differential line element, ds, and the surface element, dS:

$$ds = \sqrt{1+(\epsilon B r^{\epsilon-1})^2}\, dr \tag{6.3}$$

$$dS = r\, d\phi\, ds \tag{6.4}$$

These geometric relations are then combined to define the contact area, A_{LB}, and the perimeter p of the probe, both projected in the scratch direction ($n_x = \underline{n} \cdot \underline{e}_x$). These two quantities are shown in Fig. 6.2b.

$$A_{LB}(d) = -\int_{(S)} n_x\, dS = \frac{2B\epsilon}{\epsilon+1}\left(\frac{d}{B}\right)^{(1/\epsilon)+1} \tag{6.5}$$

$$p(d) = \int ds = \left(\frac{d}{B}\right)^{1/\epsilon} \beta \tag{6.6}$$

with the dimensionless parameter β:

$$\beta = 2\int_0^1 \sqrt{1+(\epsilon d)^2\left(\frac{d}{B}\right)^{-2/\epsilon} x^{2\epsilon-2}}\, dx \tag{6.7}$$

6.1.2 Contour Integral Method

The contour integral method, initially proposed by Rice [99], is extended for determination of the energy release rate, G, associated with the fracture process occurring during the scratch test. The following section recalls these developments by Akono *et al.* [5,4].

As illustrated in Fig. 6.2, the existence of fracture planes surrounding the scratch probe, $\Gamma = p\ell$, is hypothesized, with p the perimeter of the probe and ℓ the crack length in the x direction. The dissipation rate is then calculated based on the spontaneous change of potential energy, dE_{pot}, due to the creation of the surface Γ:

$$D = -\frac{dE_{pot}}{dt} = Gp\frac{d\ell}{dt}; \quad G = -\frac{\partial E_{pot}}{\partial \Gamma} \tag{6.8}$$

The change in potential energy is then estimated from the perspective of an observer attached to the propagating crack. Two sources of potential energy changes are considered: the variation in free energy density ψ in a material volume V enclosing the crack tip, and

the energy release that is convectively transported at a speed $\underline{V} \cdot \underline{n} = -\dot{\ell} n_x$ passed the (fixed) observer.

$$\frac{dE_{pot}}{dt} = \int_V \frac{\partial \psi}{\partial t} dV - \int_A \psi \dot{\ell} n_x \, dA \tag{6.9}$$

where A is the closed boundary of V. For a linear elastic material ($\psi = \frac{1}{2}\sigma_{ij}u_{i,j}$ with σ_{ij} the symmetric stress tensor, $u_{i,j}$ the displacement gradient), using the divergence theorem allows a change of the volume integral into a surface integral:

$$\int_V \frac{\partial \psi}{\partial t} dV = \int_V \sigma_{ij} \frac{\partial u_{i,j}}{\partial t} dV = \int_A t_i \frac{\partial u_i}{\partial x} \dot{\ell} \, dA \tag{6.10}$$

where $t_i = \sigma_{ij} n_j$ are surface tractions, and considering that the displacement rate seen by the moving observer is equal to $u_{i,t} = \dot{\ell} u_{i,x}$ in a displacement-controlled fracture test. The combination of equations (6.8) to (6.10) yields the following expression of the energy release rate:

$$G = \frac{1}{p} \int_A \left(\psi n_x - t_i \frac{\partial u_i}{\partial x} \right) dA \tag{6.11}$$

According to the classical form of the J-integral [99], in planar cracks the fracture perimeter coincides with the fracture width, $dA = p \, ds$. The difference between these lengths is rather chosen to apply this technique to different scratch geometries. For the scratch problem, a closed volume is chosen that includes the probe-material interface, the stress-free surface at the top ($n_x = 0$; $t_i = 0$), the stress-free fracture surfaces in prolongation of the scratch probe surface ($n_x = 0$; $t_i = 0$), and the closing material surfaces far from the probe-material interface ($\psi = 0$; $u_{i,x} = 0$); so that the only contribution to the surface integral comes from the probe-material interface S:

$$G = \frac{1}{p} \int_{(S)} \left(\psi n_x - t_i \frac{\partial u_i}{\partial x} \right) dS \tag{6.12}$$

Physically speaking, the energy release so defined can be associated with the energy stored in a material domain in front of the scratch probe.

6.1.3 Fracture Criterion

The stress field in front of the scratch probe is estimated to be uniaxial in the x direction:

$$F_T = \int_{(S)} \sigma_{xx} n_x dS \tag{6.13}$$

The shear stresses were also investigated by Akono and Ulm [6], but experimental validation proved the uniaxial stress field to be adequate [4]. In this case, the free energy is $\psi = (1/2)\kappa\sigma_{xx}^2/E$ and the work of the stress vector along $\partial u_x/\partial x = \epsilon_{xx}$ is $\sigma_{xx} n_x \epsilon_{xx} = \kappa\sigma_{xx}^2 n_x/E$, where E is the Young's modulus, $\kappa = 1$ for plane stress and $\kappa = 1 - \nu^2$ for plane strain (ν is the Poisson's ratio). Thus, the energy release rate (Eq. (6.12)) is simplified into the following form:

$$G = -\frac{\kappa}{2pE} \int_{(S)} \sigma_{xx}^2 n_x dS \tag{6.14}$$

Assuming a constant stress field over the projected contact area, A_{LB}, the combination of equations (6.5), (6.13) and (6.14) results in:

$$G = \frac{\kappa}{2pA_{LB}E} F_T^2 \tag{6.15}$$

The energy release rate is bounded by the fracture energy, G_f, as described in (6.16). Crack propagation occurs when this critical value is reached. In addition, the fracture energy is also related to the fracture toughness, K_C, (within the limits of LEFM):

$$G \leq G_f = \frac{\kappa}{E} K_c^2 \tag{6.16}$$

The fracture propagation criterion for the scratch test then reads:

$$F_T \leq F_c = K_c \sqrt{2pA_{LB}} \tag{6.17}$$

where F_c is the critical horizontal force for crack propagation. Finally, both the perimeter p and the projected contact area A_{LB} are dependent on the penetration depth d. The probe shape function, f, is thus defined:

$$f(d) = 2p(d)A_{LB}(d) \tag{6.18}$$

6.1.4 Scaling Relations for Conical and Spherical Probes

Any type of axisymmetric probe could potentially be used, but we focus here on conical and spherical probes, as these probe shapes will be used in the experimental application. Based on equations (6.5) to (6.7), the shape functions are determined both for the conical probe ($\epsilon = 1$; $B = \cot\theta$) and for the spherical probe ($\epsilon = 2$; $B = 0.5/\mathrm{R}$):

Conical probe:
$$f(d) = 4\frac{sin\theta}{(cos\theta)^2}d^3 \tag{6.19}$$

Spherical probe:
$$f(d) = \frac{16}{3}\beta\left(\frac{d}{R}\right)d^2R, \quad \beta\left(x = \frac{d}{R}\right) = \sqrt{1+2x} + \frac{1}{\sqrt{2x}}\mathrm{arcsinh}\left(\sqrt{2x}\right) \tag{6.20}$$

In the case of the conical probe, the following self-similar scaling relation is obtained between the scratch penetration depth and the horizontal force:

$$F_c(\lambda d) = \lambda^{3/2}F_c(d) \tag{6.21}$$

On the other hand, the self-similar scaling for the spherical probe is limited by the β coefficient. Nevertheless, $\beta \approx 2$ for small values of $d/R \ll 1$, which results in the linear scaling:

$$F_c(\lambda d) \approx \lambda F_c(d) \tag{6.22}$$

For these types of axisymmetric probes, the self-similar scaling of the scratch force associated with fracture propagation indicates that the measured fracture properties are independent of the probe size and the probed depth, for homogeneous materials.

6.1.5 Experimental Applications

In practice, microscratch tests are performed with a Rockwell diamond indenter probe, which has a geometry consisting of a conical range with a half-apex angle θ of 60° and a spherical tip of radius R. The transition between these two ranges occurs at $d/R = 0.134$, which means that the tip can be approximated by a cone for tests performed at sufficient penetration depths, i.e., $d/R >> 0.134$.

The presence of fracture processes during a microscratch test is verified by determination of the scaling relation between the horizontal force and the penetration depth. The model function $y = a(x - c)^b$ is fitted to the experimental curve $F_T(d/R)$, as illustrated in Fig. 6.3.

As shown in equations (6.21) and (6.22), the theoretical b coefficient is 1 for the spherical range and 1.5 for the conical range. The results presented by Akono *et al.* [4] are generally in agreement with the theory for experiments performed on different materials: the b coefficient varies from 1.11 to 1.20 for the spherical range, and from 1.49 to 1.51 for the conical range. When the maximal penetration depth is close to the transition between the spherical and conical ranges, b has intermediate values between 1.30 and 1.39. Unexpected values are also measured for some materials, such as the Delrin polymer probed in the conical range (b=1.19) and the AISI-1045 metal probed in the transition range (b=1.74). Nevertheless, fracture toughness measured for these two materials is in good agreement with literature values, which suggests that unexpected b coefficients may not be sufficient to invalidate the measurements.

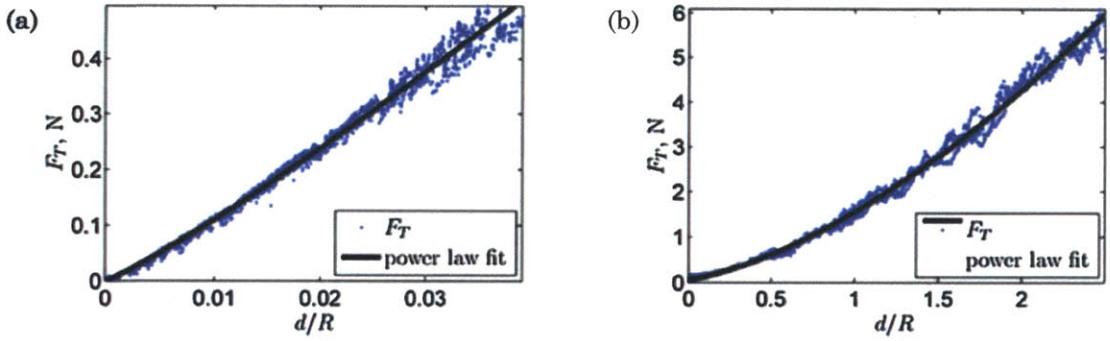

Fig. 6.3. Experimental curves of the horizontal force vs. the penetration depth, with fitted power law functions [4] for (a) fused silica, b=1.11, and (b) paraffin wax, b=1.49

The variability in tip geometries and the possible tip wearing prevents the use of the theoretical tip shape functions. The solution proposed by Akono et al. [4] is to calibrate the tip shape function with a reference material of known K_c. The order of this function depends on the activated range of the tip and a polynomial fitting is performed according to equations (6.23) and (6.24):

Conical range:
$$f\left(\frac{d}{R}\right) = R^3\left[\alpha\left(\frac{d}{R}\right)^3 + \delta\left(\frac{d}{R}\right)^2 + \gamma\frac{d}{R}\right], \alpha \geq 0, \delta \geq 0, \gamma \geq 0. \tag{6.23}$$

Spherical range:
$$f\left(\frac{d}{R}\right) = R^3\left[\delta\left(\frac{d}{R}\right)^2 + \gamma\frac{d}{R}\right], \delta \geq 0, \gamma \geq 0 \tag{6.24}$$

According to Akono *et al.* [4], the coefficient α captures the conical shape of the tip, δ captures the spherical part and γ accounts for the blunting of the tip. Fig. 6.4 illustrates the tip shape function fitting procedure applied for a tip of 200 μm radius. The spherical range is calibrated on fused silica and the conical range on paraffin wax.

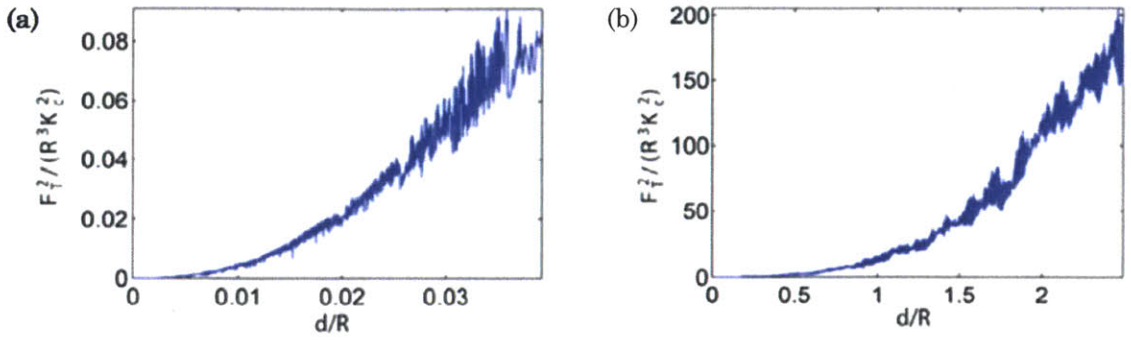

Fig. 6.4. Probe shape function calibration [4] for (a) spherical range with fused silica, $f(d/R) = 54.51(d/R)^2$, and (b) conical range with paraffin wax, $f(d/R) = 13.02(d/R)^3$

Results are in agreement with the theoretical tip shape function for the conical range. The measured α coefficient of 13.02 is similar to the theoretical value of 13.86 calculated with Eq. (6.19) and a half-apex angle of $\theta = 60°$. However, in the spherical range, the experimental data results in $\delta = 54.51$, and the theoretical value is $\delta_{th} \approx 10.7$, based on Eq. (6.20) with $\beta \approx 2$ for $d/R < 0.1$. This difference is not further explained by the authors [4], but the calibration function is used with success to assess fracture toughness of ceramics.

Once the tip shape function f is calibrated, the fracture toughness K_c of other materials may be calculated using Eq. (6.17). As illustrated in Fig. 6.5 for Pyrex and soda lime glass [4], the calculated $F_T/\sqrt{2pA}$ are plotted as a function of the relative penetration depth, d/R. After initial deviation attributed to local plastic deformation [4], the fracture process becomes dominant and the data points converge. The load-independent fracture toughness, K_c, is then calculated by taking the average and standard deviation of $F_T/\sqrt{2pA}$ for $d > d_{max}/2$, as described by Eq. (6.25).

$$K_c = \left\langle \frac{F_T}{[2pA]^{\frac{1}{2}}} \right\rangle \Bigg|_{d > \frac{d_{max}}{2}} \tag{6.25}$$

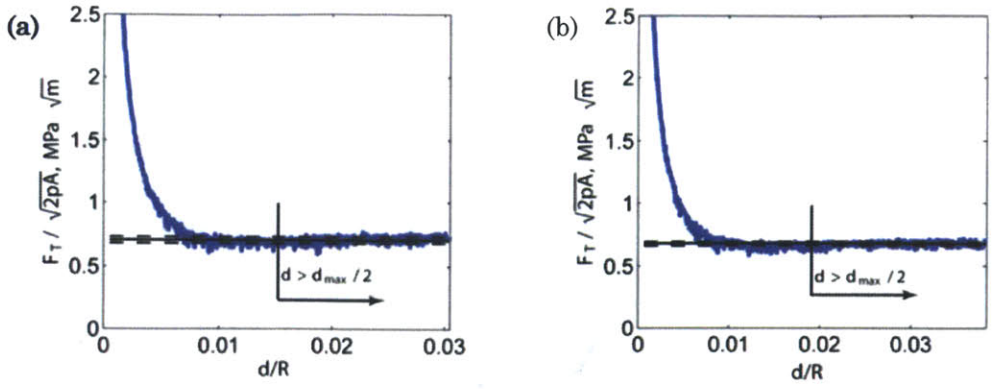

Fig. 6.5. Fracture toughness as a function of the relative penetration depth for (a) Pyrex and (b) soda lime glass. After initial local plastic deformation [4], the convergence of data points indicates a fracture-dominated process. The fracture toughness is averaged from the second half of the curve.

6.2 Reference Materials

In order to calibrate tip shape functions and to validate the scaling of the microscratching method, several reference materials were investigated. These materials are presented in Table 6.1, which also includes the manufacturer of the specimen tested and the literature values for the fracture toughness determined by the conventional three point bending tests. For each material, a range of reference values is provided, along with the literature values used by Akono [4].

Material	Manufacturer	Literature K_c (MPa.m$^{1/2}$)		References
		Range	Akono [4]	
Lexan	Sabic	2.69	2.69	[50]
Fused silica	McMaster Carr	0.58 - 0.7	0.58	[48,137]
Soda lime glass	-	0.7 - 0.8	0.7	[48,21]
Macor	Accuratus	1.53 - 1.9	-	[2,73]
Alumina	Accuratus	3 - 5	-	[2,44,39,21]

Table 6.1. Reference materials used for calibration and validation of the micro-scratch test at different scales. The literature values for K_c are provided along with their references.

6.3 Experimental Protocol

The microscratch tests were performed with a Micro-Combi Tester, *MCT*, distributed by CSM Instruments. This instrument shown in Fig. 6.6 is equipped with a sample holder on a

3 axis stage, an indenter, a set of three optical microscope lenses (5X, 20X and 50X), and sensors to measure forces, displacements and acoustic emissions.

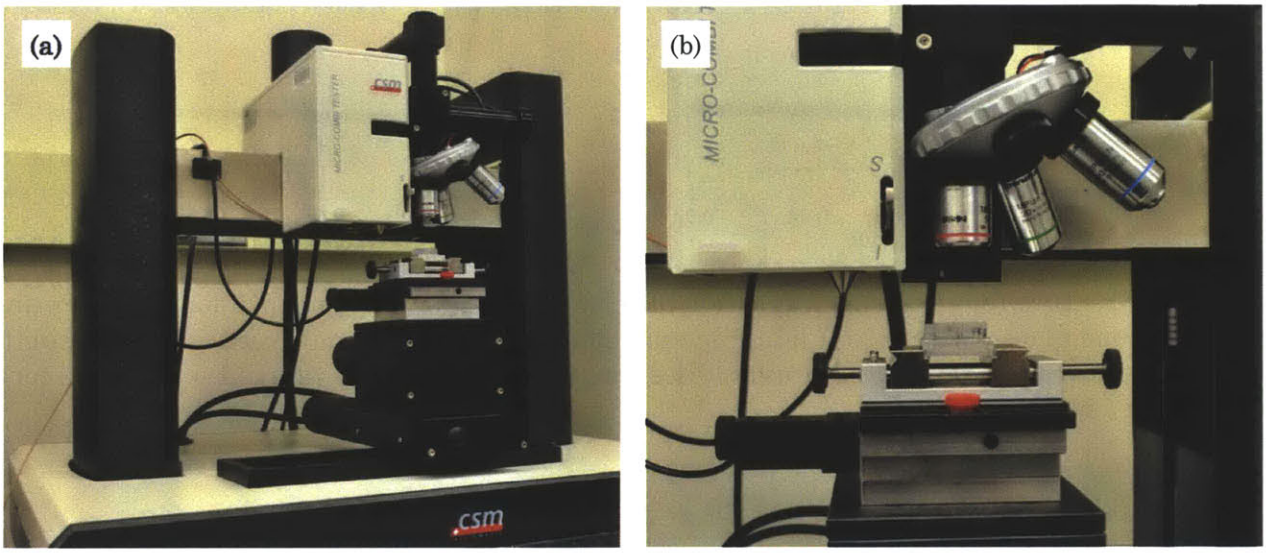

Fig. 6.6. Micro-Combi Tester by CSM Instruments: (a) global view showing the automatic stage (3 axis) and the horizontal support for the instrumentation, and (b) close-up showing the sample, the indenter and the three optical microscope lenses.

The default experimental protocol was defined for the conical and spherical ranges based on previous testing that assessed the validity of these protocols for specific applications. Additional variants will also be investigated in subsequent sections of this study, for probing at the characteristic length scales of cement clinkers.

Conical Range

The default protocol for the conical range is presented in Table 6.2, and it corresponds to the protocol used for polymers by Akono *et al.* [4]. As suggested by Akono [3], the Lexan polymer is used for calibration in replacement of the paraffin wax initially used.

Probe Type:	Rockwell	End Load (N):	30
Material:	Diamond	Loading Rate (N/min):	60
Radius (μm):	200	Scanning load (N)	0.03
		Speed (mm/min):	6
Linear Scratch Type:	Progressive	Length (mm):	3
Begin Load (N):	0.03	Approach speed (%/s):	0.7

Table 6.2. Default experimental protocol for microscratching in the conical range with a tip of 200 μm radius, based on the protocol used for polymers [4].

Spherical Range

The default protocol for the spherical range was previously developed for ceramics [4]. Most parameters are the same as those used for the conical range, with the exception that the vertical force is limited to 7N and the loading rate is set to 14 N/min. In addition, fused silica is used as the reference material for calibration with a fracture toughness value of K_c = 0.58 MPa.m^{½}, according to Akono *et al.* [4].

6.4 Improvements in Experimental Methods

To obtain precise and accurate results, measurements must be performed in strictly controlled conditions. Possible improvements in the experimental methods were identified during this project, and specific investigations were performed regarding the method used to hold the sample in the instrument and the moisture control of Lexan.

6.4.1 Holding the Sample: Circular vs. Rectangular Substrate

As shown in Fig. 6.7a and Fig. 6.9, two types of sample holders jaws may be used with the MCT instrument to accommodate circular and rectangular samples. Before running a microscratch test, the jaws are first tightened around the sample, which is then assumed to be perfectly held in place. Since the depth of the scratch path is measured by the penetration of the indenter tip (relative to a pre-scan of the surface), uncontrolled vertical displacement of the sample during the test would erroneously increase the measured penetration depth.

A reference fused silica specimen was used for calibration in the spherical range. The specimen had a disk shape and the circular holder jaws were initially used, as shown in Fig. 6.7a. However, it was found that the sample did not sit completely on the horizontal surfaces of the holder. The sample was rather held by two contact points as schematized in Fig. 6.7b-c and rotation was possible around the axis crossing these contact points.

As illustrated in Fig. 6.8, measurements performed in these conditions showed high level of variability with respect to the measured penetration depths and horizontal forces. This large variability of the raw data also affected the fitted tip shape functions, which were significantly different for successive series of measurements, as shown in Fig. 6.8c. In this case, only the series *Circ#1* had similar magnitude as the reference by Akono *et al.* [4].

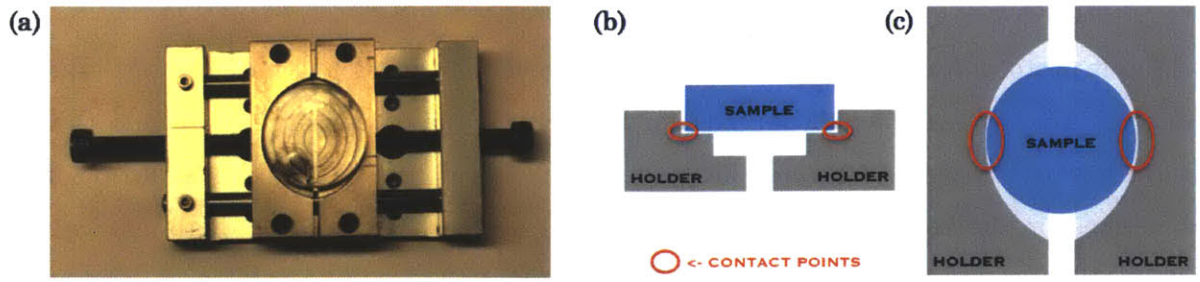

Fig. 6.7. (a) Disk shaped fused silica sample fixed with the circular jaws. Schematic (b) side view and (c) top view of the holder with identification of the two contact points. Rotation of the sample was possible around the axis crossing these contact points.

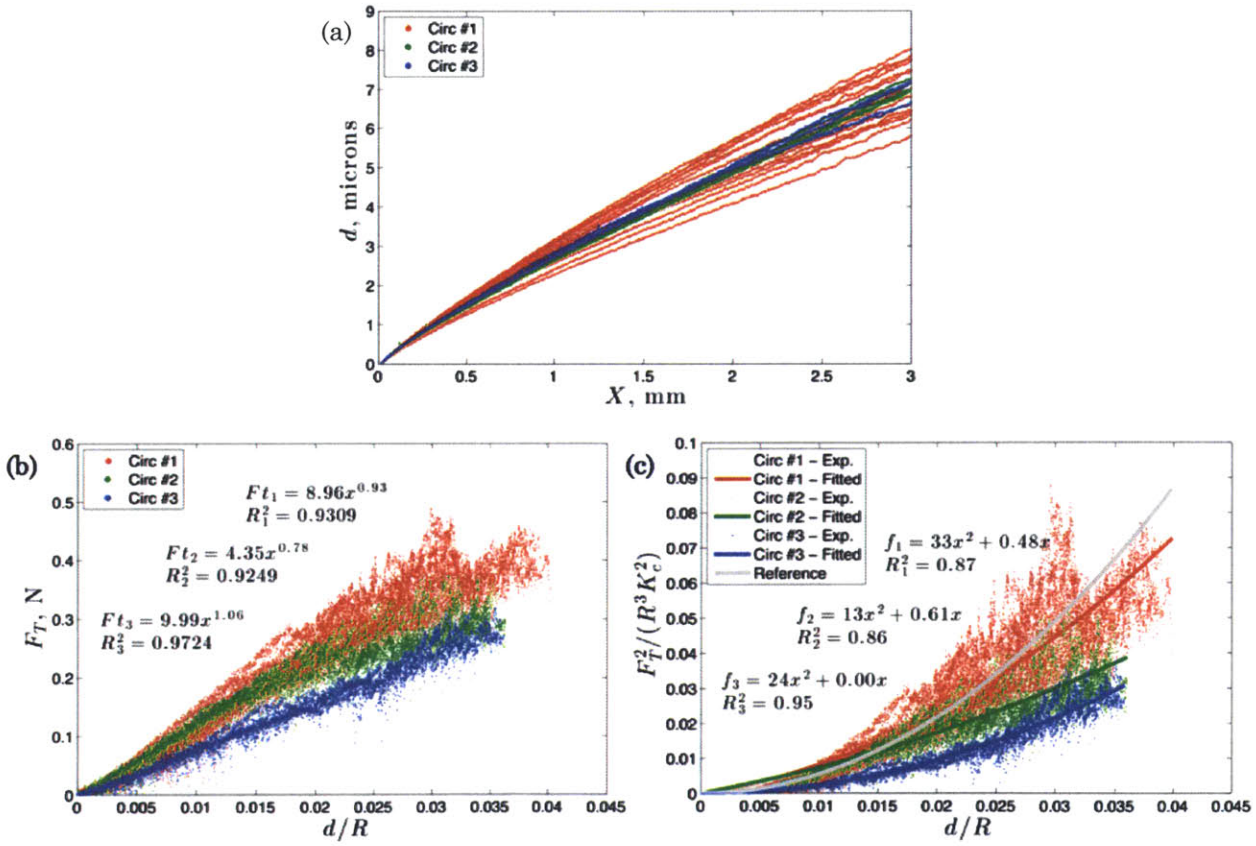

Fig. 6.8. Spherical range calibration on a fused silica sample held with the circular jaws: (a) penetration depth vs. distance, (b) horizontal force vs. penetration depth, and (c) tip shape function fitting.

To avoid any movement of the disk shaped reference sample, a rectangular aluminum plate was machined to have perfectly parallel edges. The sample was fixed with cyanoacrylate glue to the aluminum substrate, which was then firmly held in the rectangular jaws of the instrument, as shown in Fig. 6.9.

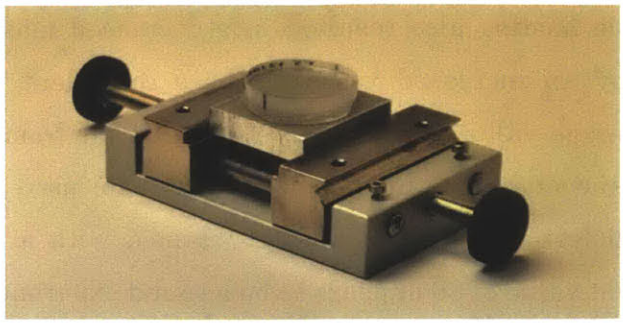

Fig. 6.9. Sample holder clamping a rectangular aluminum base on which a disk sample of fused silica has been glued.

As illustrated in Fig. 6.10, the results obtained with this revised holding method showed very good repeatability. In addition, scaling of the horizontal force and penetration depth was validated with an average fitted value of b=1.01, which was consistent with theoretical value of 1 for the spherical range.

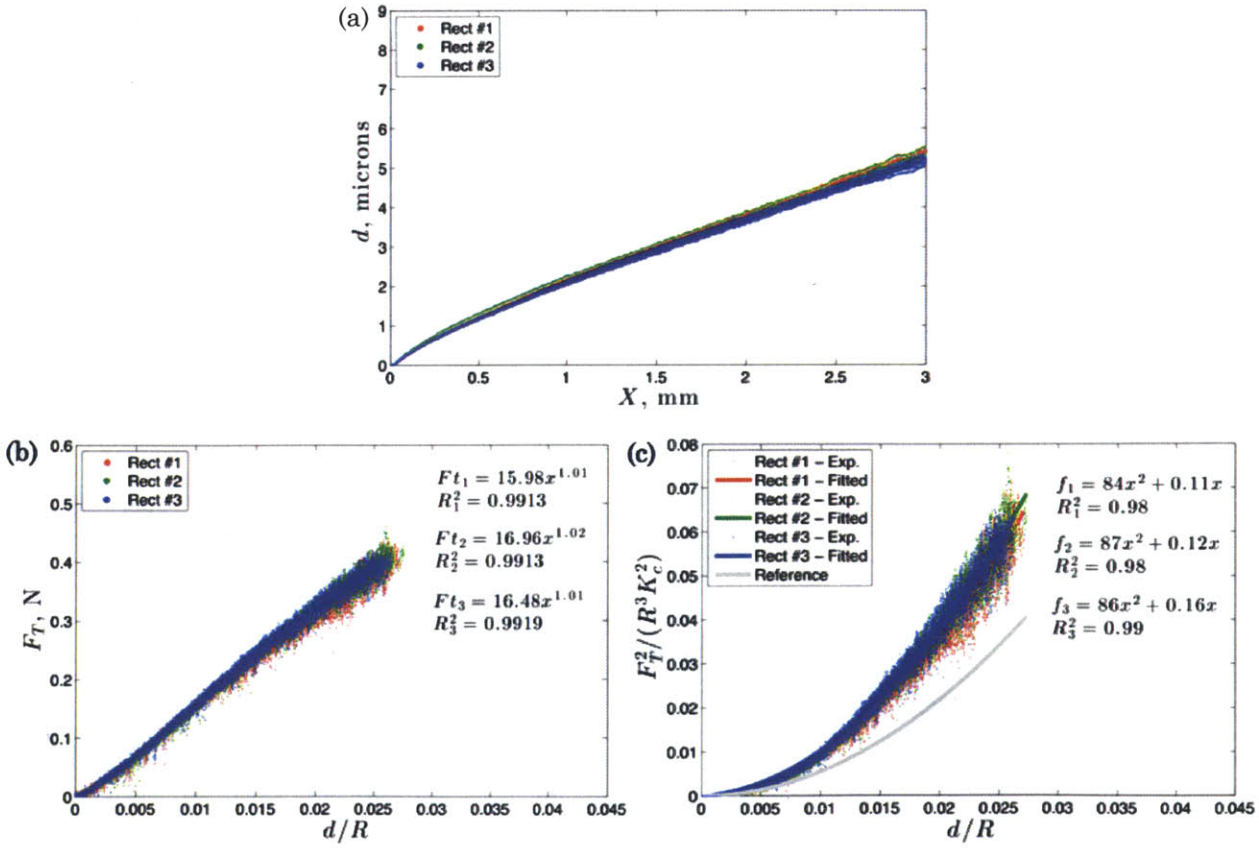

Fig. 6.10. Spherical range calibration on a fused silica sample glued to a rectangular aluminum substrate: (a) penetration depth vs. distance, (b) horizontal force vs. penetration depth, and (c) tip shape function fitting.

However, better sample holding also resulted in a decreased maximal penetration depth, which was reflected by an increased value of the α coefficient for the fitted tip shape functions. With an average value of 86, this coefficient is far from the theoretical value of 10.7 (see section 6.1) and above the published value of 54.5 used as reference in Fig. 6.8c and Fig. 6.9c. Nevertheless, these results were obtained with a rigorous and repeatable method, and α coefficient value of 86 appears to be a sound experimental result.

Overall, this investigation led to the recommendation that the circular jaws should not be used to hold the sample. Instead, disk shaped samples should be glued to a rectangular base to obtain high quality results. Based on these conclusions, all the samples investigated in this study are glued to an aluminum substrate held in place with the rectangular jaws.

6.4.2 Lexan Reference Material: Moisture Control

The calibration of the experimental method is a critical step to obtain reliable results. Calibration materials, such as Lexan, must be well understood and should exhibit consistent properties. Two significantly different trends were observed in the measurements on Lexan, during an investigation aiming to reduce experimental variability in the microscratch test. Several experimental details were investigated without success, until the moisture content of Lexan was found to be of importance [3,102,96,58]. Fig. 6.11 shows measurements on a Lexan specimen before and after isopropanol cleaning. The surface treatment resulted in a shift in the measured horizontal force, F_T, from a maximum value of ~10N up to ~19N. This was accompanied by a reduction of the penetration depth, d.

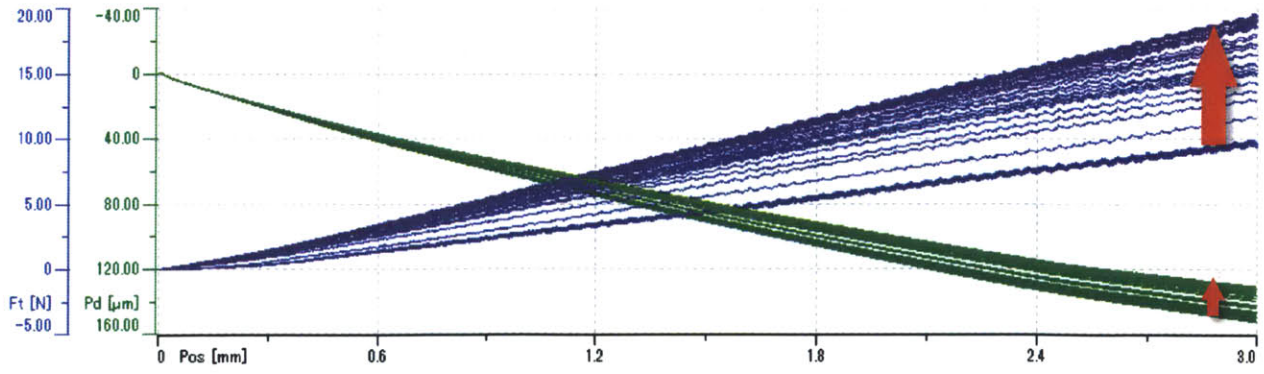

Fig. 6.11. Microscratching raw results for a Lexan specimen showing the influence of isopropanol cleaning. The horizontal force Ft shifts from the lower trend to the higher trend, while penetration depth d is reduced.

An additional study was performed to understand this unexpected behavior, with the aim to determine (1) the effect of moisture content on the properties of Lexan, (2) the rate of Lexan moisture absorption and (3) the optimal Lexan specimen conditioning method.

6.4.2.1 Experimental Program

A series of Lexan specimens were prepared with different conditioning methods and were tested at different time intervals. Each conditioning step is described in the following paragraphs and the characteristics of all tested specimens are presented in Table 6.3. The preparation procedures are inspired from a new procedure released by Akono [3].

The specimens were first cut with a table saw from a single 12 mm thick sheet of Lexan polycarbonate resin thermoplastic produced by SABIC Innovative Plastics (see Fig. 6.12a).

Alconox and water cleaning were performed in the following way: (1) removal of plastic covers; (2) ultrasonication in a 1% Alconox solution for 5 min; (3) ultrasonication in water for 5 min; (4) rinsing under running water; and (5) removing surface water with moisture-free compressed air. On the other hand, isopropanol cleaning consisted in gently wiping the Lexan surface with soft cloth soaked with isopropanol; this wiping was performed 10 times at intervals of 30s to allow for evaporation.

Cleaned samples were dried in an oven set at 125°C for the prescribed period [102,58]. After drying, the specimens were cooled either in a desiccator or in a glass jar with a tight plastic lid. Finally, the specimens were mounted on machined aluminum bases with cyanoacrylate glue (Fig. 6.11b) before testing.

Specimen	Size (cm^2)	Cleaning	Drying (hr)	Cooling	Scratching (# @ t[hr])
Wat1	3.2x4.2	Alconox + Water	No	No	~8 @ ~0,1,2,4,8,24,168
Iso1	3.2x4.2	Isopropanol	No	No	~8 @ ~0,1,2,4,8,24,192
Dry1	3.2x4.2	Alconox + Water	24	Dessicator (20min)	~8 @ ~0,1,2,4,8,24,168
Dry2	3.2x4.2	Alconox + Water	24	Dessicator (24hr)	24 @ ~24
Dry3	3.2x4.2	Alconox + Water	24	Glass jar (24hr)	24 @ ~24
Dry4	3.2x4.2	Alconox + Water	96	Dessicator (20min)	~8 @ ~0,2,120
Ako1	2.5x2.5	Alconox + Water	24	Glass jar (24hr)	24 @ ~24

Table 6.3. Preparation details for the Lexan specimens investigated in this study. All the samples were prepared by the author, with the exception of sample *Ako1* which was prepared and tested by Akono.

For comparison reasons, the specimen *Ako1* was prepared and tested by Akono following her new procedure: alconox and water cleaning, 24 hr drying at 125°C, 24 hr cooling in glass jar before performing a matrix of 24 scratches.

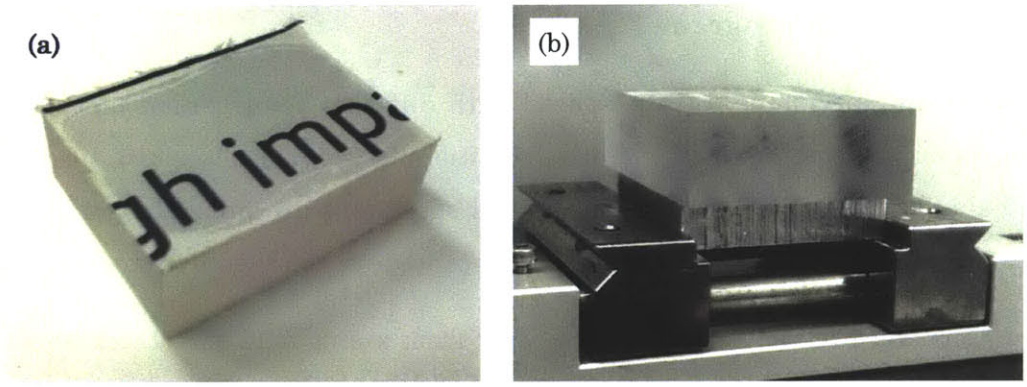

Fig. 6.12. (a) Specimen cut with the table saw (3.2x4.2cm²), before removal of the protective plastic covers. (b) Conditioned sample mounted on the machined aluminum base and placed in the Micro Combi Tester rectangular holder.

After sample conditioning, testing was performed with the default parameters for the conical range as previously described. A single 200 μm Rockwell diamond indenter, tip number E269, was used for all the tests in this study. The number of scratches per series varied between 8 and 24, and the scratches were performed with a 7 mm offset (in x and y directions) from the corners to avoid edge effects. After the first series of scratches, the samples were stored in the laboratory environment, where the ambient relative humidity was approximately 20-25%.

6.4.2.2 Results

The comparison of the raw results is achieved with the maximal horizontal force, F_{Tmax}, and the maximal penetration depth, d_{max}, at the end of the scratch path (see the red circles in Fig. 6.11). The time t is recorded for each scratch, considering $t = 0$ at the end of sample conditioning.

As shown in Fig. 6.13, the maximal horizontal force F_{Tmax} is dependent on the conditioning method used. For the moist specimen *Wat1* (not dried after water cleaning), the measured F_{Tmax} is low with values around 10N. Drying the specimens in an oven increases the measured F_{Tmax} up to 12-18N. On the other extreme, horizontal forces reach 20N for the specimen *Iso1* treated with isopropanol, which is 100% higher than for the moist samples.

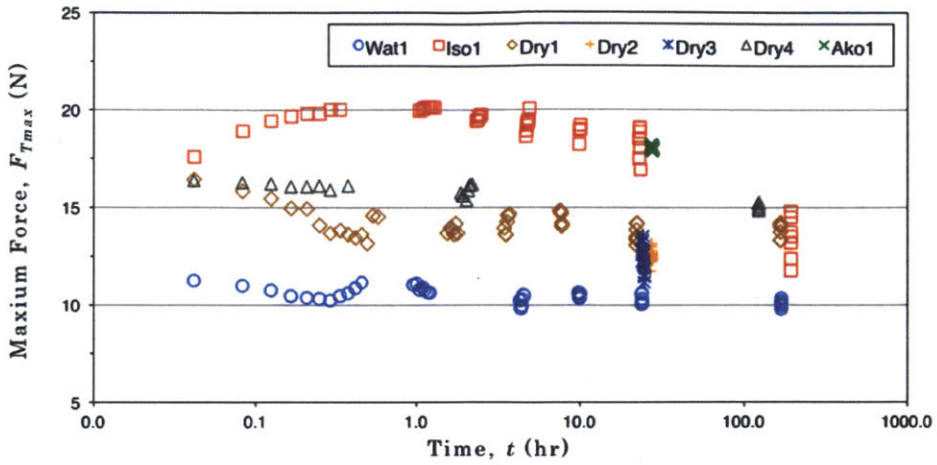

Fig. 6.13. Maximal horizontal force, F_{Tmax}, as a function of time, t, for different conditioning methods. The moist specimen shows a low F_{Tmax}, whereas oven-drying results in a middle range F_{Tmax} and the highest values are obtained for the specimen wiped with isopropanol.

The measured maximal penetration depths, d_{max}, are presented in Fig. 6.14 for the same set of samples. The observations made for F_{Tmax} also generally apply for d_{max}, with the difference d_{max} is increased with moisture. However, the moisture effect is less severe for d_{max} with relative variations are below 10% (compared to 100% for F_{Tmax}).

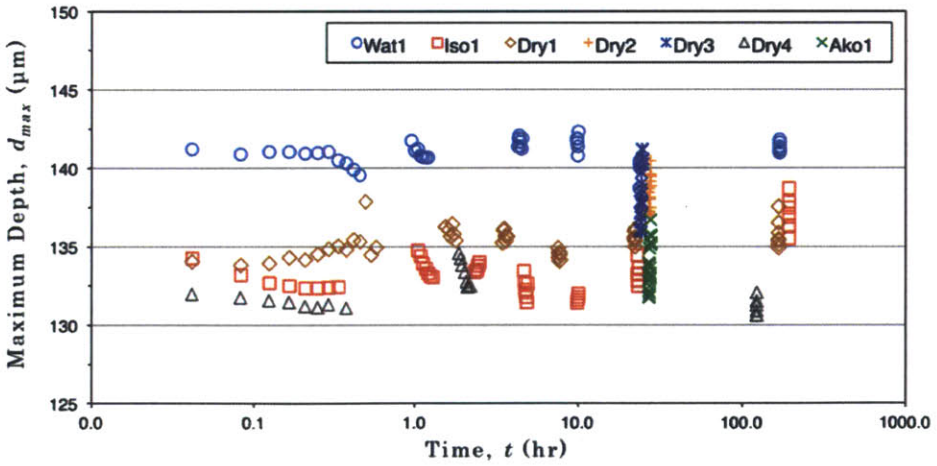

Fig. 6.14. Maximum penetration depth, d_{max}, as a function of time, t, for different conditioning methods. The moist specimen exhibit lower d_{max} than the dried specimens.

To link these results to the calibration function (i.e., Eq. (6.23)), the α coefficients are plotted in Fig. 6.15. Calibrating on moist Lexan results in $\alpha \approx 5$, whereas using dryed samples generally results in $\alpha \approx [7.5, 18]$ and isopropanol treatment raises α up to ~22.

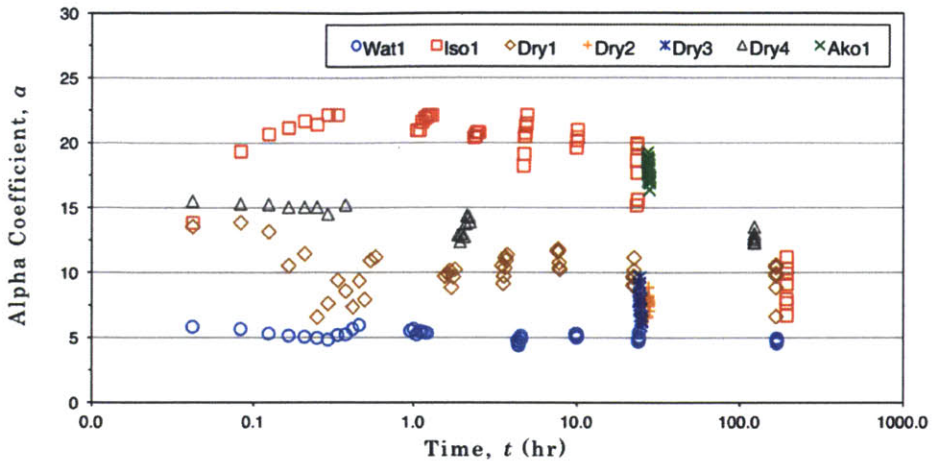

Fig. 6.15. Alpha coefficient, α, as a function of time, t, for different conditioning methods. The α coefficient is higher, up to a factor four, for the specimen treated with isopropanol compared to the moist specimen.

6.4.2.3 Discussion

Effect of Moisture on Properties

It is known from the plastic industry that "the majority of thermoplastic resins, including sheet products, are hygroscopic, which means that they absorb moisture. Moisture builds up in the polymer sheet during manufacturing, transportation and storage. In the 'as extruded' condition it presents no problem" [102]. However, the measured properties change significantly as a function of the moisture content, as shown in Fig. 6.13 and Fig. 6.14. Higher horizontal force and lower penetration depth are measured for the dried specimens (e.g., *Dry4*) compared to the moist specimen (i.e., *Wat4*), which indicates that Lexan resistance to scratching reduces with moisture absorption. In addition, the F_{Tmax} values may be used to qualitatively describe the moisture of the tested Lexan specimens, as all other experimental details were kept constant.

Lexan Drying

The drying method as performed by Akono [3] (2.5x2.5 cm^2 specimens dried at 125°C for 24 hr, then cooled for 24 hr in a sealed glass jar) was found to be successful, as the Lexan specimen *Ako1* showed elevated and repeatable resistance to scratching.

Similar drying performed on larger 3.2x4.2 cm^2 specimens *Dry1*, *Dry2* and *Dry3* was found to be incomplete, resulting in middle-range resistance to scratching and lower repeatability.

A more stringent drying regime may be required as suggested in the *Lexan Sheet Processing Guide by SABIC* [102]. The recommended drying for 12 mm thick Lexan sheets is 48 hr at 125°C ± 3°C in a hot-air circulating oven changing the oven air volume 6 times per hour. Other authors are even more conservative [58], preparing Lexan samples of 2 mm thickness and drying for 48 hr at 125°C with temperature ramping resulting in a total process of 82 hr. In an attempt to mitigate the absence of air circulation and ramping options for the oven used in this study, the specimen *Dry4* was dried for 4 days at 125°C. As illustrated in Fig. 6.13, higher F_{Tmax} values were obtained, but the full resistance of Lexan was not reached. Therefore, it is advised to limit the size of the Lexan pieces, as for specimen *Ako1*.

An alternative approach consists of drying the surface with isopropanol. In this case, isopropanol replaces the water in the porosity of Lexan because of its lower surface tension [64]. After evaporation of both liquids, the Lexan surface is drier and exhibits higher resistance to scratch, as shown with specimen *Iso1* in Fig. 6.13.

Moisture Variations with Time

Lexan is known to absorb moisture as stated by *Port Plastics*: "A note of caution - polycarbonate sheet begins absorbing moisture immediately upon removal from the predrying oven" [96]. Ambient moisture absorption was observed for the specimen *Dry1* tested 20 minutes after removal from the oven. In contrast, the opposite is observed for specimen *Iso1*, as the isopropanol and moisture progressively evaporate in the first hour.

Ambient moisture seems to be absorbed very slowly over a long period of time by the specimens *Dry1* and *Dry4* in comparison to the specimen *Iso1*, which mechanical properties decrease rapidly. This suggests that isopropanol drying is only effective on a shallow layer of material, in comparison to deeper oven drying.

Surface Cleanness

To reduce variability in the measurements, the surface should be kept clean and undamaged, as suggested by Akono [3] and illustrated in Fig. 6.16a for a water-cleaned specimen. Fig. 6.16b illustrates the surface of specimen *Iso1* where scratches of small dimensions were introduced by the cloth used during the isopropanol treatment. Even if this surface was lightly damaged, repeatable and stable results were obtained between 0.5 and 3 hours after surface conditioning.

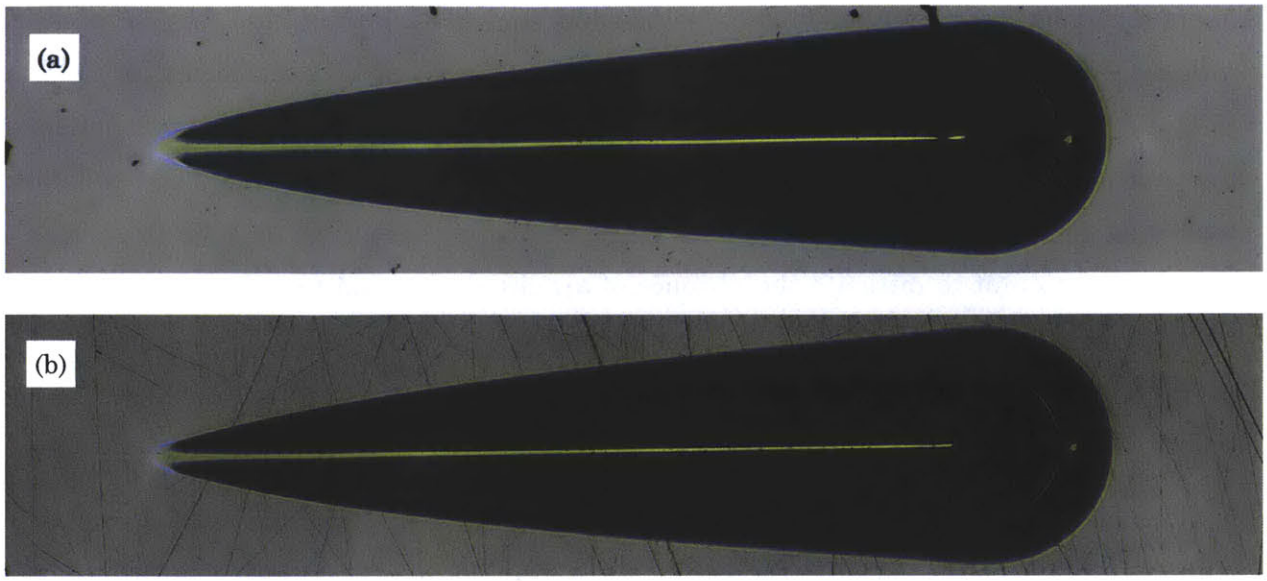

Fig. 6.16. Lexan surfaces and scratch paths of specimens (a) *Dry1* and (b) *Iso1*. Water cleaning procedure allows removal of most of the surface impurities, whereas the cloth used in the isopropanol treatment introduces small scratches on the surface.

Isopropanol Surface Treatment

Moisture removal with isopropanol was envisaged further based on the results for specimen *Iso1*, and considering that Lexan is generally compatible with alcohols [102]. To validate this conditioning procedure, the exact same protocol used for sample *Iso1* was repeated for additional specimens (*Iso2*, *Iso3*, *Iso4*, *Iso5*). However, the moisture removal was not systematically achieved for this series of tests, as shown in Fig. 6.17. Following such a discrepancy in the measured values, isopropanol treatment is not recommended.

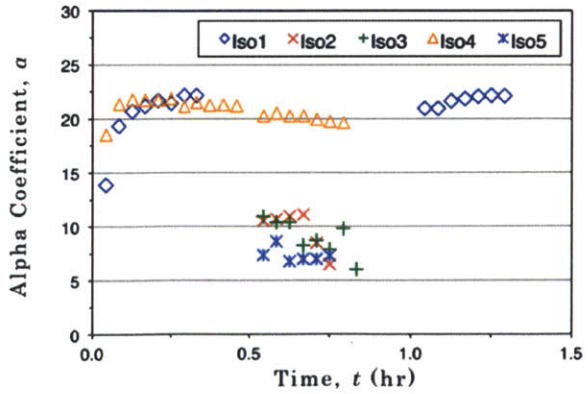

Fig. 6.17. Evolution of coefficient α over time t for five different samples conditioned with the exact same isopropanol cleaning procedure.

6.4.2.4 Conclusions

In conclusion, better understanding of the effect of moisture on Lexan properties has been acquired through this investigation and the findings are summarized below.

Lexan resistance to scratching is strongly dependent on moisture content. The measured horizontal force (i.e., F_{Tmax}) exhibits a reduction up to 50% between moisture free specimens and moist specimens. Thus, very precise control of Lexan moisture is required before using this material for calibration, or for investigations of other possible experimental variability.

After initial conditioning and stabilization in the first hour, the rate of moisture absorption is dependent on the conditioning method. The dried samples seem relatively stable for several days, whereas a faster decay in mechanical performances is observed for specimens cleaned with isopropanol. In addition, uneven moisture absorption may be responsible for increased variability.

Sample conditioning according to Akono's new procedure [3] with small-sized specimens is found to limit the decrease of Lexan scratch resistance associated with moisture. On the other hand, isopropanol cleaning is not recommended, as the same procedure applied to different specimen may lead to drastically different results. Following these observations, Akono's new procedure [3] is used in this project to perform conical calibration with Lexan. Finally, the use of an alternative material with lower sensitivity the environment could be envisaged in further investigations.

6.5 Downscaling of the Method

An interesting advantage of the microscratch test over conventional fracture toughness measurement methods resides in the possible scaling for investigations at any characteristic scale of complex materials. In this project, the millimeter scale is tested with an indenter probe of 200 μm radius used in the conical range [4]. In addition, downscaling is investigated with the spherical range of the same 200 μm probe and with smaller probes (R = 50 and 20 μm) used both in the spherical and the conical ranges. These investigations at smaller scales focus on the measurement of ceramics properties and Table 6.4 summarize the experimental protocols tested.

Tip Radius (μm) Range	200 Spherical	50 Conical	50 Spherical	20 Conical	20 Spherical
Max d (μm)	6	15	2.2	9	0.8
Max d/R	0.025	0.3	0.045	0.45	0.04
Max Fv (N)	7	15	4	4	1
Length (mm)	3	1.5	0.4	0.1	0.04
Load rate (N/min)	14	60	60	24	15
Velocity (mm/min)	6	6	6	0.6	0.6

Table 6.4. Experimental protocols used to investigate downscaling of the microscratch test with 200, 50 and 20 μm probes. The choice of parameters is partly based on the expected applications at the characteristic scales of clinkers.

6.5.1 Spherical Range of the 200 μm Probe

As demonstrated for ceramics by Akono *et al.* [4], the microscratch test can be used in the spherical range of a 200 μm tip to characterize hard brittle materials. These materials are not suited for microscratching in the conical range, because large chipping occurring in front of the tip invalidates the measurements. Before using the method with materials of unknown properties, the tip was calibrated with fused silica and tests were performed on soda lime glass (SLG), Macor and aluminum oxide ceramic (alumina). The fracture toughness of these ceramics range from 0.58-0.8 to 3-5 MPa.m^{½} (see section 6.2).

The fracture toughness convergence plots are presented in Fig. 6.18 and the results are compared in Table 6.5 with those published by Akono *et al.* [4]. For the materials tested, the fitted b coefficients were generally consistent with the expected values for fracture processes performed with a spherical probe ($b \approx 1$), except for Macor. As discussed in section 6.4.1, the rectangular jaws were used in this study and this led to a different tip shape parameter α = 86, compared to 54.5 in [4]. Nevertheless, accurate K_c results were obtained for soda lime glass (as in [4]) which validates the proposed use of the rectangular jaws to hold the sample.

Material	Max d/R	Fitted b coefficient	Tip shape function or predicted K_c (MPa.m^{½})	Literature K_c (MPa.m^{½})
Fused silica	0.025	1.01	$f = 86x^2$	0.58 - 0.7
Soda lime glass	0.02	1.21	$K_c = 0.71 \pm 0.03$	0.7 - 0.8
Macor	0.03	1.31	$K_c = 0.84 \pm 0.04$	1.53 - 1.9
Alumina	0.012	1.18	$K_c = 1.93 + 0.16$	3 - 5
Fused silica *	0.04	1.11	$f = 54x^2$	0.58
Pyrex glass *	0.03	1.16	$K_c = 0.68 \pm 0.02$	0.63
Soda lime glass *	0.04	1.20	$K_c = 0.71 \pm 0.03$	0.70

Table 6.5. Measured and literature values of K_c for the tested ceramics. Results with a star (*) are the results published by Akono *et al.* [4]

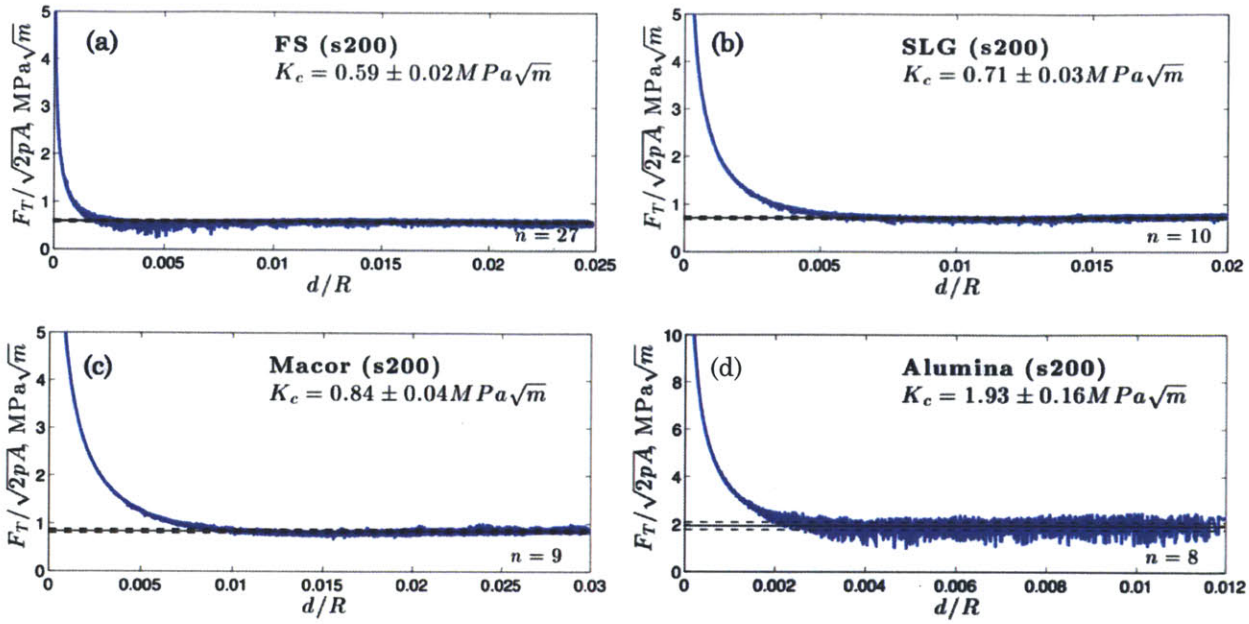

Fig. 6.18. Fracture toughness measured in the spherical range of the 200 μm probe (identified as *s200*) on (a) fused silica, (b) soda lime glass, *SLG*, (c) Macor, and (d) alumina.

The results for Macor and alumina exemplify the limits of applicability of the spherical range microscratching with the 200 μm probe. The method seems adequate for materials with fracture toughness similar to that of the calibration material (e.g., soda lime glass or pyrex), but the accuracy is limited for the other tested ceramics. This may be attributed to microtexture, as further investigated in the following sections.

6.5.2 Spherical Range for Probes of Radius from 200 to 20 μm

The fused silica, soda lime glass, Macor and alumina samples were tested with probes of decreasing radius, i.e., 50 and 20 μm. Fig. 6.19 illustrates that homogeneity of the reference fused silica is preserved over the probed scales, and the microscratching results are thus expected to be consistent over the scales. Similar homogeneity was also identified for soda lime glass up to the smallest tested scale, which is shown in Fig. 6.20a. However, porosity was observed in the alumina specimens. This microtexture was expected to affect mainly the larger scales, as scratching with the 20 μm tip was performed between the pores (see Fig. 6.20c). No homogeneity was found in Macor at the smaller scales, and Fig. 6.20b shows the large chipping occurring during scratching because of the material microstructure. For this reason, Macor was not considered in the tests with the 50 and 20 μm probes.

In addition, downscaling of the microscratching method was correlated with a reduction in the signal-to-noise ratio, as illustrated for soda lime glass in Fig. 6.18b and Fig. 6.21. This could be explained by the increased effect of surface irregularities at small scale. Thus, the precision of the results at the smaller scales was expected to be lower.

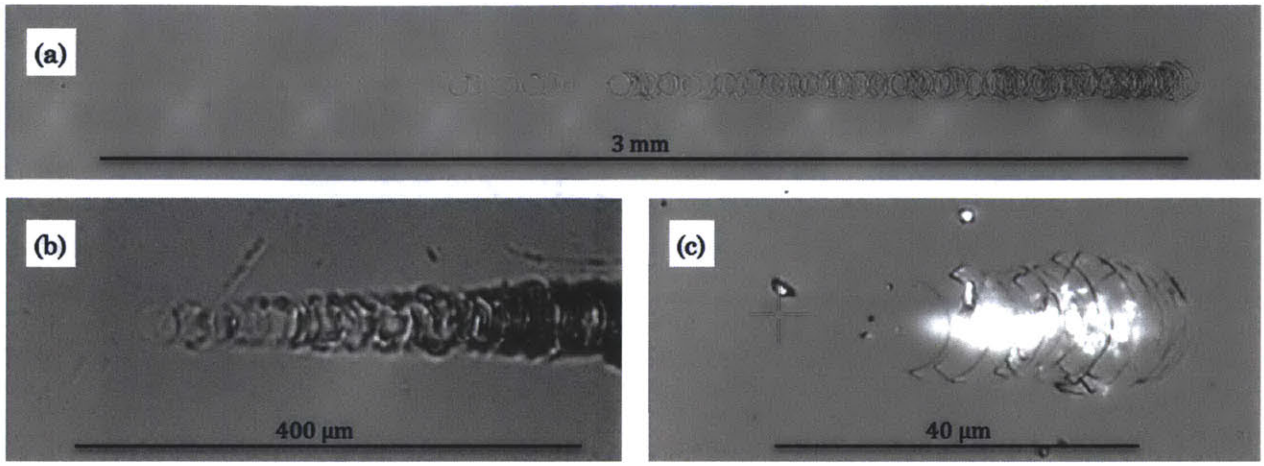

Fig. 6.19. Scratch imprint for spherical range microscratching performed on fused silica with (a) the 200 µm probe, (b) the 50 µm probe, and (c) the 20 µm probe.

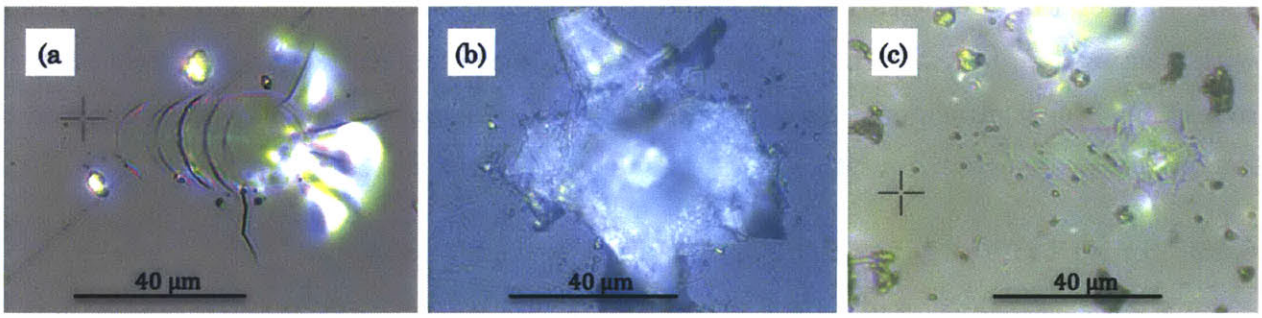

Fig. 6.20. Scratch imprint for spherical range microscratching performed with a 20 µm probe on (a) soda lime glass, (b) Macor, and (c) alumina.

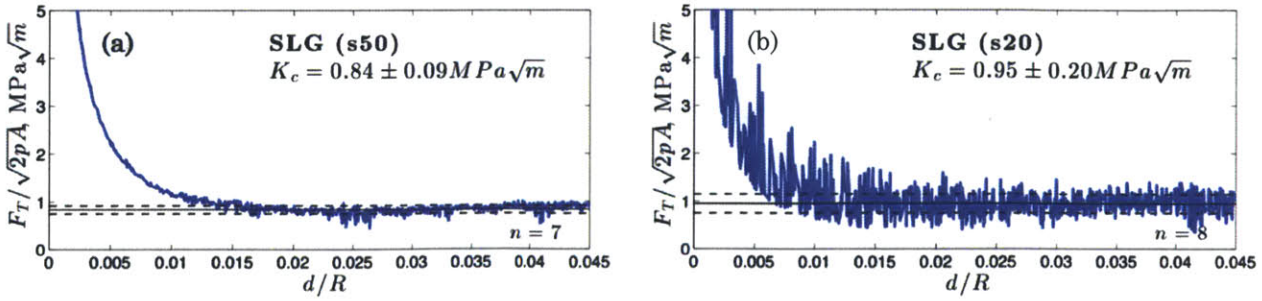

Fig. 6.21. Fracture toughness measured on soda lime glass in the spherical range of (a) the 50 µm probe, *s50*, and (b) the 20 µm probe, *s20*.

Fig. 6.22 presents the measured fracture toughness plotted as a function of the literature reference values for the three probed scales (the results also figure in Table 6.6). In this figure, the error bars on the reference K_c describe the range of published values (see section 6.2) and the error bars on the measured K_c represent the standard deviations, as defined in section 6.1.5. The fracture toughness measured for soda lime glass is in agreement with the literature values for the three tested scales. In contrast, K_c for the alumina ceramic tends to converge toward the literature value as the probing scale is reduced. The lower values obtained with the 200 and 50 μm probes may be due to microsctructural defects (e.g., pores), whose influence was avoided by probing the bulk between the pores with the 20 μm probe.

Overall, consistent results were obtained between fused silica and soda lime glass in the spherical range of the 200, 50 and 20 μm probes. Therefore, scaling of the spherical microscratching method, along with fused silica calibration, is adequate for materials in which homogeneity is maintained over the probed scales. In addition, results for Macor and alumina stress the importance of the microtexture, which may be responsible for differences in fracture toughness over the probed scales.

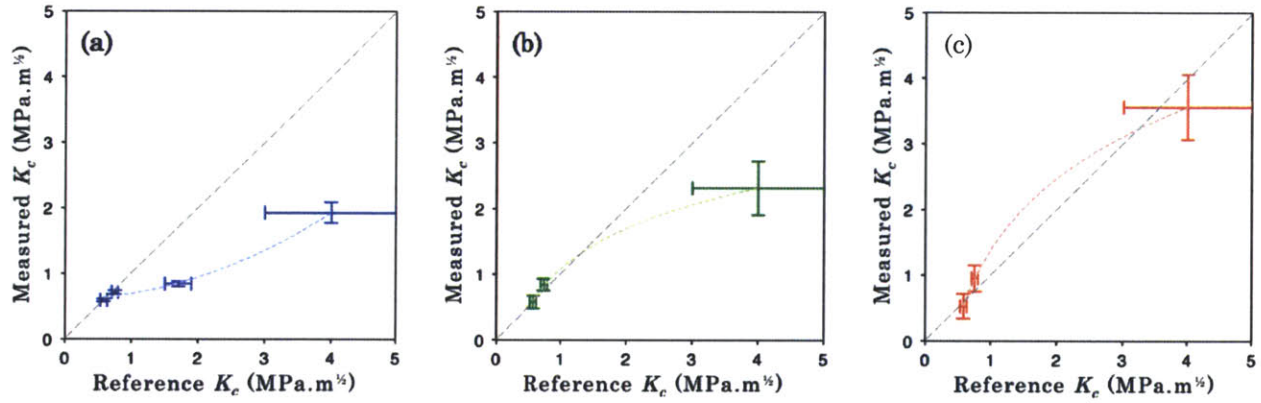

Fig. 6.22. Fracture toughness of ceramics measured in the spherical range, with probes of radius (a) 200 μm, (b) 50 μm, and (c) 50 μm, as a function of the reference values from literature. The vertical error bars present the standard deviation on the measurements, and the horizontal error bars show the range of the published values (see Table 6.1).

Material	Spherical 50 μm			Spherical 20 μm		
	Max d/R	Fitted b	K_c (MPa.m^{½})	Max d/R	Fitted b	K_c (MPa.m^{½})
Fused silica	0.045	1.17	0.58 ± 0.10	0.045	1.00	0.53 ± 0.19
Soda lime glass	0.045	1.49	0.84 ± 0.09	0.045	1.13	0.95 ± 0.20
Alumina	0.045	1.35	2.29 ± 0.40	0.040	1.47	3.56 ± 0.50

Table 6.6. Scratching results for reference ceramics (spherical range, 50 and 20 μm probes).

6.5.3 Conical Range for 50 and 20 µm Probes

The conical range of the 50 and 20 µm probes was investigated with fused silica, soda lime glass and alumina ceramic. Macor was not included in this series of tests because of the large chipping observed in the spherical range. Fig. 6.23 presents the scratch results for alumina, which do not exhibit the convergence typical of a fracture process (see section 6.1.5). Thus, downscaling of the conical range is investigated with fused silica as calibration material and soda lime glass. As presented in Table 6.7, the measured K_c of the soda lime glass is slightly overestimated with 0.98-1.09 ± 0.08 MPa.m^{½} as compared to the reference values of 0.7-0.8 MPa.m^{½}.

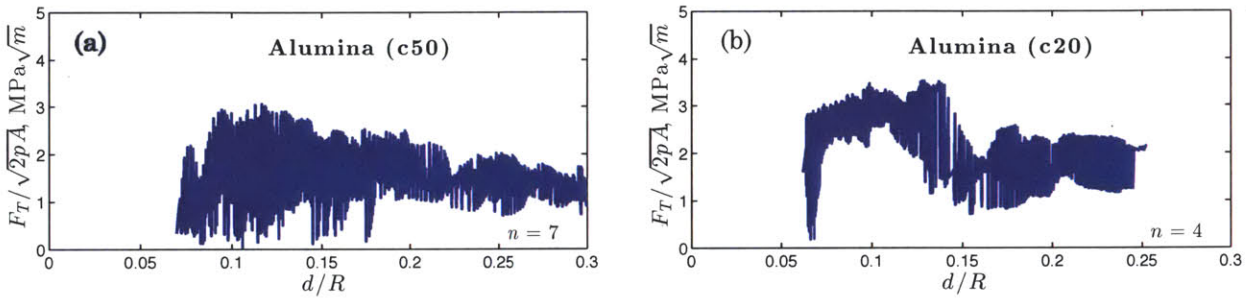

Fig. 6.23. Fracture toughness measured on alumina in the conical range of (a) the 50 µm probe, *c50*, and (b) the 20 µm probe, *c20*. The convergence typical of a fracture process is not achieved with this material at those scales.

Material	Conical 50 µm			Conical 20 µm		
	Max *d/R*	Fitted *b*	K_c (MPa.m^{½})	Max *d/R*	Fitted *b*	K_c (MPa.m^{½})
Fused silica	0.30	1.74	0.57 ± 0.06	0.45	1.99	0.57 ± 0.06
Soda lime glass	0.35	1.31	0.98 ± 0.08	0.35	1.54	1.09 ± 0.07
Alumina	0.30	1.06	n/a	0.25	0.99	n/a

Table 6.7. Measured fracture toughness for the ceramics tested in the conical range of the 50 µm and 20 µm probes.

6.6 Chapter Summary

This chapter first described the microscratch test method used in this project to predict the fracture toughness of brittle materials according to the model developed by Akono and Ulm [5,6,4]. In this method, a microscratch is performed with a Rockwell diamond probe forced over a surface under constant horizontal displacement and increasing vertical force. The fracture toughness is then extracted from the measured penetration depth and horizontal

force with a model based on the linear-elastic fracture mechanics. The model was calibrated with reference polymers and ceramics, which were presented in this chapter along with the experimental protocols. In addition, improvements of the experimental methods were proposed based on the experience gained in this project. A first suggestion was to avoid holding the sample with the circular jaws, since they were found to allow vertical movement of the sample. A better alternative would be to glue circular samples on rectangular aluminum bases and use the rectangular jaws. Another interesting observation was the sensitivity of the Lexan polymer to moisture, which needs to be controlled in order to obtain good quality calibration. In addition, downscaling of the microscratch test was investigated with probes of decreasing radius (200, 50 and 20 μm) and with reference ceramic materials. It was found that the microscratching model could be downscaled in the spherical range with good accuracy, given the homogeneity of the materials over the tested scale (e.g., fused silica and soda lime glass). Furthermore, the influence of the microtexture was emphasized with the results obtained for Macor and alumina ceramics at the different scales.

Part III

Results and Discussion

Chapter 7

Microstructure and Characteristic Scales

In order to perform investigations on heterogeneous materials like clinkers, knowledge of the characteristic length scales is required. As illustrated in Fig. 7.1, clinker is a multi-scale material consisting of nodules at the macroscale (10^{-1}, 10^{-2} m), characterized by a porous texture at the intermediate scale (10^{-3}, 10^{-4} m) and composed of different crystalline phases at the microscale (10^{-5}, 10^{-6} m). A detailed description of these characteristic scales is presented in this chapter, along with microstructure analyses of the investigated clinkers.

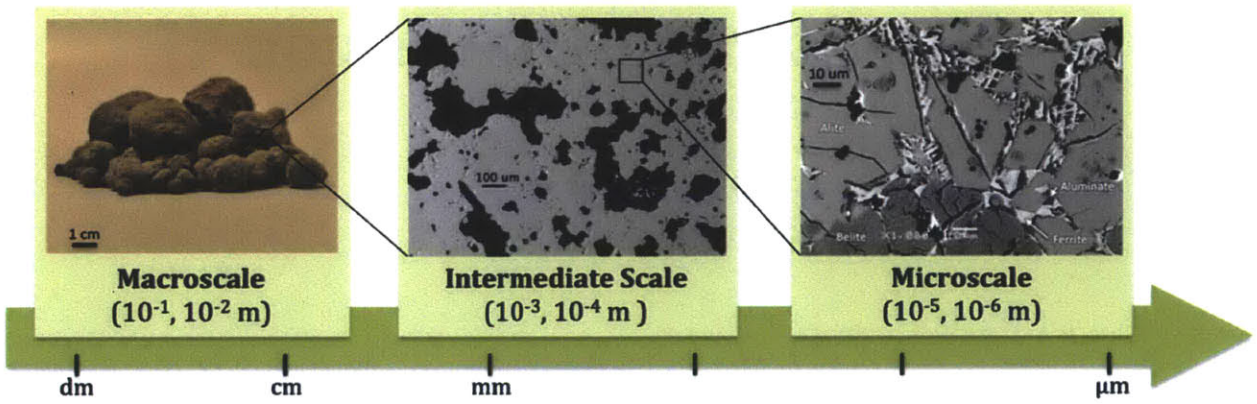

Fig. 7.1. Characteristic scales of clinkers: clinker nodules at the macroscale are characterized by a porous texture at the intermediate scale and they are composed of different crystalline phases at the microscale (alite, belite, aluminate, ferrite).

7.1 Macroscale: Nodules

Clinker nodules are produced during air quenching of the melt at the exit of the cement kiln. Their size and properties depend on firing and quenching conditions. Clinkers in this study generally exhibit a gradation in nodule size from fine micron-sized powder up to nodules of 30-40 mm in diameter, with the exception of clinker C4 which contains nodules up to 150 mm in diameter. For each clinker type, representative sub-samples of nodules with diameters of 20-30 mm were extracted to perform bulk analyses, as illustrated in Fig.

7.2. It is worth noting that nodules of clinker C2 are very fragile compared to those of other clinkers. Special care is required during handling and cutting prior to epoxy impregnation, as nodules would otherwise split or disintegrate.

Fig. 7.2. Typical clinker nodules of 20-30 mm diameter selected for bulk analyses, examples of clinkers (a) C2, (b) C3 and (c) C4.

7.2 Intermediate Scale: Porosity and Bulk Surfaces

At the intermediate scale, clinkers are generally very porous materials with available bulk surfaces limited by porosity. As illustrated in Fig. 7.3, total porosity and pore size distribution may vary significantly between different clinker types. As fracture properties at the macroscale are likely to be influenced by porosity at the intermediate scale, apparent size distribution of the pores is determined with image analysis for the studied clinkers.

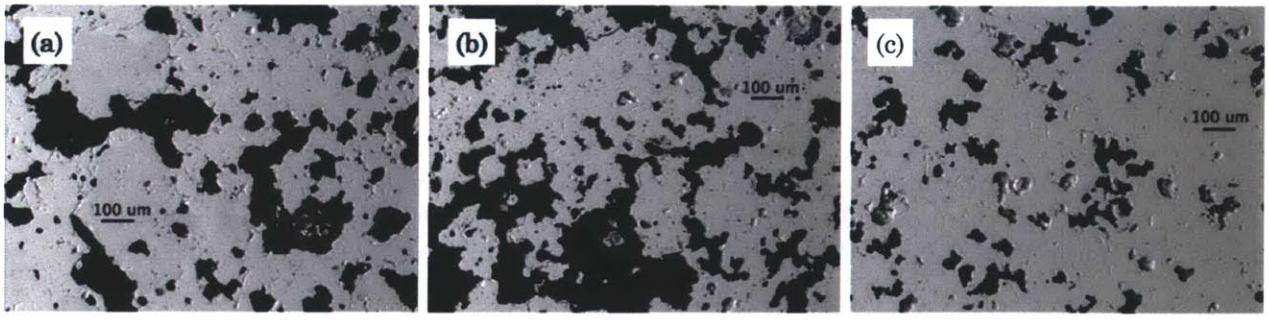

Fig. 7.3. Typical intermediate scale imaging of clinkers (a) C2, (b) C3 and (c) C4. The SEM micrographs are optimized for image analysis of porosity: gray clinker matrix contrasts strongly with black porous regions.

Porosity is investigated with low magnification back-scattered SEM images (e.g., Fig. 7.3). The pore areas are extracted with the image analysis software ImageJ [106] after manual thresholding. To obtain representative porosity measurements, 16 images of 1 mm by

1.3 mm are analyzed for every clinker. The number of images is chosen to analyze a surface much larger than the largest heterogeneities (i.e., largest pores). As presented in Fig. 7.4a, the total porosity is significantly lower for clinker C4 with 12%, and higher for clinker C3 with 33%, in comparison to the other two clinkers (~25%). According to the Delesse principle [84], these surface porosities may be considered representative of the volumetric porosities. Based on Ono's work [91], the porosity for ordinary clinker should be between 13 and 16%, in contrast to poorly burned clinkers for which porosity can reach 25 to 35%. Thus, the porosity of the studied clinkers is above the average, except for clinker C4.

Apparent size distributions presented in Fig. 7.4b indicate that average equivalent pore diameters are consistent with total porosity: 65 μm for clinker C4, 250 μm for clinker C2, and 150 μm for clinkers C1 and C3. Because of the interconnections between pores, these values are overestimations compared to the measurable dimensions of single pores. The equivalent pore diameters are calculated assuming circular pores, and the analysis method thus considers connected pores as a single pore with larger radius.

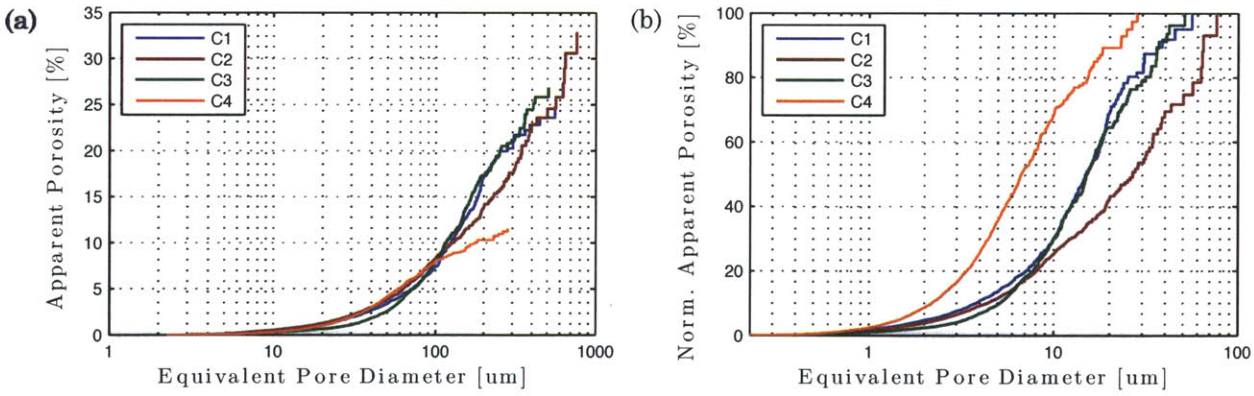

Fig. 7.4. Results of clinker surface image analyses showing, (a) apparent pore size distributions and (b) normalized apparent pore size distributions. Porosity of 33% is measured for clinker C2, 12% for clinker C4 and ~25% for clinkers C1 and C3.

In addition to porosity, surfaces available between pores are of interest for microscratching of the bulk at the intermediate scale. Surfaces without any pores being very scarce, bulk surfaces adequate for intermediate scale testing are defined as surfaces exempt of pores larger than 5-10 μm. Although total porosity varies between the studied clinkers, the distribution of pores smaller than 100 μm tends to be random and of similar magnitude for all clinkers, as illustrated in Fig. 7.4a. Thus, similarly sized surfaces may be expected for

testing on the different clinkers. Observation of several clinker surfaces (e.g., Fig. 7.5) showed that intermediate scale microscratching of the bulk should be limited to surfaces of 200 x 200 μm^2, as larger surfaces are not available in sufficient quantities.

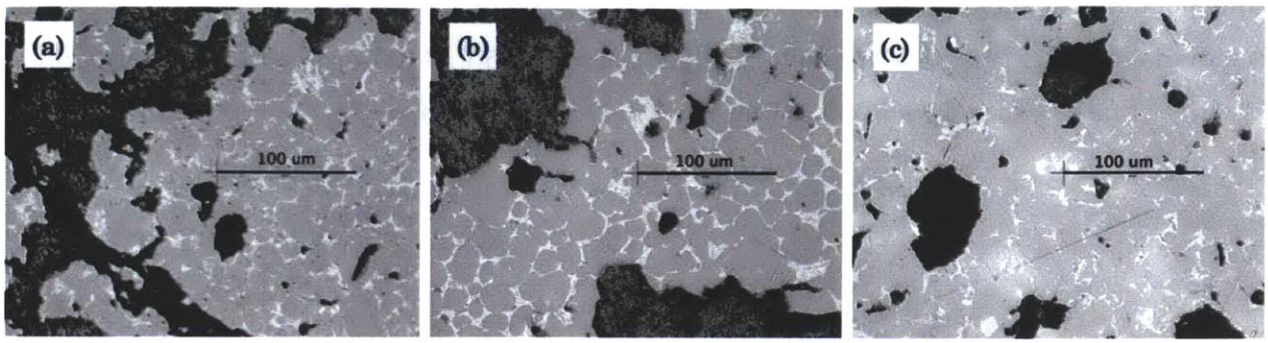

Fig. 7.5. Examples of available bulk surfaces for samples (a) C2, (b) C3 and (c) C4. Bulk surfaces adequate for intermediate scale testing (exempt of pores larger than 5-10 μm) are limited to 200 x 200 μm^2, as larger areas are not available.

If microscratching benefits from large bulk surfaces, chemistry analyses require clinker representativeness on relatively small surfaces, which is only possible with the use of epoxy embedded powdered samples. As illustrated in Fig. 7.6a, the polished surfaces of this type of samples are composed of packed particles. To characterize these surfaces, apparent particle size distributions are measured with image analyses (particles are assumed to be circular, mean distributions are based on the analysis of 6 independent images).

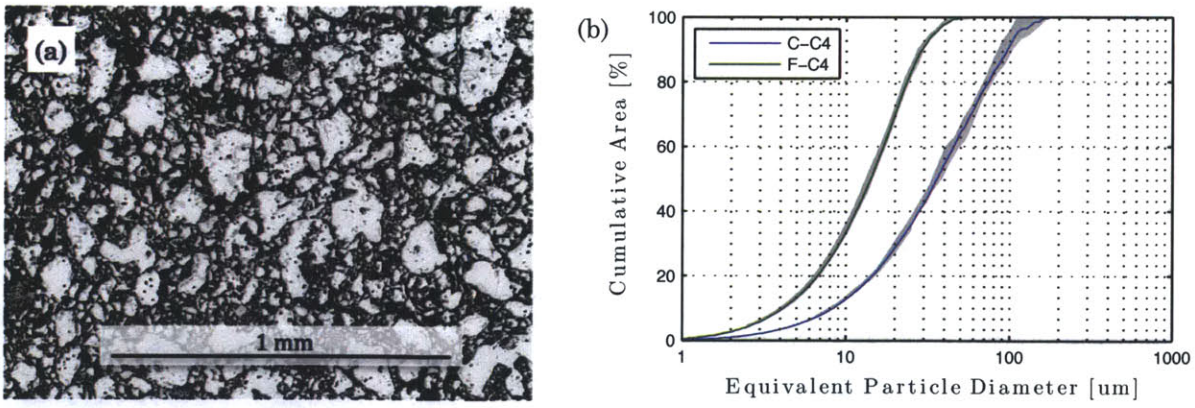

Fig. 7.6. (a) Typical SEM micrograph of coarsely ground sample *C-C4* (1280x960 pixels, 1μm/pixel) and (b) apparent particle size distributions for both coarsely ground and finely ground samples of clinker *C4*. The average is presented along with bounds based on the analysis of 6 independent images.

As illustrated with clinker C4 in Fig. 7.6b, the difference in particle diameters between the coarsely ground and the finely ground samples is significantly higher than the variability in the measurement (shown by the bounds for each curve based on the analysis of 6 independent images). Fig. 7.7 shows the distributions for all the clinker samples. The median equivalent particle diameter ranges between 35 and 45 μm for the coarsely ground samples and between 15 and 20 μm for the finely ground samples.

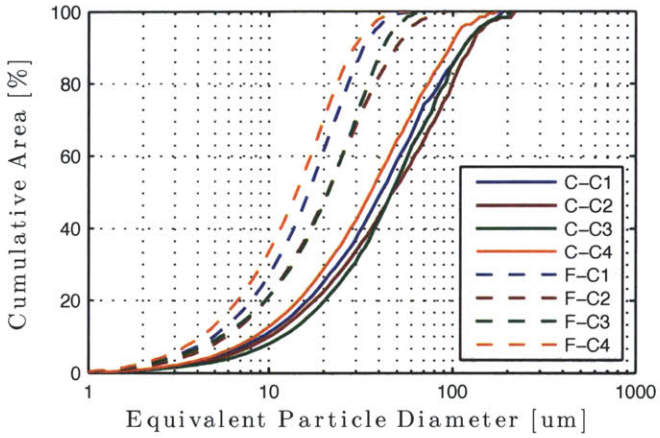

Fig. 7.7. Comparison of coarsely ground and finely ground samples with respect to their apparent particle size distribution, for the four studied clinkers.

Fig. 7.8 presents additional SEM imaging of the powdered samples performed at higher magnifications to identify the surface characteristics.

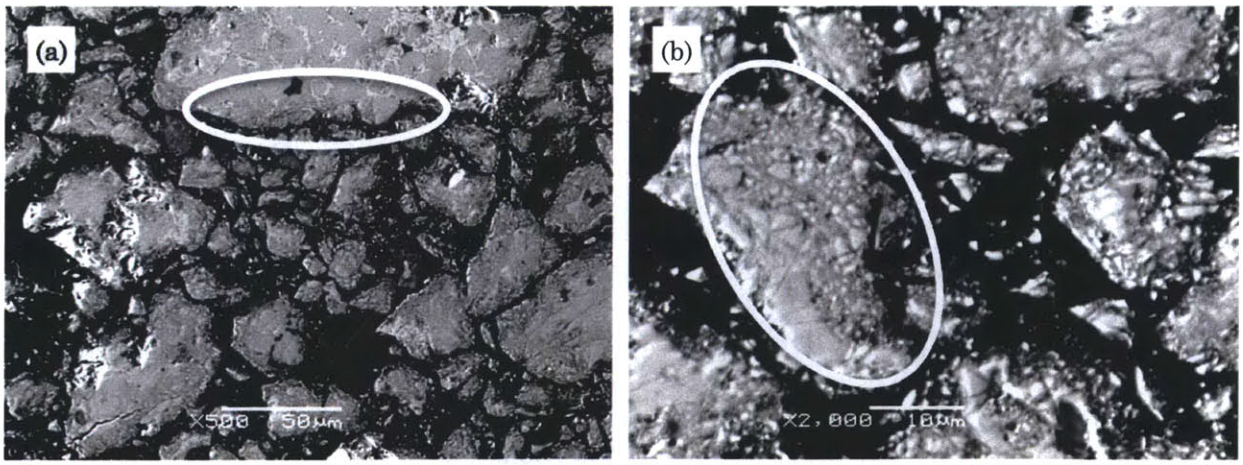

Fig. 7.8. SEM micrographs of coarsely ground sample *C-C4*. (a) The 500X magnification illustrates the defects introduced by grinding on the boundaries of large particles, whereas (b) the 2000X magnification illustrates the pronounced microcracking of smaller particles.

As illustrated with clinker C4 in Fig. 7.8a, the coarsely ground samples are composed of a large range of particle sizes. Larger particles, in which the main clinker phases are distinguishable, coexist with smaller particles, i.e., fragments of single crystals. However, the grinding necessary to prepare the powdered samples introduces defects and micro-cracking of the particles. This is usually observed near the exterior boundaries for large particles (e.g., Fig. 7.8a) and sometimes over the whole surface for smaller particles (e.g., Fig. 7.8b).

7.3 Microscale: Crystalline Phases

At the microscale, clinkers are composed of four main crystalline phases: alite, belite, aluminate and ferrite. Each phase has characteristic crystal shapes and sizes, which are dependent on manufacturing conditions. Alite crystals exhibit angular edges with normal crystal size of 25-65 μm [22]. In addition, the crystals are often micro-cracked as a result of the volume shrinkage occurring during the crystallization of the interstitial phases [74]. The studied clinkers generally follow these trends (e.g., Fig. 7.9b), with the exceptions that micro-cracking was not observed in clinker C4 (see Fig. 7.9d), and that crystals with larger diameters were found in clinker C2 (~100 μm) and clinker C3 (>150 μm). In addition, clinker C4 contains smaller alite crystals (10-20 μm) and a greater separation between adjacent crystals. Interstitial material surrounds almost all perimeters of crystals (e.g., Fig. 7.9d), whereas cannibalistic alites (i.e., adjacent alites crystals fused together) are observed for the other clinkers (e.g., Fig. 7.9bc).

Belite crystals are normally rounded (e.g., Fig. 7.9c), with a multi-directional lamellar structure (e.g., Fig. 7.9d). They are usually slightly smaller than alite crystals, with sizes of 20-40 μm [22]. The studied clinkers contain belite crystals of typical sizes that are usually found in clusters (e.g., Fig. 7.9c), except for clinker C4 in which silicates are well distributed (e.g., Fig. 7.9d). In addition, clinker C1 exhibits closely packed ragged belite crystals with extension of "fingers" into the matrix (e.g., Fig. 7.9a). If the majority of belite content is concentrated in well-defined belite crystals, belite inclusions are also present into alite crystals for all clinkers (e.g., Fig. 7.9c).

Observation of the interstitial phase indicates a concentration of ferrite between crystals in belite nests, as illustrated in Fig. 7.9a-c. The spacing between alite crystals is usually filled

with lath-form crystals of ferrite intermixed with the aluminate phase [22], as shown in Fig. 7.9b-d. The size of these intermixed crystals is generally of a few microns (2-3 μm), with rare occurrence of larger single-phase regions (e.g., Fig. 7.9b).

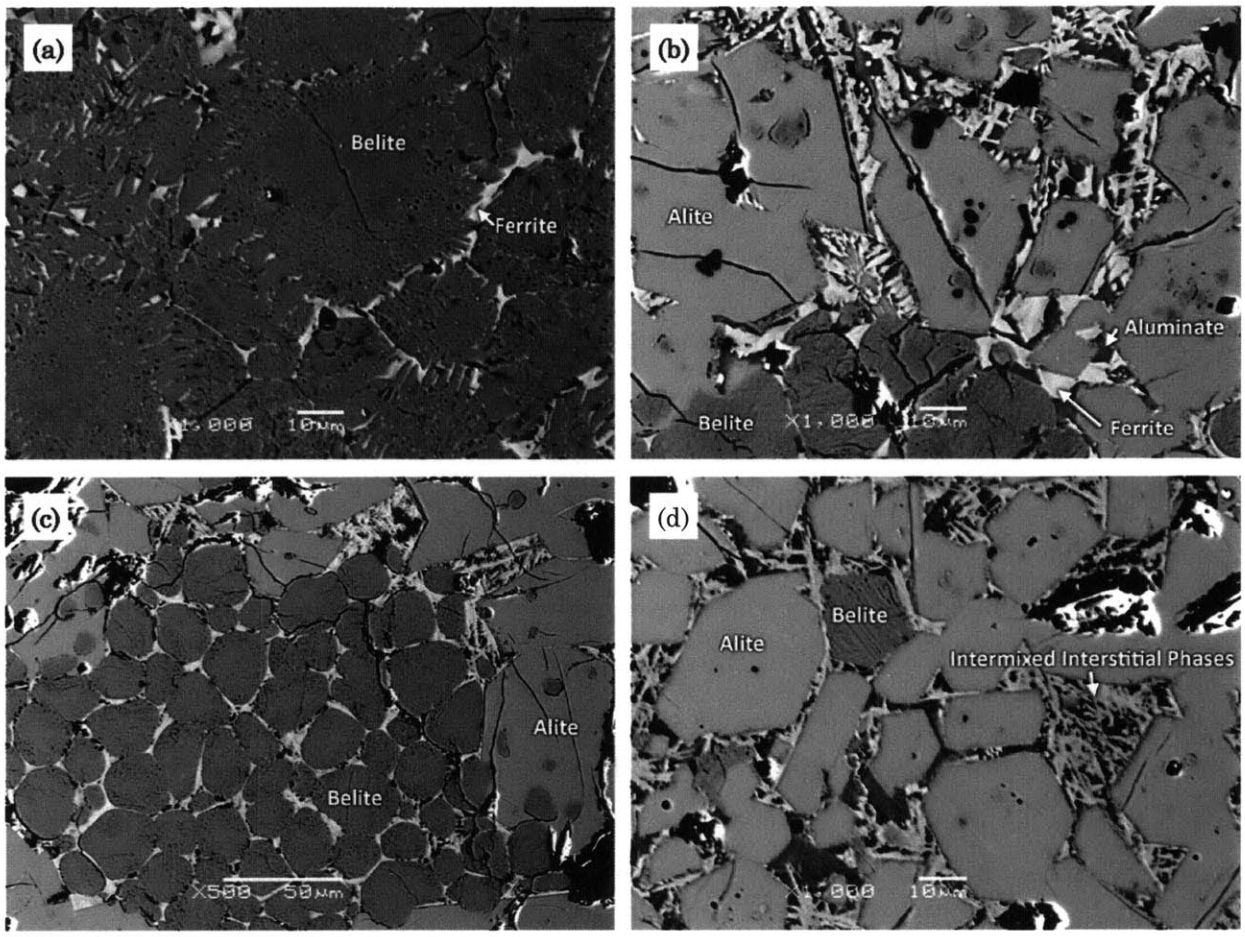

Fig. 7.9. SEM imaging of phases details for the fours studied clinkers: (a) C1 showing dendritic belite; (b) C2 showing the four clinker phases and micro-cracked alites; (c) C3 illustrating belite nesting and inclusion of belites into alite crystals; and (d) C4 showing distributed belites and alites crystals free of micro-cracking.

Thus, investigations of alite and belite phases at the microscale are limited by crystal sizes of approximately 20-30 μm. In addition, the characteristic size of the interstitial phases (2-3 μm) should be considered during analyses aiming to probe all the clinker phases.

7.4 Chapter Summary

In this chapter, the microstructure of the studied clinkers was investigated with respect to the characteristic clinkers scales. At the macroscale (10^{-1}, 10^{-2} m), clinkers are nodules

graded from dust up to diameters of 30-40 mm (and up to 150 mm for clinker C4). The intermediate scale (10^{-3}, 10^{-4} m) is characterized by a combination of porosity and clinker matrix. Image analysis applied to SEM micrographs was used to quantify porosity. Clinker C2 showed highest porosity with 33%, compared to 12% for clinker C4, and around 25% for clinkers C1 and C3. Bulk surfaces between the pores were also investigated and it was found that bulk testing should be limited to surfaces of 200 x 200 μm^2, as larger surfaces were very scarce. At the microscale (10^{-5}, 10^{-6} m), clinkers are composed of the four main clinker phases (alite, belite, aluminate and ferrite). Microcracking and fusion of adjacent alite crystals was observed for all clinkers except C4. In addition, clinker C3 contained oversized alite crystals larger than 150 μm, in comparison to the usual 25-65 μm. Typical sizes (20-40 μm) of belite crystals were observed and these crystals were usually found in clusters, except in clinker C4. Interstitial phases (aluminate and ferrite) filled the space between alites and belites and were generally composed of intermixed crystals of a few microns (2-3 μm), with rare occurrence of larger single-phase regions. Finally, the description of clinker characteristic scales performed in this chapter, along with the identification of particularities of the studied clinkers, will be used in further chapters to design experiments and to support the interpretation of the results.

Chapter 8

Mineralogy and Bulk Chemistry

Mineralogy and chemistry of clinkers are of great importance, since they have influence on both the grindability and the reactivity of clinkers. This chapter investigates the studied clinkers with the characterization methods used by industry: X-ray diffraction (XRD) with qualitative phase identification and quantitative Rietveld analyses, as well as X-ray fluorescence spectroscopy (XRF). In addition, the external standard method is applied with the XRD measurements to assess the non-crystalline content.

8.1 Qualitative Mineralogy and Polymorphism (XRD)

XRD spectra measured for the four clinker samples are presented in Fig. 8.1 together with phase identification. Monoclinic alite, *A*, orthorhombic belite, *B*, orthorhombic aluminate, *C'*, and orthorhombic ferrite, *F*, patterns are fitted to the XRD spectra. The identified peaks are in good agreement with Taylor's XRD patterns of typical Portland cement [121].

In addition to the above principal clinker phases, two other secondary phases are identified: free lime, *L* (CaO/cubic) and periclase, *P* (MgO/cubic). Peak intensities for these phases are relatively small and vary with clinker type, probably as a consequence of the raw mix composition and burning conditions of each clinker. Calcium oxide may persist as free lime in clinker if the lime saturation factor is above one (see section 4.3.2). Also, magnesium oxide may be introduced in clinker raw mixes as an impurity to reduce melting temperature and to stabilize reactive polymorphs at room temperature. After substitution in clinker phases, additional magnesium in Portland cement clinker tends to crystallize as periclase [121].

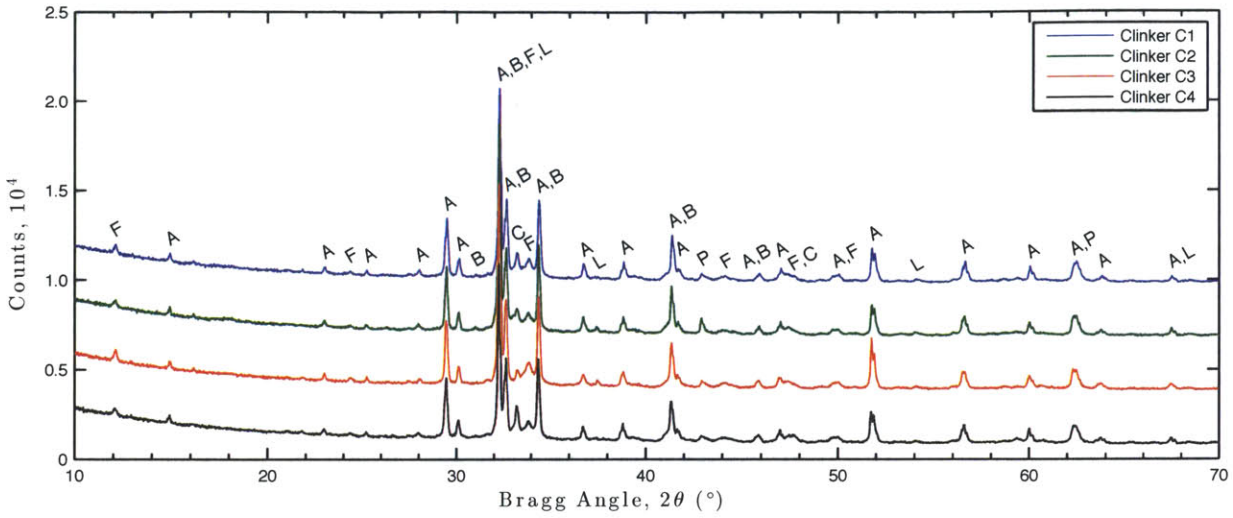

Fig. 8.1. Qualitative phase identification for the X-ray diffraction patterns of the four studied clinkers. The major phases identified are alite, *A*, belite, *B*, aluminate, *C*, ferrite, *F*, with minor (/trace) amounts of free lime, *L*, and periclase, *P*.

Alite polymorphism is determined by closer observation of the XRD spectra intensities between 51 and 52.5 °2θ, as shown in Fig. 8.2a. According to Taylor [121], two peaks of similar intensities correspond to the monoclinic polymorph M_3, whereas higher intensity of the first peak indicates the presence of the monoclinic polymorph M_1, as illustrated in Fig. 8.2b.

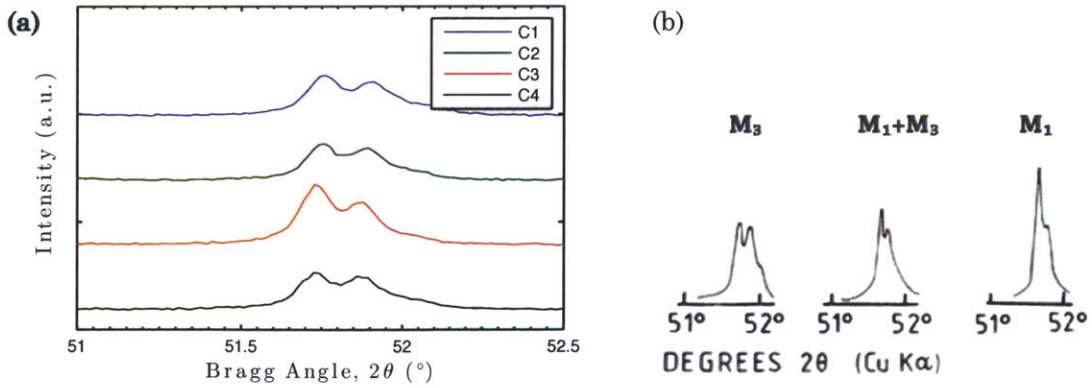

Fig. 8.2. (a) Specific window of the XRD patterns which presents characteristic peaks for alite polymorphism identification. (b) Reference spectra for alite polymorphism as presented by Taylor [121]. The relative height of the peaks around 52 °2θ indicates the presence of polymorph M_3, polymorph M_1 or a combination of both polymorphs.

Alite polymorphism is related to the supersaturation of the melt. High supersaturation, induced by sufficient amounts of MgO and/or high firing temperature, results in high intensity of nucleation leading to the stabilization of the polymorph M_3, as described by Maki *et al.* [76,75]. On the contrary, low supersaturation of the melt and lower viscosity, triggered by the presence of SO_3, results in lower intensity of nucleation leading to unstable growth of larger crystals of the polymorph M_1 [76,75]. Stanek [115] found that this polymorphism had influence on the strength of cements. He measured strengths 10% higher with the polymorph M_1 compared to the polymorph M_3. Clinkers studied in this project generally exhibits the alite polymorph M_3 except for clinker C3 whose alite crystals seem to be a combination of both polymorphs M_3 and M_1. These results are in agreement with previous observations of the microstructure in section 7.3 where larger alite crystals typical of the polymorph M_1 were observed in clinker C3.

8.2 Quantitative Mineralogy (Rietveld Analyses)

As illustrated in Fig. 8.3 for a single scan performed on clinker *C2*, the Rietveld method is used to fit the experimental profile with a calculated profile. The quality of the fit is validated both by visual inspection and with the weighted residual parameter, R_{wp}. For this scan, $R_{wp} = 6.15\%$ which satisfies the quality criterion fixed in this work to $R_{wp} < 10\%$ (see section 4.2.3). Similar quality of refinement is achieved for all scans with $R_{wp} < 8\%$, as shown in Table 8.1.

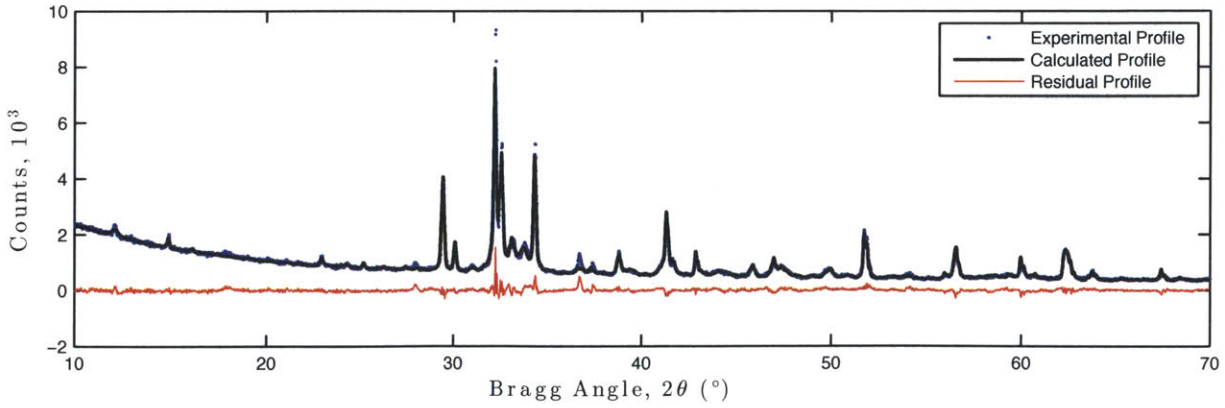

Fig. 8.3. Comparison of the experimental profile, the calculated profile and their difference (the residual profile) for a typical Rietveld refinement of clinker *C2*. The quality of the fit is assessed both qualitatively by visual inspection (peaks are adequately modeled and highest residuals are associated with highest intensities) and quantitatively with the weighted residual profile: $R_{wp} = 6.15\% < 10\%$.

As presented in Table 8.1, the refined weight percent show good repeatability with variations lower than 2 wt%. The results indicate higher belite and periclase contents for clinker *C2*, higher alumina to ferrite ratio for clinker *C4*, highest alite content for clinker *C3*, and average weight fractions for clinker *C1*. The measured free lime content is found to be negligible.

Clinker	**C1**	**C2**	**C3**	**C4**
	$\bar{x} \pm$ *95% CI*	$\bar{x} \pm$ *95% CI*	$\bar{x} \pm$ *95% CI*	$\bar{x} \pm$ *95% CI*
Weight fractions (wt%) for all the crystal structures				
Alite - M_3	50 ± 13	34 ± 11	24.6 ± 7.6	45.3 ± 4.8
Alite - M_1	16 ± 13	24 ± 13	45.9 ± 6.8	19.0 ± 4.7
Belite - β	11.9 ± 1.1	15.0 ± 0.9	10.5 ± 0.8	12.0 ± 0.4
Belite - α'	1.7 ± 1.3	5.0 ± 1.0	0.3 ± 0.5	1.0 ± 0.4
Alum. - Cubic	3.7 ± 0.2	2.2 ± 0.4	2.3 ± 0.2	8.0 ± 0.8
Alum. - Ortho.	2.0 ± 0.5	3.1 ± 1.1	0.0 ± 0.0	1.6 ± 1.0
Ferrite	13.0 ± 1.1	13.2 ± 0.5	15.0 ± 0.6	11.6 ± 0.8
Lime	0.0 ± 0.0	0.3 ± 0.5	0.0 ± 0.0	0.0 ± 0.0
Periclase	1.9 ± 0.3	3.6 ± 0.1	1.5 ± 0.2	1.3 ± 0.1
Quantitative evaluation of refinements				
R_{wp}	*7.3 ± 1.6*	*6.6 ± 0.9*	*7.1 ± 0.2*	*6.3 ± 0.6*
Weight fractions (wt%) for the identified clinker phases				
Alite	65.9 ± 0.8	57.6 ± 1.9	70.4 ± 0.9	64.4 ± 1.0
Belite	13.6 ± 0.4	20.1 ± 1.1	10.8 ± 1.2	13.0 ± 0.5
Aluminate	5.6 ± 0.5	5.3 ± 0.8	2.3 ± 0.2	9.7 ± 0.6
Ferrite	13.0 ± 1.1	13.2 ± 0.5	15.0 ± 0.6	11.6 ± 0.8
Periclase	1.9 ± 0.3	3.6 ± 0.1	1.5 ± 0.2	1.3 ± 0.1

Table 8.1. Results of the quantitative Rietveld refinements for the four studied clinkers. Weight fractions are first presented for all crystal structures included in the refinement, and then only for the identified clinker phases. The quantitative evaluation of the refinement is also presented with the weighted residual profile R_{wp}. Four replicates on two different samples are performed for each clinker. The mean value is presented along with 95% confidence interval.

In addition to weight fractions, Rietveld results give an indication on the relative distribution of polymorphs for alite, belite and aluminate. However, error on alite polymorphism is very high, and the distribution of these polymorphs should not be considered quantitatively because of strong overlapping of the characteristic peaks, as suggested by other authors [103]. Nevertheless, trends for alite polymorphs are in agreement with qualitative observations, since clinker C3 shows a stronger contribution of polymorph M_1. Observation of belite polymorphism illustrates the predominance of β belite, and clinker C2 exhibits the largest contribution of the polymorph α'.

8.3 Assessment of Non-Quantified Content (Ext. Standard Method)

In the quantitative Rietveld analyses, the measured weight fractions are normalized to the total amount of crystalline phases. To have a better description of the composition of the studied clinkers, non-quantified content was investigated with the external standard method. As shown in Table 8.2, average non-quantified contents range between 13% and 18%, with confidence intervals (95%) obtained from combinations of four scans for each clinker and three scans for the standard. In addition, lower and upper bounds are presented to reflect the disagreement in literature regarding the crystalline content of the NIST α-alumina corundum used as standard in this study. Overall, the results are in good agreement with literature. Non-quantified/amorphous contents for clinkers usually range between 3.3% and 25% [72,116,133,82,68,60,65]. Although the non-quantified content is often considered to be only amorphous material, it is defined here as the sum of the amorphous content, the non-detected crystalline phases and the residuals from fitting, as suggested by Jansen *et al.* [60].

Non-quantified content (wt%)	**Lower Bound** $\bar{x} \pm$ *95% CI*	**Average** $\bar{x} \pm$ *95% CI*	**Upper Bound** $\bar{x} \pm$ *95% CI*
Clinker C1	13 ±2	16 ±2	19 ±2
Clinker C2	12 ±2	15 ±2	18 ±2
Clinker C3	10 ±1	13 ±1	16 ±1
Clinker C4	15 ±2	18 ±2	21 ±2

Table 8.2. Non-quantified content determined for the four studied clinkers. Disagreement in literature about exact crystalline content of the NIST α-alumina corundum is responsible for lower and upper bounds. Confidence intervals, *CI*, of 95% are obtained with combinations of four scans for the clinkers and three scans for the standard.

The combination of the quantitative Rielveld results with the non-quantified contents is presented in Fig. 8.4. The non-quantified contents represent a significant proportion of the studied clinkers, with weight fractions of the same magnitude as major clinker phases such as belite and ferrite. Thus, this fraction of clinkers should be considered with respect to grinding and reactivity. In this study, the non-quantified contents are of the same magnitude for all studied clinkers and the only statistically significant difference is the higher weight fraction for clinker C4 (18%), when compared to clinker C3 (13%).

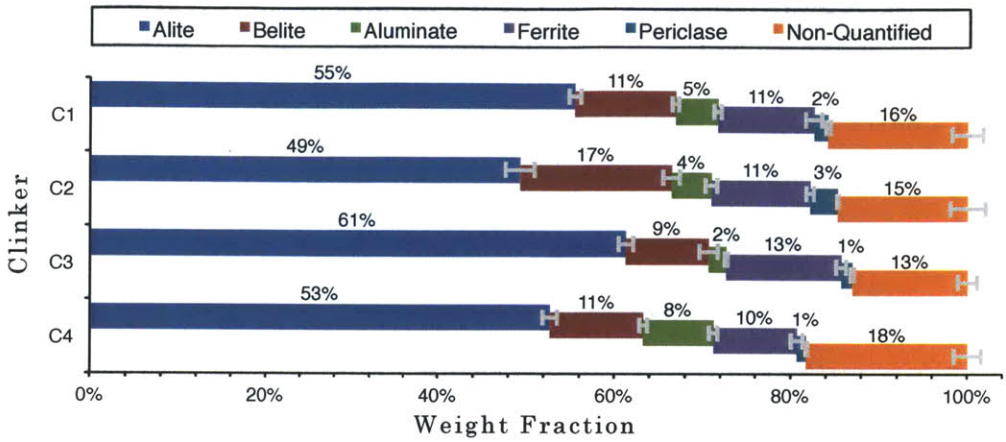

Fig. 8.4. Combined results of the quantitative Rietveld analyses and the assessment of non-quantified content performed with the external standard method. The error bars represent 95% confidence intervals based on 4 repetitions.

8.4 Bulk Chemistry (XRF) and Composition Parameters

Bulk oxide compositions measured by X-ray fluorescence spectroscopy are presented in Table 8.3 for the studied clinkers. To facilitate the interpretation of these results, the composition parameters are calculated (see section 4.3.2) and presented in Table 8.4.

The results for the lime saturation factor *LSF* are in good agreement with literature values, which range between 0.92 and 0.98 [121]. Clinker C3 has a higher but acceptable LSF value, as modern clinkers may reach up to 1.02 [121]. Higher LSF values implies increased availability of CaO which favor the alite phase and may result in residual free lime precipitation. These results are in agreement with quantitative mineralogy (section 8.2) where clinker C3 exhibits higher alite content than the other clinkers.

Furthermore, the modified *LSF**, which accounts for possible Mg substitution in alite, is higher than 100 for all clinker. This indicates that in the case of perfectly homogeneous raw mix with ideal burning conditions, all the belite would be transformed into alite and there would be precipitation of both residual CaO and MgO. Observation of the mineralogy results (section 8.2) illustrates that these ideal conditions cannot be met in industrial cement kilns. Local variations in temperatures and in concentrations of CaO and MgO prevent complete transformation of belite into alite. Nevertheless, precipitation of the periclase phase is observed for all clinkers and specifically for clinker C2, which is in agreement with the higher MgO content measured with XRF for this clinker. In contrast, the free lime phase is

not identified with the XRD analyses, which does not mean it is absent in all samples. Free lime is known to be a soft clinker phase (Mohs' hardness of 3-4 compared to 4-6 for the other major clinker phases [22]) and sample preparation may result in overgrinding of lime which then prevents its experimental identification.

Oxides ***(wt%)***	***C1***	***C2***	***C3***	***C4***
CaO	65.54	64.22	64.58	64.08
SiO_2	20.57	20.72	19.59	20.20
Al_2O_3	5.04	4.86	4.73	6.29
Fe_2O_3	3.02	3.11	3.63	2.85
MgO	2.92	4.34	2.53	2.56
SO_3	0.49	0.47	1.56	1.19
Na_2O	0.25	0.25	0.26	0.30
K_2O	0.54	0.71	0.91	1.07
TiO_2	0.22	0.22	0.22	0.24
P_2O_5	0.12	0.09	0.18	0.28
Mn_2O_3	0.17	0.08	0.10	0.08
SrO	0.10	0.09	0.23	0.29
LOI	0.96	0.82	1.46	0.52
Na_2O_{eq}	0.61	0.72	0.86	1.00

Table 8.3. Bulk chemistry weight fractions measured by XRF and loss on ignition, *LOI*, for the four studied clinker samples (i.e., C1, C2, C3 and C4). Equivalent alkalis are calculated according to ASTM C150-04 [10]: $Na_2O_{eq} = Na_2O + 0.658K_2O$.

Parameter	***C1***	***C2***	***C3***	***C4***
LSF	0.98	0.96	1.01	0.96
LSF*	1.05	1.06	1.07	1.02
SR	2.55	2.60	2.35	2.21
AF	1.67	1.56	1.30	2.20

Table 8.4. Composition parameters calculated for the four studied clinkers. The composition parameters include the lime saturation factor *LSF*, the modified *LSF** which allow for Mg substitution in alite, the silica ratio *SR* and the alumina ratio *AR*.

In addition, the calculated alumina ratios, *AF*, are also in good agreement with the mineralogy results: the aluminate phase is present in lower concentration for clinker C3 and in higher concentration for clinker C4. These results for clinker C4 also correlate with previous observations of the microstructure (section 7.3). An intermix of aluminate and ferrite is observed between the well-separated silicate crystals of clinker C4, whereas the other clinkers contain clusters of belite crystals usually filled with the ferrite phase.

In addition to the composition parameters, the bulk chemistry may be used to support the assessment of polymorphism of the alite phase (section 8.1). In this study, clinker C3 contains the alite polymorph M_1 and the highest SO_3 content, both of which are associated with slow alite grow rates [76,75]. Finally, the oxide composition of clinkers may be used to validate the conformity with the requirements of standards such as ASTM 150 [10]. An example is the equivalent alkalis content which must be kept below 0.6% for low-alkali cements (only clinker C1 meets this requirement).

8.5 Chapter Summary

In this chapter, the mineralogy of the clinkers was assessed with XRD analyses focused on the alite polymorphism and the abundance of constituting phases (including both crystalline phases and non-quantified content). In addition, bulk chemistry was investigated with XRF and the composition parameters were calculated. Based on these measurements, particularities were identified for each clinker. Clinker C1 showed low alkali content, and it is therefore the only clinker usable in low alkali cements. Clinker C2 had the highest belite content, with 20% of the crystalline phases. Its MgO content was also significantly higher than for other clinkers, as measured both with XRD and XRF. Clinker C3 was the only clinker containing significant amount of the alite polymorph M_1, as determined in the XRD analyses. This observation was also supported by the high SO_3 concentration measured with XRF and the oversized alite crystals (>150 μm) previously observed in the SEM analyses. In addition, clinker C3 had the highest alite content and the lowest aluminate content, which is in agreement with its high lime saturation factor *LSF* and low alumina ratio *AR*. Clinker C4 was characterized by the highest content of interstitial phases and a relatively high amount of aluminate phase, as measured by quantitative XRD. In addition, the non-quantified content of clinker C4 was higher (18%) than that of clinker C3 (13%), whereas the other two clinkers contained average quantities. Finally, the comprehensive characterization presented in this chapter will be use for further comparison with the alternative statistical EPMA analysis method presented in Chapter 9 and for correlation with the mechanical properties investigated in Chapter 10.

Chapter 9

Alternative Comprehensive Characterization

Recent experimental and simulation works proposed new possibilities for engineering clinkers with lower grinding energy and higher reactivity, based on chemical substitutions in the clinker main phases [70,77]. This led to an increased interest in monitoring the phases' chemistry, which may be quantitatively measured either with an electron-probe microanalyzer (EPMA) equipped with wavelength dispersive spectrometers [67,104] or with an SEM equipped with an energy dispersive spectrometer (SEM-EDS) [28].

This chapter proposes an alternative characterization method to provide, from a single EPMA experiment, simultaneously the chemistry of individual phases, their relative abundance and the chemistry of the bulk material. The method consists of performing a grid of EPMA spot analyses over a representative sample surface and using advanced statistical tools to extract the desired quantities. This method is applied to the four industrial clinkers of this study with three different variants in sample preparation: bulk samples, coarsely ground samples and finely ground samples. The accuracy of the method is assessed by comparison with results from the previous chapter.

9.1 Data Sieving

The first step of analysis consists of sieving the data to isolate the "signal" from the "noise", using Gaussian mixture clustering of the analytical totals (see section 5.3.1). As presented in Table 9.1, the bounds on analytical totals are determined for each dataset, along with the sieving ratio of N valid "signal" points over N_0 raw points.

The bounds for bulk samples are in excellent agreement with the expected values of 100 ± 2 [45], which indicates a good calibration of the instrument and the quality of the probed surface. On the other hand, lower totals are measured for powdered samples. This

systematic error may be attributed to particles defects and microcracking imposed during grinding, as shown in Fig. 7.8.

Clinker	Bounds for Totals of Signal (wt %)					Sieving Ratio, N/N_0 (%)				
	Bulk	Coarse		Fine		Bulk	Coarse		Fine	
		Grid a	*Grid b*	*Grid a*	*Grid b*		*Grid a*	*Grid b*	*Grid a*	*Grid b*
C1	[97,103]	[87,97]	[86,97]	[84,99]	[86,99]	63	43	47	45	38
C2	[96,104]	[93,100]	[92,100]	[88,99]	[86,100]	64	45	45	40	46
C3	[97,102]	[90,101]	[88,100]	[89,102]	[85,97]	78	52	47	39	42
C4	[96,102]	[88,98]	[87,98]	[89,98]	[89,99]	57	47	46	30	31

Table 9.1. Data sieving results for each probed grid, including the bounds for the analytical totals of the "signal" and the sieving ratio.

All these microtexture effects may significantly alter the scattering of electrons and the generation of characteristic X-rays, in comparison to polished homogeneous standard materials [9]. Such a deviation of analytical conditions tends to affect the measured intensities as well as the calculated k ratios resulting in abnormal analytical totals. As expected, finer grinding introduces more defects which amplifies this phenomenon that is generally observed for finely ground samples when compared to coarsely ground ones. Nevertheless, further analysis of the measured chemistry (see section 9.2.2) indicates that all elements seem to be affected similarly by surface irregularities, because ratios between elements are preserved. The results with lower totals may thus be considered valid. The sieving ratio is also found to decrease with increasing grinding fineness and this is further investigated in the discussion.

9.2 Chemistry of the Clinker Phases

9.2.1 Analysis of Bulk Samples

Following the sieving of "signal", each dataset is deconvoluted with respect to the main four elements (*Ca*, *Si*, *Fe* and *Al*) into statistically different clusters. Several combinations of the dimensions may be used for representation of the clustering results, but the *Ca* vs. *Si* representation is of particular interest for clinker analyses. Fig. 9.1 illustrates this representation for bulk samples *B-C2* and *B-C4*, along with the typical compositions of the main clinker phases, as published by Taylor [121].

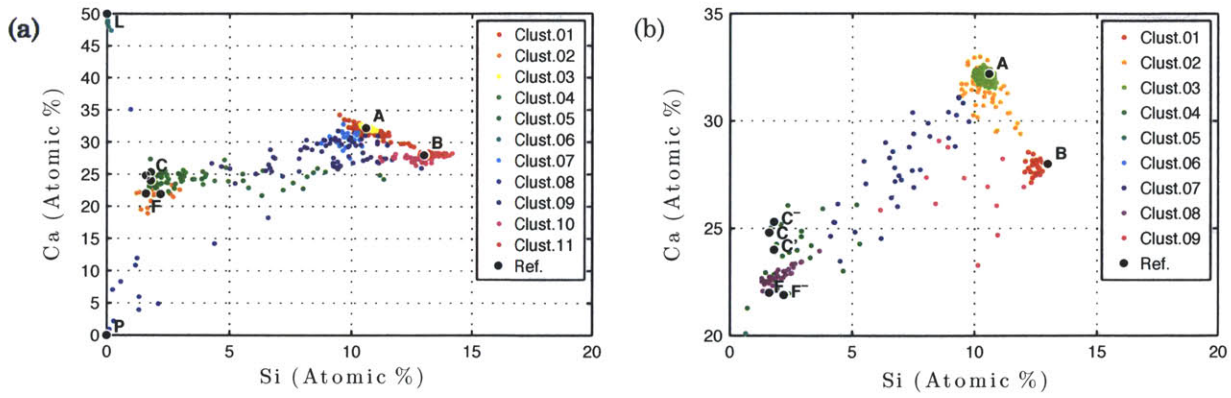

Fig. 9.1. *Ca* vs. *Si* representation for bulk samples (a) *B-C2* focused on the entire range of *Ca* values, and (b) *B-C4* focused on the main clinker phases. The deconvoluted clusters are presented along with the typical compositions of the clinker phases, as published by Taylor [121] for: alite, *A*; belite, *B*; aluminate, *C*; aluminate orthorhombic, *C'*; aluminate low-Fe, *C-*; ferrite, *F*; ferrite low-Al, *F-*; free lime, *L*; and periclase, *P*.

Each cluster is then associated either to a pure clinker phase or to a mixture of different phases. As presented in Table 9.2, four pure phases are identified: alite, *A*; belite, *B*; interstitial phase, *I*; and free lime, *L*. The remaining clusters are different mixtures, *Mix*, of the identified pure phases. In addition, a phase rich in Mg, phase *M*, is identified as a mixture of periclase (expected to be present in cement clinkers) with the other phases.

The average chemical compositions are presented in Table 9.2 for each cluster of both samples *B-C2* and *B-C4*. The measured compositions for alite and belite are found to be in good agreement with the typical compositions published by Taylor [121] and presented in Table 9.3. The major elements agree within 2-4%, and the minor elements indicate the chemical signature of each clinker type. In this first step of analysis, the two interstitial phases are not clearly distinguishable and the combined response of these two phases is explained by their microtexture. As shown in Fig. 7.9b, the elongated intermixed crystals of the two phases have relatively small lateral dimensions (~2-3 μm). As the interaction diameter of the EPMA probe is around 1.5 μm, probing of pure aluminate or pure ferrite is thus unlikely to occur.

Cluster	01	02	03	04	05	06	07	08	09	10	11
Phase	*Mix*	*I*	*A*	*I*	*Mix*	*L*	*Mix*	*M*	*Mix*	*Mix*	*B*
O	55.6	55.8	55.5	55.3	55.2	50.1	55.5	51.7	56.0	57.0	57.0
Ca	31.7	21.5	32.2	24.2	24.4	48.4	30.4	10.3	28.2	27.4	28.1
Si	10.7	1.9	10.7	2.6	6.9	0.0	9.8	1.7	9.0	12.5	13.3
Al	0.7	11.0	0.5	11.6	5.3	0.1	1.4	2.6	4.1	1.7	0.7
Fe	0.3	5.6	0.2	4.6	1.7	0.1	0.5	0.8	1.7	0.5	0.3
Mg	0.9	3.4	0.9	1.3	6.2	1.2	2.2	32.7	0.8	0.5	0.3
S	0.0	0.5	0.0	0.0	0.0	0.0	0.1	0.0	0.0	0.1	0.0
Na	0.1	0.3	0.1	0.4	0.3	0.1	0.1	0.2	0.2	0.2	0.2
K	0.1	1.3	0.1	0.4	0.4	0.1	0.3	0.2	0.3	0.6	0.4
Vol. %	15.8	2.5	37.5	9.1	2.7	1.1	4.0	1.8	10.3	4.4	10.7

Cluster	01	02	03	04	05	06	07	08	09
Phase	*B*	*Mix*	*A*	*I*	*M*	*L*	*Mix*	*I*	*Mix*
O	57.1	55.7	55.5	55.4	53.1	50.1	55.6	55.5	57.5
Ca	27.9	31.4	32.1	23.8	10.2	48.0	27.9	22.8	26.7
Si	12.5	10.4	10.5	2.6	1.5	0.1	7.0	2.0	9.6
Al	1.0	0.9	0.6	11.3	3.0	0.2	5.0	10.1	1.6
Fe	0.4	0.4	0.2	4.2	1.1	0.2	2.7	7.5	0.5
Mg	0.5	0.9	0.9	2.5	29.6	1.4	1.4	1.9	1.8
S	0.5	0.2	0.1	0.2	1.2	0.0	0.2	0.1	1.9
Na	0.3	0.1	0.1	0.1	0.2	0.1	0.1	0.1	0.5
K	0.3	0.2	0.0	0.2	1.0	0.0	0.1	0.1	1.5
Vol. %	4.8	9.7	64.7	4.1	1.2	1.7	5.9	5.8	2.1

Table 9.2. Chemical composition expressed in atomic percent for the statistically distinct clusters for the bulk samples (a) *B-C2* and (b) *B-C4*. Based on the chemical composition, each cluster is identified either as a mixture, *Mix*, of several phases or as one of the clinker phases: alite, *A*; belite, *B*; interstitial phase, *I*; free lime, L; or magnesium-rich phase, *M*.

Phase	Alite	Belite	Aluminate			Ferrite	
			Cubic	Ortho.	Low Fe	Typical	Low Al
Symbol	*A*	*B*	*C*	*C'*	C^-	*F*	F^-
O	55.4	56.7	54.8	54.4	55.0	55.5	55.7
Ca	32.2	28.0	24.8	24.0	25.3	22.0	21.9
Si	10.6	13.0	1.6	1.8	1.8	1.6	2.2
Al	0.4	1.0	15.2	14.2	16.1	11.1	8.4
Fe	0.2	0.3	1.6	2.1	0.3	6.9	8.4
Mg	0.7	0.3	0.8	0.7	0.6	1.9	2.4
S	0.1	0.1	0.0	0.0	0.0	0.0	0.0
Na	0.1	0.1	0.8	0.5	0.3	0.1	0.3
K	0.1	0.4	0.4	2.1	0.3	0.1	0.1

Table 9.3. Typical composition expressed in atomic percent for clinker mineralogical phases, as published by Taylor [121].

The interstitial phases are further analyzed with additional representations of the clustered datasets (including *Al* and *Fe* contents), as shown in Fig. 9.2ab. According to the results, the

interstitial phase of clinker C2 seems to be a combination of ferrite, aluminate and aluminate orthorhombic, without significant contributions of low-Fe aluminate and low-Al ferrite. Similar observations are made for the other clinkers of this study, except for clinker C4, which may contain low-Fe aluminate as shown in Fig. 9.2cd.

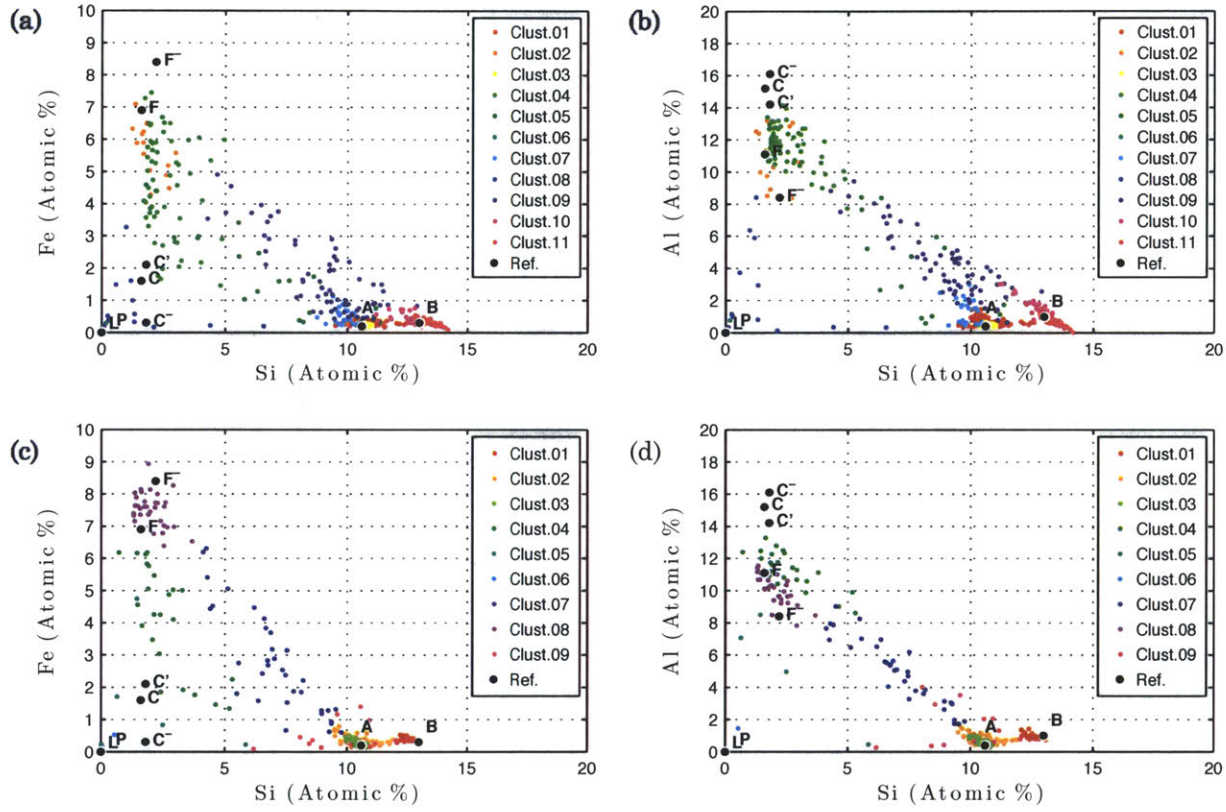

Fig. 9.2. Additional representations of the clustered results for bulk samples: *Fe* vs. *Si* representation for samples (a) *B-C2* and (c) *B-C4*; *Al* vs. *Si* representation for samples (b) *B-C2* and (d) *B-C4*. The reference phases are the following: alite, *A*; belite, *B*; aluminate, *C*; aluminate orthorhombic, *C'*; aluminate low-Fe, *C⁻*; ferrite, *F*; ferrite low-Al, *F⁻*; free lime, *L*; and periclase, *P*.

9.2.2 Analysis of Ground Samples

As illustrated for clinkers *C2* and *C4* in Fig. 9.3, the results obtained for coarsely ground and finely ground samples are similar to those of the bulk samples. Pure alite and belite phases are identified for most samples, except for sample *F-C4b* in which the number of probes corresponding to belite is too low to be clustered as an independent phase (see Fig. 9.3d). In addition, pure free lime is not measured for ground samples. Free lime is known to be a soft clinker phase, with Mohs' hardness of 3 to 4 compared to 4 to 6 for the other main

clinker phases [22], and clinker grinding may result in overgrinding of lime which prevents its experimental identification.

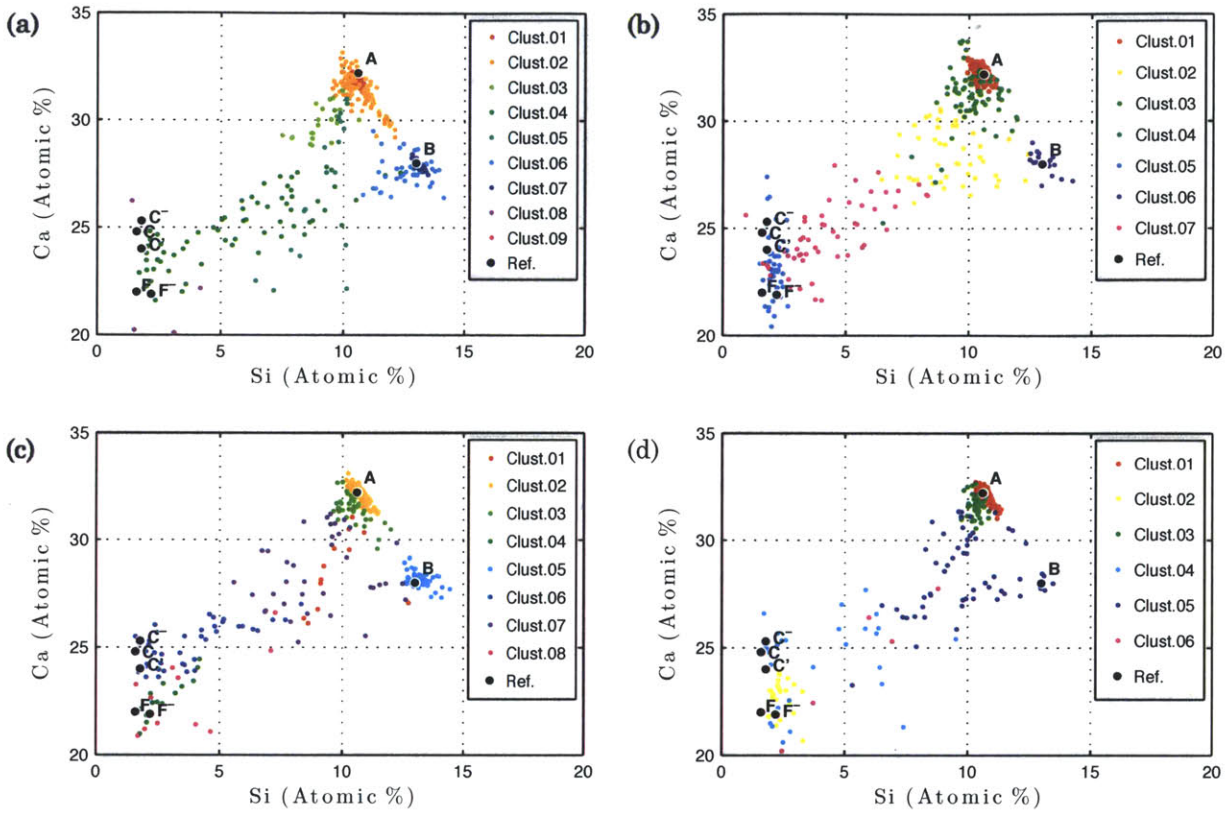

Fig. 9.3. *Si* vs. *Ca* representation for coarsely ground samples (a) *C-C2a* and (b) *C-C4b* and finely ground samples (c) *F-C2a* and (d) *F-C4b*. The reference phases are the following: alite, *A*; belite, *B*; aluminate, *C*; aluminate orthorhombic, *C'*; aluminate low-Fe, *C-*; ferrite, *F*; and ferrite low-Al, *F-*.

The influence of sample preparation is further analyzed with the comparison of alite and belite phase compositions, as presented in Table 9.4. These results validate that the use of ground samples does not significantly affect the measured composition of the pure phases, as the relative error compared to bulk samples is lower than 2-5% for major elements. In addition, these results also illustrate the repeatability of the measurements, as very similar values are obtained with two grids (a and b) performed on the same sample.

Phase	Alite					Belite				
Sample	*B-C2*	*C-C2a*	*C-C2b*	*F-C2a*	*F-C2b*	*B-C2*	*C-C2a*	*C-C2b*	*F-C2a*	*F-C2b*
O	55.5	55.5	55.5	55.6	55.5	57.0	56.9	57.0	57.1	57.0
Ca	32.2	31.8	31.6	32.1	32.3	28.1	27.9	27.8	28.2	28.2
Si	10.7	10.5	10.6	10.7	10.6	13.3	13.1	13.3	13.2	13.2
Al	0.5	0.6	0.6	0.5	0.5	0.7	0.8	0.7	0.8	0.8
Fe	0.2	0.3	0.3	0.3	0.2	0.3	0.4	0.3	0.4	0.4
Mg	0.9	1.1	1.1	0.8	0.9	0.3	0.5	0.5	0.3	0.3
S	0.0	0.0	0.0	0.0	0.0	0.0	0.1	0.1	0.1	0.1
Na	0.1	0.2	0.2	0.0	0.0	0.2	0.4	0.3	0.0	0.1
K	0.1	0.1	0.1	0.1	0.1	0.4	0.4	0.4	0.4	0.4

Table 9.4. Comparison of alite and belite compositions in atomic percent, for clinker *C2* with different types of sample preparation: bulk sample (*B-C2*), coarsely ground sample (*C-C2* with grids *a* and *b*) and finely ground sample (*F-C2* with grids *a* and *b*).

9.3 Abundance of the Clinker Phases

9.3.1 Processing of EPMA Results

Following chemistry analyses, the grid EPMA datasets are used to determine the abundance of the identified main clinker phases. Based on the *Ca* vs. *Si* representation expressed in weight fractions (see Fig. 9.4), the method consists of considering each single probe i either as a pure phase or as a combination of $j=1...n$ pure phases. The relative weight fractions, $\eta_{m,ji}$, are determined for each probe i by a linear system of equations based on the previously determined chemical composition of the n constituting phases (the n clustering poles). Densities of main clinker phases, ρ_i, are used to convert relative weight fractions, $\eta_{m,ji}$, into relative volumetric fractions, $\eta_{v,ji}$, as shown in Eq. (9.1). Then, volume fractions of clinker phases are obtained by averaging the relative volumetric fractions for the N probes of a sample, as defined with Eq. (9.2).

$$\eta_{v,ji} = \frac{\eta_{m,ji}/\rho_j}{\sum_{j=1}^{n}(\eta_{m,ji}/\rho_j)} \tag{9.1}$$

$$\pi_j = \frac{\sum_{i=1}^{N}\eta_{v,ji}}{N} \tag{9.2}$$

As illustrated in Fig. 9.4a, data processing is performed in a three step process to treat successively (1) impurities, (2) free lime and (3) major clinker phases. In the first step,

probes not associated with the clinker main phases and having low *Ca* contents are removed and considered as impurities (impurity threshold is set to *Ca* content below 30 wt%).

In the second step, probes with *Ca* content above the alite pole, which are almost exclusively located on the *free lime-alite-belite* line, are assumed be a mixture of free lime and alite. This is a reasonable assumption considering that neighboring free lime and belite crystals is unlikely to occur [20], as these phases are expected to combine into alite under adequate clinkering conditions (i.e., no excess alkali, sufficient burning temperature) [22]. The relative fraction for each phase is determined according to the system of equations (9.3) based on the calcium content, *Ca*, of the investigated probe, Ca_i, the alite pole, Ca_A, and the free lime pole, Ca_L.

$$\begin{aligned} Ca_i &= Ca_A * \eta_{Ai} + Ca_L * \eta_{Li} \\ 1 &= \eta_{Ai} + \eta_{Li} \end{aligned} \tag{9.3}$$

The remaining data points are considered as mixtures of the main clinker phases and are treated in a third step. The system of equations (9.4) based on *Ca* and *Si* contents is used to determine, for each data point *i*, the relative contributions of alite, η_{Ai}, belite, η_{Bi}, and interstitial phases, η_{Ii}.

$$\begin{aligned} Ca_i &= Ca_A * \eta_{Ai} + Ca_B * \eta_{Bi} + Ca_I * \eta_{Ii} \\ Si_i &= Si_A * \eta_{Ai} + Si_B * \eta_{Bi} + Si_I * \eta_{Ii} \\ 1 &= \eta_{Ai} + \eta_{Bi} + \eta_{Ii} \end{aligned} \tag{9.4}$$

All data points associated with the three main clinker phases should theoretically be located inside the compositional simplex formed by the three poles. As shown in Fig. 9.4a, this is not the case because of inherent error on the measurements. Thus, mixtures of two phases are not precisely located on a line between the two poles, but distributed around this line. Such distribution leads to unrealistic solutions with negative relative weight fractions. To avoid this situation, the points outside of the defined simplex are projected on the boundaries and summits, as illustrated in Fig. 9.4b.

The results obtained with this procedure are presented in Table 9.5. A decrease in free lime content from bulk samples to ground samples is generally observed, which is in agreement with previous qualitative observations. Cement clinkers typically contain about 1% of free

lime, which can easily ground too finely to be detected [22]. The quantitative results for coarse samples therefore indicate an underestimation of free lime with the proposed methodology. In addition, high variability between samples is observed for the amount of impurities, which indicates that the results for minor phases may be used qualitatively but that the quantitative values need to be considered with care. Smaller variability is measured on the abundance of the clinker main phases and these results are further analyzed in the following sections.

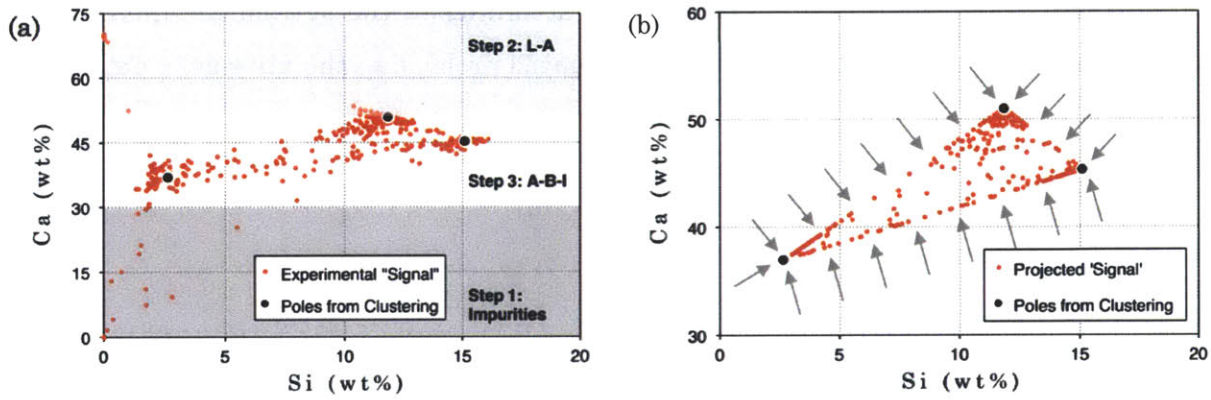

Fig. 9.4. (a) Experimental "signal" of sample *B-C2* with illustration of the data processing steps: (1) the impurities are removed; (2) the points above the alite pole are considered as mixtures of free lime, *L*, and alite, *A*; (3) the remaining points are distributed between the three main clinker phases (alite *A*, belite *B* and interstitial *I*). (b) Projection of the points outside of the alite-belite-interstitial compositional simplex.

9.3.2 Comparison with XRD Results

As presented in Table 9.5, the results obtained both with the EPMA and XRD investigations are compared in volumetric percent for the clinker main phases (see section 8.2 for complete XRD results). The results are first normalized to the total content of the main clinker phases (alite, belite and interstitial) and the relative errors on the EPMA results are then determined using the XRD results as reference values. The three types of sample preparation are compared with single grids (*a* or *b*) or combination of two grids (*a*+*b*): the bulk samples (*B*-), coarsely ground (*C*-) and finely ground (*F*-) samples. Further analysis of these results is presented in the discussion.

Sample	Method	Minor Phases (v%)		Norm. Fractions (v%)			Relative Error (%)		
		Lime	Impurities	Alite	Belite	Interst.	Alite	Belite	Interst.
C1	**XRD**			**69**	**14**	**18**			
B-C1	*Bulk*	*2.1*	*0.9*	*76*	*12*	*13*	*10*	*13*	*28*
C-C1 (a)	*Coarse*	*0.6*	*0.0*	*68*	*15*	*17*	*1*	*9*	*3*
C-C1 (b)	*Coarse*	*0.8*	*0.0*	*71*	*12*	*16*	*4*	*9*	*8*
C-C1 (a+b)	Coarse	0.8	0.0	71	13	16	3	4	10
F-C1 (a+b)	*Fine*	*0.4*	*1.9*	*69*	*12*	*19*	*1*	*14*	*8*
C2	**XRD**			**62**	**20**	**18**			
B-C2	*Bulk*	*1.3*	*2.3*	*61*	*22*	*17*	*2*	*8*	*3*
C-C2 (a)	*Coarse*	*0.3*	*1.3*	*63*	*23*	*15*	*1*	*12*	*17*
C-C2 (b)	*Coarse*	*0.3*	*2.0*	*60*	*24*	*16*	*3*	*16*	*7*
C-C2 (a+b)	Coarse	0.3	1.7	61	24	15	2	16	12
F-C2 (a+b)	*Fine*	*0.4*	*2.0*	*57*	*25*	*18*	*8*	*21*	*5*
C3	**XRD**			**74**	**11**	**16**			
B-C3	*Bulk*	*0.2*	*0.9*	*72*	*8*	*20*	*3*	*22*	*27*
C-C3 (a)	*Coarse*	*0.6*	*1.3*	*71*	*10*	*19*	*3*	*3*	*18*
C-C3 (b)	*Coarse*	*0.4*	*2.3*	*73*	*11*	*16*	*0*	*3*	*3*
C-C3 (a+b)	Coarse	0.8	1.7	71	12	17	4	9	11
F-C3 (a+b)	*Fine*	*0.8*	*1.9*	*69*	*10*	*20*	*6*	*4*	*29*
C4	**XRD**			**66**	**13**	**21**			
B-C4	*Bulk*	*1.9*	*1.0*	*78*	*8*	*13*	*18*	*35*	*36*
C-C4 (a)	*Coarse*	*0.4*	*1.5*	*68*	*10*	*22*	*3*	*22*	*6*
C-C4 (b)	*Coarse*	*0.5*	*0.4*	*67*	*12*	*21*	*1*	*9*	*4*
C-C4 (a+b)	Coarse	0.5	0.8	67	11	22	1	15	5
F-C4 (a+b)	*Fine*	*0.4*	*1.8*	*69*	*11*	*20*	*4*	*18*	*1*

Table 9.5. Abundance of clinker minor phases (v%) and clinker main phases (normalized v%), with relative error compared to XRD results (normalized v%). B = Bulk samples; C = Coarsely ground sample; F = Finely ground sample; a = First grid; b = Second grid.

9.4 Bulk Chemistry

9.4.1 EPMA Average Chemistry

Under the assumption that the "signal" of the EPMA datasets is representative of the whole clinker, a good approximation for the bulk chemistry is expected from averaging the chemistry over all the data points. To facilitate the comparison with X-ray fluorescence (XRF) measurements, the average chemistry obtained from the elemental atomic fractions is converted into oxides weight fractions. The EPMA average chemistry of each clinker is presented Table 9.6, as calculated with the results obtained for coarsely ground samples with two experimental grids (*a*+*b*).

9.4.2 XRF Results and Comparison

The oxide compositions (wt%) measured by XRF are also reproduced in Table 9.6 (see section 8.4 for more details). These compositions are considered as the reference values for validation of the EPMA averaging method. However, it is worth reminding that the relative error on the XRF method itself ranges from <5% for the four major oxides up to 100% for the trace oxides.

As shown in Table 9.6, similar error is obtained when comparing the two methods (below 5-10% for the main four oxides and up to 75% for trace oxides), which indicates a good agreement given the accuracy of the XRF measurements. In addition, it is observed that the main oxides tend to be slightly overestimated by the EPMA method while the trace oxides are generally underestimated. This may be attributed to the limits of the statistical representativeness of the sieved "signal". Trace elements may be either substitutions in the major phases or localized concentrations in the clinker matrix. The error on the latter is expected to be larger in the discrete EPMA probing, as the overall concentrations of trace elements are generally less than a percent. Nevertheless, it is interesting to note that the relative trends between clinkers are relatively consistent for the two methods (e.g., SO_3 content). In addition, other trace oxides measured with XRF (i.e., TiO_2, P_2O_5, Mn_2O_3 and SrO) were not included in the EPMA measurements.

Method	**EPMA Average Chemistry**				**XRF Bulk Chemistry**			
Sample	*C-C1*	*C-C2*	*C-C3*	*C-C4*	*C1*	*C2*	*C3*	*C4*
CaO	67.6	64.9	65.7	65.8	65.5	64.2	64.6	64.1
SiO_2	22.3	22.8	20.9	21.1	20.6	20.7	19.6	20.2
Al_2O_3	4.9	4.5	4.7	6.7	5.0	4.9	4.7	6.3
Fe_2O_3	3.0	3.0	3.6	3.1	3.0	3.1	3.6	2.9
MgO	0.7	3.0	2.4	1.9	2.9	4.3	2.5	2.6
SO_3	0.2	0.2	0.7	0.4	0.5	0.5	1.6	1.2
Na_2O	0.1	0.4	0.2	0.2	0.3	0.3	0.3	0.3
K_2O	0.3	0.4	0.4	0.3	0.5	0.7	0.9	1.1
Others	-	-	-	-	0.6	0.5	0.7	0.9
LOI	1.0	0.8	1.5	0.5	1.0	0.8	1.5	0.5

Table 9.6. Oxide weight percent measured by averaging EPMA results for all the valid data points obtained for the coarse samples (grids a+b). The results from XRF are presented for comparison. The EPMA results are in agreement for the major oxides (relative error < 5-10%), with a tendency for underestimation of the minor oxides. Note that the loss of ignition, LOI, is measured with a complementary method and is thus the same for both sets of results.

9.5 Discussion

9.5.1 Optimal Experimental Protocol

9.5.1.1 Representativeness of the Probed Surface

An important consideration regarding the experimental protocol is the choice of sample preparation. Although bulk samples are simpler to prepare, the quality of the quantitative phase abundance was found not to be constant from clinker to clinker with this method. The relative error ranges from less than 10% to more than 30%, as presented in Table 9.5. To investigate this behavior, additional grid measurements were performed on two bulk samples of clinker *C3*, prepared from two different clinker nodules (samples *B-C3-1* and *B-C3-2*). As shown in Table 9.7, variations in the phase abundance are measured from one nodule to the other (*B-C3-1* vs. *B-C3-2*), indicating non-uniformity in clinker composition. In addition, the belite content is found to vary from grid to grid probed on the same sample *B-C3-2* (*a* vs. *b* vs. *c*). These variations are explained by the nested distribution of the belite crystals, as illustrated in Fig. 7.9c. Thus, limited accuracy on the average abundance of the phases is obtained from bulk samples. Testing of larger representative surfaces on several nodules would be required to improve this accuracy.

Sample	*Method*	Norm. Fractions (vol.%)		
		Alite	Belite	Int.
C3	**XRD**	**74**	**11**	**16**
B-C3-1 (a)	*WDS-Bulk*	*72*	*8*	*20*
B-C3-1 (b)	*WDS-Bulk*	*72*	*8*	*20*
B-C3-1 (c)	*WDS-Bulk*	*73*	*10*	*18*
B-C3-2 (a)	*WDS-Bulk*	*70*	**15**	*15*
B-C3-2 (b)	*WDS-Bulk*	*78*	**8**	*13*
B-C3-2 (c)	*WDS-Bulk*	*72*	**12**	*15*

Table 9.7. Abundance of the clinker main phases calculated for two samples of clinker C3 (*B-C3*-a and *B-C3-2*) with three independent grids (*a*,*b*,*c*) on each sample.

To ensure representativeness of the probed surfaces, an alternative approach is the use of epoxy-embedded ground samples. With this approach, a sufficiently large grid located randomly on a single sample is expected to be representative of the average clinker properties. However, optimal particle size of the clinker powder needs to be determined. This is done to optimize the compromise between increased representativeness and lower

"noise" in the measurements. On the one hand, finer grinding eliminates uneven distribution of phases, such as belite nests. On the other hand, increasing the surface-to-volume ratio of the probed particles increases both the particle-effect and the surface roughness, which affects the quality of the quantitative chemistry measured with the EPMA [45,9]. This loss of quality is observed with the raw data sieving, as presented in Table 9.1. The "signal" represents 30-45% of total probes for finely ground samples, compared to 45-50% for coarsely ground samples.

9.5.1.2 Validation of the Sieving Method

Geometrical Model

To support the sieving method proposed in this study, a geometrical model is developed to determine the probability of having the whole EPMA interaction volume landing on a single particle, as schematized in Fig. 9.5. This probability is modeled based on the surface distribution of particles, with Eq. (9.5) and Eq. (9.6). In order to apply the model, the areas of the j=1...n particles, $A_P^{(j)}$, are extracted from the SEM image analyses (see section 7.2) along with the total surface of the analyzed image, S. The radius of each particle, $R_P^{(j)}$, is calculated assuming circular particles and the probe interaction radius, R_{IV}, is retrieved from previous simulations (section 5.2.1).

$$P[valid] = \frac{\sum_j^n \pi \left(R_P^{(j)} - R_{IV}\right)^2}{S}, \; R_P^{(j)} > R_{IV} \tag{9.5}$$

$$R_P^{(j)} = \sqrt{A_P^{(j)}/\pi} \qquad (1) \tag{9.6}$$

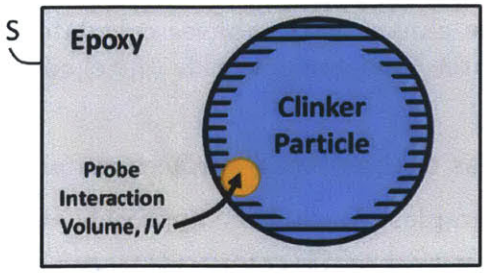

Fig. 9.5. Schematic representation of the geometrical model used to validate the data sieving method. The model estimates the probability of having the whole EPMA interaction volume landing on clinker particles, based on SEM image analyses of the probed samples.

Comparison of the Modeled Probability and the Sieving Ratios

For each clinker, the probability of a valid measurement, *P[valid]*, is determined as a range with upper and lower bounds calculated from the variability in the inputs, i.e., the interaction radius ranging between 0.5 and 0.75 μm, and the six SEM micrographs independently analyzed for each clinker. As presented in Table 9.8, the experimental sieving ratios are in general agreement with the modeled probability of valid probing, considering the simplifying assumptions of the model and the additional factors influencing the analytical totals (e.g., surface roughness, defects, pores, and cracks).

Clinker	Coarsely ground			Finely ground		
	P[valid]	*Grid a*	*Grid b*	*P[valid]*	*Grid a*	*Grid b*
C1	[47%, 53%]	43%	47%	[32%, 39%]	45%	38%
C2	[46%, 52%]	45%	45%	[34%, 39%]	40%	46%
C3	[45%, 51%]	52%	47%	[32%, 41%]	39%	42%
C4	[45%, 51%]	47%	46%	[30%, 35%]	30%	31%

Table 9.8. Modeled probability of a valid probe for coarsely and finely ground samples of each clinker. "Signal" sieving ratios are also provided for each experimental grid (*a* and *b*).

9.5.1.3 Grid Characteristics and Expected Accuracy

The modeling results indicates that the maximum proportion of expected valid probes is 45-50% for coarsely ground samples, compared to 30-40% for finely ground samples. This relatively low level of valid probes has an influence on the statistical representativeness of each single grid, as less than half of the 1024 acquired points are used in the analyses.

The effect of this reduction is demonstrated with coarsely ground samples in Table 9.5. The relative error in phase abundance calculated from single grids (*a* or *b*) reaches 20%. The combined analysis of the two grids (*a*+*b*) results in relative errors lower than 5% for the alite content and lower than 15% for the belite and the interstitial contents. However, the results for finely ground samples lack accuracy regarding phase abundance even with the combination of two grids.

The prescribed spacing between the EPMA spot analyses (section 5.2.2) is validated by the median equivalent particle diameters, which range between 35 and 45 μm for coarsely ground samples. The majority of the particles are unlikely to be probed twice with the

prescribed 60 μm spacing, which ensures representativeness of the average clinker properties.

Finally, as chemistry analyses were found to be equivalent for the different types of sample preparation (section 9.2.2), the recommended experimental protocol consists of probing grids of 2048 points spaced by 60 μm on coarsely ground samples having median equivalent particle size ranging from 35 to 45 μm.

9.5.2 Polymorphism of the Alite Phase

Different polymorphs of the main clinker phases may be found in industrial clinkers. Polymorph identification is of interest because of the potential effects on the grinding and hydraulic properties of cement. In particular, two polymorphs of the alite phase (M_1 and M_3) may be present in industrial clinkers.

As described in section 8.1, the alite polymorphism is related to the supersaturation of the melt. High supersaturation, favored by sufficient amounts of MgO and/or high firing temperature, results in high intensity of nucleation which leads to the stabilization of the polymorph M_3, as described by Maki *et al.* [76,75]. On the contrary, low supersaturation of the melt and lower viscosity, favored by the presence of SO_3, results in lower intensity of nucleation leading to unstable growth of larger crystals of the polymorph M_1 [76,75].

If alite polymorphism may be determined with XRD spectra, polymorph identification may also be performed by analysis of the clinker chemical signature. The polymorph M_3 is associated with higher magnesium content and the polymorph M_1 with higher sulfur content. According to the bulk chemistry presented in Table 9.6, the clinker *C3* has higher SO_3 content and is thus susceptible to contain the polymorph M_1. This is the case as previously determined with XRD. On the other hand, lower MgO content of clinker *C1* may not be directly correlated with lower content of the polymorph M_3. High kiln temperatures may also contribute to the stabilization of this polymorph, and it seems to be the case for clinker *C1* in which the polymorph M_1 is not observed.

Finally, the chemical analyses performed with the EPMA method also allow identification of polymorphs for the interstitial phases which include three types of aluminates (cubic, orthorhombic and low-Fe) and two types for ferrite (normal and low-Al), as presented in section 9.2.

9.5.3 Limitations

This method is intended for application to conventional industrial clinkers. Testing of other types of clinker or cements with additional phases is not considered in this study, but extensions of the model may be developed.

The combined analysis of aluminate and ferrite into a single phase may be considered as a limitation of this method. The distinction between these two phases is not simple because of their microstructure characterized by intermixed crystals of small size (~2-3μm), as illustrated in Fig. 7.9b. The probing of pure aluminate or ferrite is less likely to occur than the probing of the interstitial mixture, since the interaction volume of the EPMA probe was simulated to be ~1.5 μm in diameter. This mixture is then considered in statistical clustering as a single phase and the chemistry of each phase is limited to qualitative observations (see section 9.2). A perspective solution to calculate aluminate and ferrite abundances is to extend the mixture model with a third dimension (*Fe* or *Al*), using typical reference chemistry for these poles.

Another limitation of the method is related to the particle-effects and the surface roughness. The quantitative chemistry of each data point is obtained from EPMA, after application of the corrections to account for the matrix effects. However, this procedure works under the condition that the probed surface is flat and homogenous, which is not respected for every spot analysis. The data sieving procedure is useful to remove majority of the data points associated with clinker-epoxy transitions, but the probes associated with mixtures of clinker phases are conserved.

The experimental acquisition time of the EPMA is also a limitation of the method, as each single measurement point requires about a minute. To apply the proposed method at the industrial scale in cement plants, the use of tabletop SEM equipped with fast EDS detectors could be an interesting alternative. If this equipment was historically used for qualitative analyses, modern instruments calibrated with quality standards allow accurate quantitative analyses. Thus, this variant of the proposed method is of interest for clinker quality control at cement plants.

9.6 Chapter Summary

In this chapter, a new method using grid electron probe microanalyses (EPMA) was presented to simultaneously measure the chemistry of the clinker phases, their relative abundance, and the bulk clinker chemistry. Testing of the method was performed with four industrial clinkers and three sample preparation methods. The chemistry of alite and belite phases was determined quantitatively with relative error lower than 2-4% for the major elements, in comparison to typical clinker compositions. This quantification also showed excellent repeatability and was not significantly affected by the sample preparation method. In addition, the qualitative analysis of the chemistry of the interstitial phases allowed identification of polymorphs for aluminate (cubic, orthorhombic, low Fe) and ferrite (normal, low Al). A model based on the law of mixtures was proposed to determine the abundance of the clinker phases. The highest accuracy was obtained for relatively large grids (2048 points) performed on epoxy-embedded coarsely ground samples. The comparison with quantitative XRD analyses resulted in relative errors lower than 5% for alite content and lower than 15% for belite and interstitial phase contents. The bulk chemistry was obtained by averaging the measured chemistry for all the valid EPMA data points. Comparison with XRF measurements showed that the accuracy of the EPMA average chemistry was similar to that of the XRF method. A data sieving method was also proposed to extract the "signal" from the raw measurements. Based on Gaussian clustering of the analytical totals, the sieving aims to remove the "noise" (the invalid EPMA measurements caused by probing of epoxy, particle-effects, surface roughness, etc.). The sieving method was further validated with a geometrical model developed to predict the expected "signal"-to-"noise" ratio based on apparent particle size distributions measured with SEM micrographs. Finally, this new method for clinker analysis was developed with EPMA measurements, but the same method could be applied to quantitative SEM-EDS measurements (provided adequate calibration with quality standards). The use of fast and inexpensive SEM-EDS equipment would be of interest for quality control applications at cement plants, considering the future need for monitoring the chemistry of the clinker phases.

Chapter 10

Multi-scale Fracture Toughness

As discussed in Chapter 7, three principal characteristic scales may be defined for clinkers. The separation between these scales is based on the heterogeneities, which consist of the pores and the grains of the clinker phases. This chapter first focuses on the macroscale fracture toughness to investigate the effects of microstructure. Microscratching is then performed between the pores at the intermediate scale to measure the fracture properties of alite and belite clusters. Finally, the testing is further downscaled to measure fracture toughness of single alite and belite grains at the microscale.

10.1 Macroscale: Effects of Microstructure

Microscratching in the Conical Range of the 200 μm Probe

Microscratching was performed in the conical range of a 200 μm indenter probe with the default protocol presented in Table 6.2. Fig. 10.1a presents a typical measurement on clinker, which illustrates the variations caused by the presence of pores.

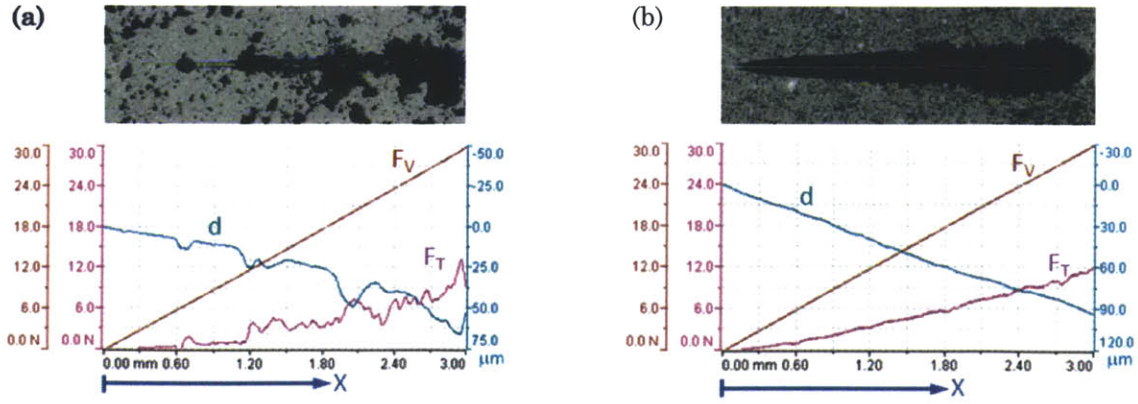

Fig. 10.1. Typical measurements of microscratch tests performed on (a) cement clinker and (b) hydrated cement paste. The prescribed vertical force, F_V, is identical for both samples, while the penetration depth, d, and the horizontal force, F_T, are affected by the porosity.

For comparison, Fig. 10.1b illustrates the same measurement performed on a porous hydrated cement paste. Even though the pores are smaller than those of clinker, the porosity still conflicts with the microscratch method assumption of probing a homogeneous material. However, similarly as in nanoindentation analyses [27], this assumption can possibly be relaxed by ensuring the micromechanics scale separability condition:

$$d_0 \ll \mathcal{L} \ll (d, w, D) \tag{10.1}$$

where $\mathcal{L}$ is the characteristic size of the representative elementary volume, *REV*, which must be larger than the characteristic size of the largest heterogeneity d_0 contained in the *REV*. Also, the characteristic size D of the heterogeneities at a higher scale and the size of the mechanical solicitation must be larger than the *REV*. In the case of the scratch test, the mechanical solicitation relates to the penetration depth d and the width w of the scratch imprint, since the method assumes a succession of horizontal fracture events occurring in front of the perimeter of the probe (see section 6.1.2). In addition, the scratch length must be sufficient to allow these fracture events to reach the load-independent steady state, as required by the microscratch method (see section 6.1.5).

Intrinsic properties of single phases can be measured when the volume of material solicited is small enough not to be influenced by heterogeneities at a higher scale, e.g. $(d, w) \ll D$. In contrast, composite properties are associated with mechanical solicitation larger than the heterogeneities, e.g. $(d, w) \gg D$. The 1/10 or Buckle's rule-of-thumb is generally accepted in the case of nanoindentation [26,66] to define the separation between thescales. In this study, the hypothesis is made that scale separability and the Buckle's rule-of-thumb are valid for the microscratch method. The validation of this assumption is left for future work.

For the measurement presented in Fig. 10.1a, the size of the largest heterogeneities (i.e., pores of ~65-250 μm) was of the same magnitude as the maximum penetration depth $d_{max} \approx 75$ μm, and the scale separability condition was therefore not satisfied. In an attempt to reach this condition, the maximum vertical force was increased to 180N (the limit of the available instruments). The penetration depths increased up to 200-250 μm, but it was still insufficient to measure the composite response including porosity. Fig. 10.2 illustrates the fracture toughness convergence plots for clinker C1 measured with maximum vertical loads of 30N and 180N, respectively. Measurements at higher maximum force resulted in an

uncontrolled scatter of the data associated with large chipping in front of the indenter tip. This approach was abandoned, as no convergence could be obtained with loads up to 180N.

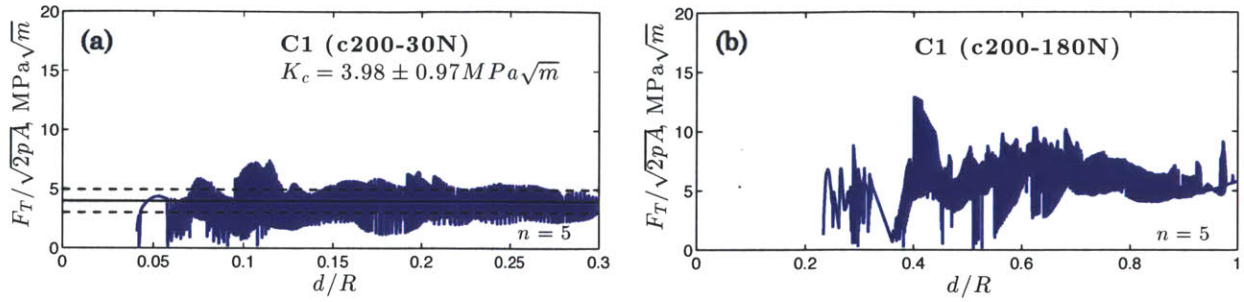

Fig. 10.2. Fracture toughness as a function of the relative penetration depth for clinker C1. The tests are performed in the conical range of the 200 μm probe, *c200*, with maximum vertical load reaching (a) 30N and (b) 180N. High levels of chipping occurring at higher forces up to 180N prevent adequate measurement of fracture toughness.

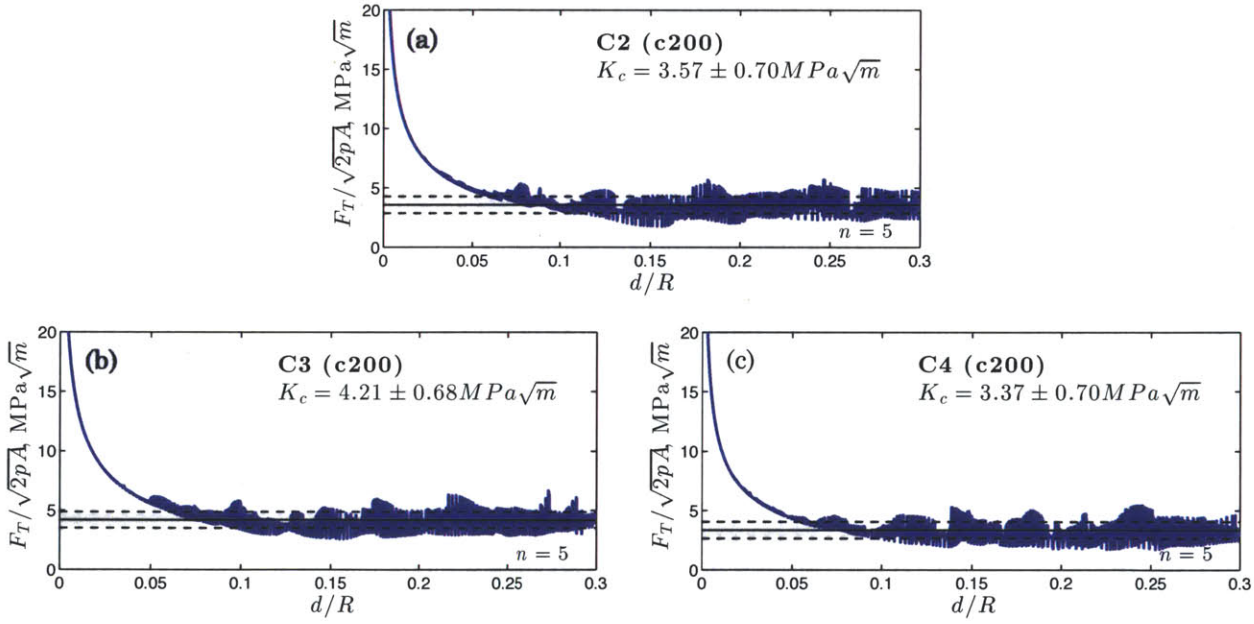

Fig. 10.3. Fracture toughness measured in the conical range of a 200 μm probe (*c200*) for clinkers (a) C2, (b) C3, and (c) C4. Clinker C3 seems to exhibit higher fracture toughness.

These results indicate that the microstructural constrains of clinkers (i.e., relatively large pores and limited available surfaces) limit the separation of scales. Therefore, the macroscale fracture toughness is considered as a local fracture response rather than a composite material property. Nevertheless, this toughness is representative of the clinker microstructure, since each scratch of 3 mm in length consists of a succession of fracture

events occurring over hundreds of grains, boundaries, and pores. In addition, the toughness converges for increasing penetration depths as shown in Fig. 10.2a and Fig. 10.3, which indicates that the steady state of fracture required by the method is obtained. Also, the results were on average reproducible within the experimental error, as shown with 5 independent measurements overlaid for each clinker.

Finally, comparison of the results indicates that clinker C2 and C4 tend to exhibit lower macroscale fracture toughness then clinkers C1 and C3. Possible explanations for these differences are discussed further in Chapter 11.

10.2 Intermediate Scale: Alite and Belite Clusters

Microscratch testing at the intermediate scale of clinkers aimed to measure the fracture toughness of the combined clinker phases without the effects of porosity. The bulk surfaces available for testing were limited to 200 μm x 200 μm, since larger surfaces without pores were not available in the polished clinker specimens (see section 7.2). The use of the 200 μm probe was not possible on these limited surfaces, and microscratching was thus performed in the conical range of the 50 and 20 μm probes.

Microscratching in the Conical Range of the 50 μm Probe

Microscratching was performed on the clinkers with a 50 μm tip, and the protocol was adjusted to fit the scratches on bulk surfaces between pores. Pre-testing showed that microscratching could be achieved on 200 μm x 200 μm surfaces only if the scratch length was reduced to 100 μm and the maximum vertical load to 5N, as illustrated in Fig. 10.4a. To accommodate these constrains, the loading rate was adjusted to 60N/min and the scratch velocity to 1.2 mm/min.

A higher maximum vertical load of 10N was also tested, but was found not to be applicable. First, large chipping along scratch path was observed and this prevented the acquisition of reliable measurements (see Fig. 10.4b). Second, the ratio of scratch velocity over loading rate was found to be insufficient. Fig. 10.4c shows the imprint of a scratch with maximum vertical force of 10N over a length of 0.1 mm. This is more characteristic of an indentation with small horizontal displacement, and it does not represent a scratch path with low vertical displacement.

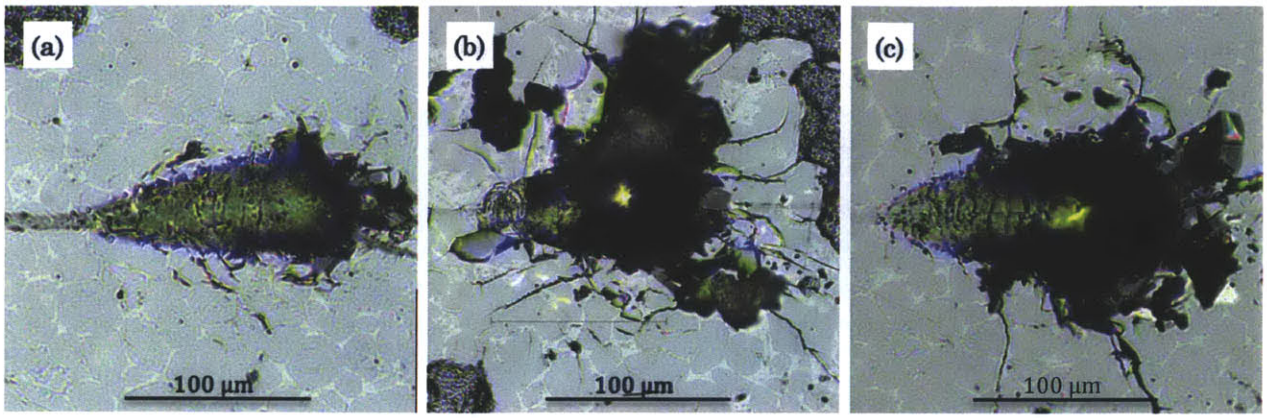

Fig. 10.4. Microscratch imprints of tests performed on clinker C3 with a 50 µm indenter used in the conical range. The maximum vertical forces ranges from (a) 5N to (b,c) 10N.

Microscratching was performed on the four studied clinkers, but the constrained experimental parameters resulted in relatively shallow scratches. The maximum scratch penetration depths did not fully reach the conical range, with maximum $d/R \approx 0.14\text{-}0.16$, in comparison to the conical range criterion $d/R >> 0.134$. The non-negligible contribution of both the conical and the spherical ranges prevented the quantitative evaluation of the fracture toughness for this series of tests.

Nevertheless, optical imaging of scratch paths allowed interesting observations regarding the propagation of cracks in the clinker matrix. The microscratch model by Akono and Ulm [6,4] assumes multiple fracture events occurring along the scratch path. The succession of semi-circular cracks in the scratch imprint shown in Fig. 10.5b suggests that this assumed behavior is correct.

In addition, radical cracks surrounding scratch paths illustrate preferential failure regions of the clinker matrix, as illustrated in Fig. 10.5 and Fig. 10.6. To quantify the relative occurrence of different crack propagation behaviors, *crack sections* were counted on a total of 16 scratched surfaces, half for alite-rich zones (eg. Fig. 10.5a and Fig. 10.6a) and half for belite-rich zones (eg. Fig. 10.5b and Fig. 10.6b). Clinker C4 was not considered in this analysis because of its different microtexture (absence of both alite micro-cracking and belite nests). A *crack section* is defined as a strait crack segment located on a single phase or interface. In addition, *crack sections* are grouped in four different types based on the phase in which they propagate: alite grains, belite grains, interstitial phases or grains interfaces.

A distinction is also made for fractures following pre-cracks, identified with images taken before scratching.

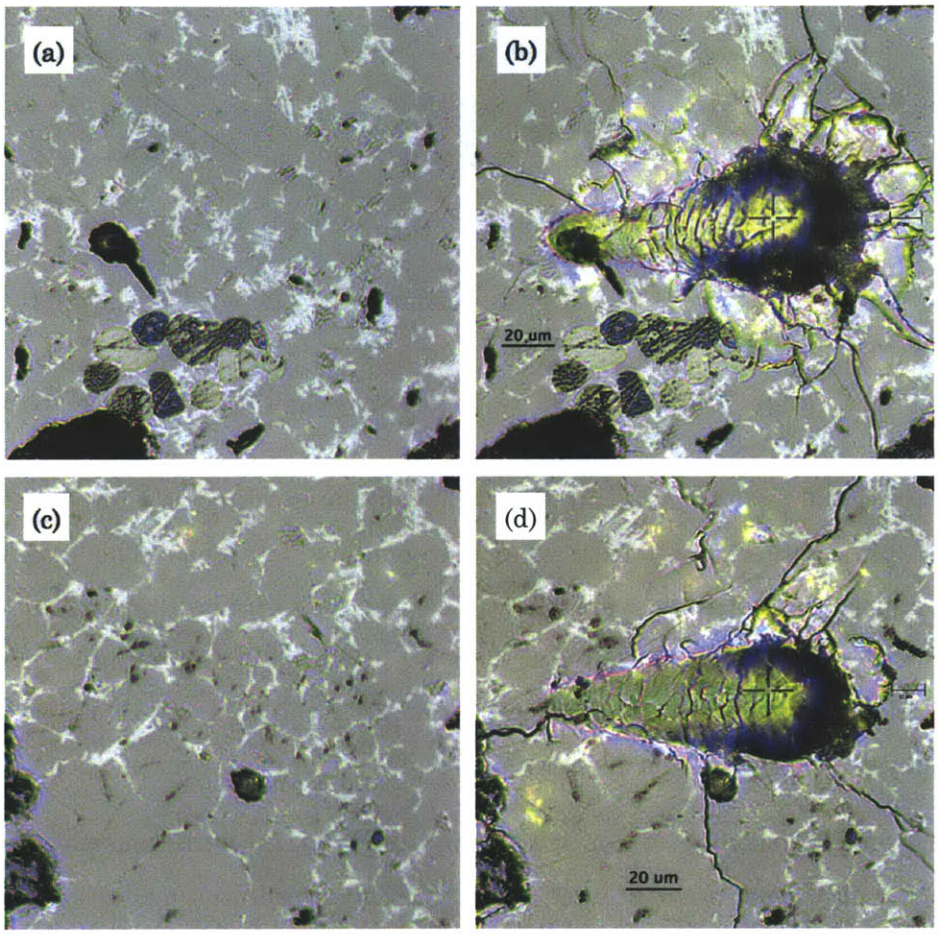

Fig. 10.5. Bulk surfaces of clinker C2: alite-rich region (a) before and (b) after microscratching; belite-rich region (c) before and (d) after microscratching. The tests are performed at the intermediate scale with the 50 µm tip used in the conical range.

Table 10.1 shows that the relative propagation of cracks trough the different grains and interfaces of clinkers is different for alite-rich and belite-rich zones. In the quasi-absence of belite grains, cracks propagate almost equally inside alite grains and between these grains, either in the interstitial phase or at the interfaces. In addition, cracks are more likely to follow interfaces along alite crystals than to propagate into the interstitial phases. This behavior is even stronger with belite grains, as radial cracks mostly contour these grains. Propagation of cracks trough belite crystals is also found in belite-rich clinker zones (23% of *crack sections*), but these are usually located near the scratch imprint, where the indenter probed directly contacts the crystals.

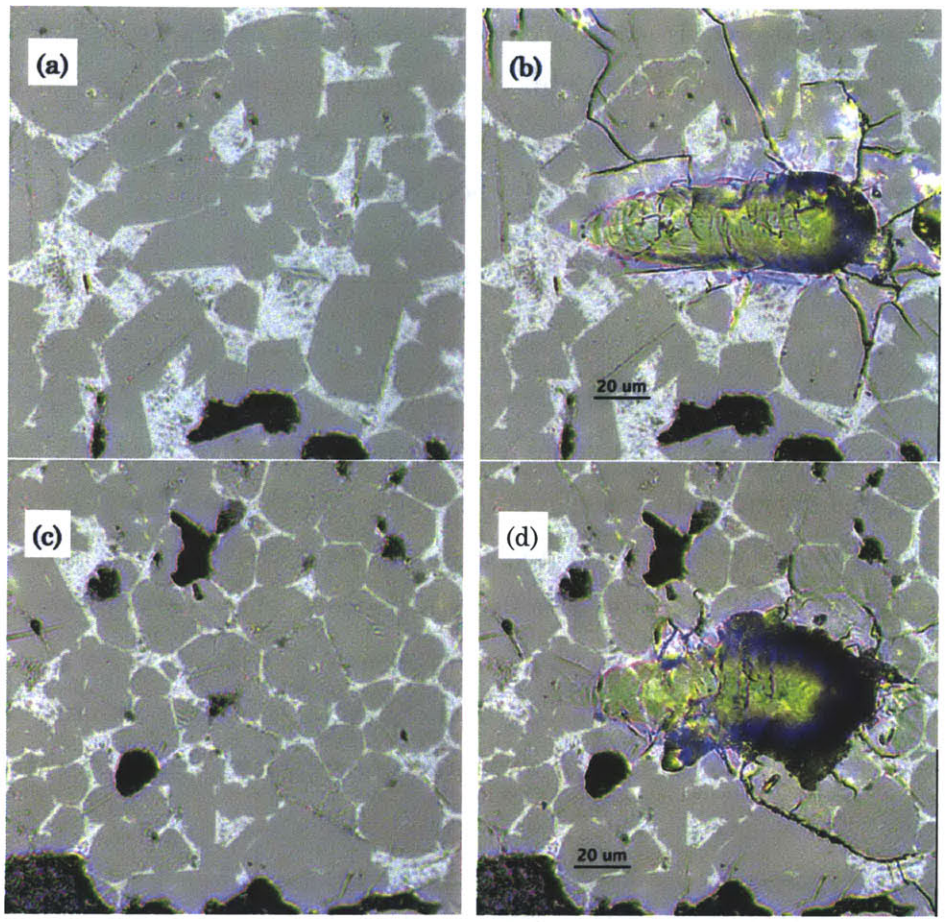

Fig. 10.6. Bulk surfaces of clinker C3: alite-rich region (a) before and (b) after microscratching; belite-rich region (c) before and (d) after microscratching. The tests are performed at the intermediate scale with the 50 μm tip used in the conical range.

Clinker Zone		*Crack Sections* per Grain Type			
		Alite	**Belite**	**Interstitial**	**Interface**
Alite-Rich	(#)	134	7	34	89
	(%)	*51%*	*3%*	*13%*	*34%*
Belite-Rich	(#)	41	47	14	100
	(%)	*20%*	*23%*	*7%*	*50%*

Table 10.1. *Crack sections* per grain type for alite-rich and belite-rich clinker zones. The *crack sections* were counted around the scratch imprint for a total of 16 different scratches.

These results agree with the observations of Hornain and Regourd [53] who stated that the development of cracks in clinkers occurs mainly in pre-cracked alite crystals and at the interfaces between phases. They also suggest that cracks are stopped or deviated by the interstitial phase which is less brittle, and they contour belite crystals which can sustain

more plastic deformations. In this study, the presence of cracks before scratching is observed for all grain types (not just alites) and at interfaces. It was measured that 13% of post-scratch *crack sections* followed these existing cracks, and significant proportion of cracks were initiated at the scratch imprint boundary.

Microscratching in the Conical Range of the 20 μm Probe

Additional testing was performed with an indenter tip of smaller radius to measure fracture properties at the intermediate scale. The conical range (max $d/R \approx 0.3$ - 0.35) was reached with a 20 μm probe in the limited available surfaces between the pores. Preliminary testing was performed to determine the experimental protocol for this series of tests (scratch length = 0.1 mm, maximum vertical force = 4N, loading rate = 24N/min, horizontal tip velocity = 0.6 mm/min). Fig. 10.7 illustrates scratch paths performed with this protocol over several grains of clinker alite and belite. In this case, the scratch width ($w_{max} \approx 30\mu m$) was of the same magnitude as the grain size ($D \approx 20$ *to* $65\mu m$). The intermediate scale fracture toughness is therefore considered as a local fracture response, similarly to the macroscale fracture toughness.

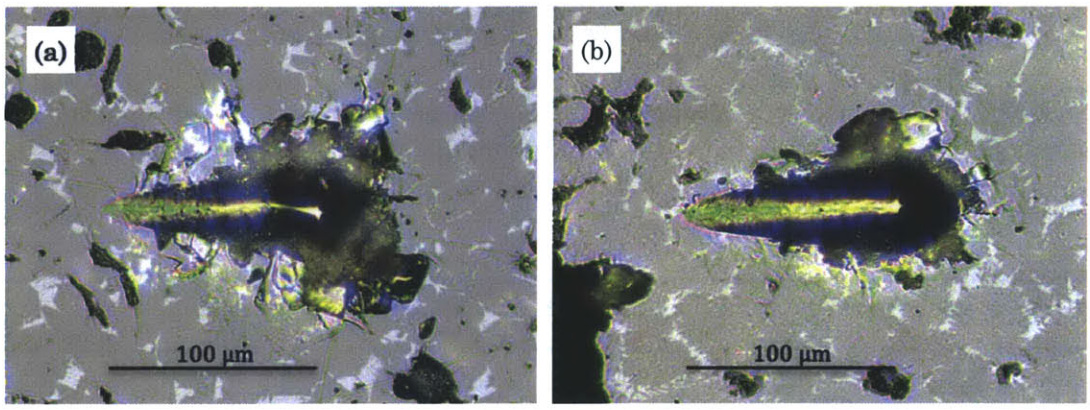

Fig. 10.7. Microscratch imprints from intermediate scale scratching of clinker C1 over (a) an alite-rich region and (b) a belite-rich region. The tests are performed with the 20 μm tip used in the conical range.

Microscratching was performed for each clinker both on alite-rich and belite-rich regions, and the results are presented in Fig. 10.8 and Fig. 10.9. It was not possible to scratch on belite-rich regions on for clinker C4, as the silicates of this clinker were well distributed (i.e., not clustered).

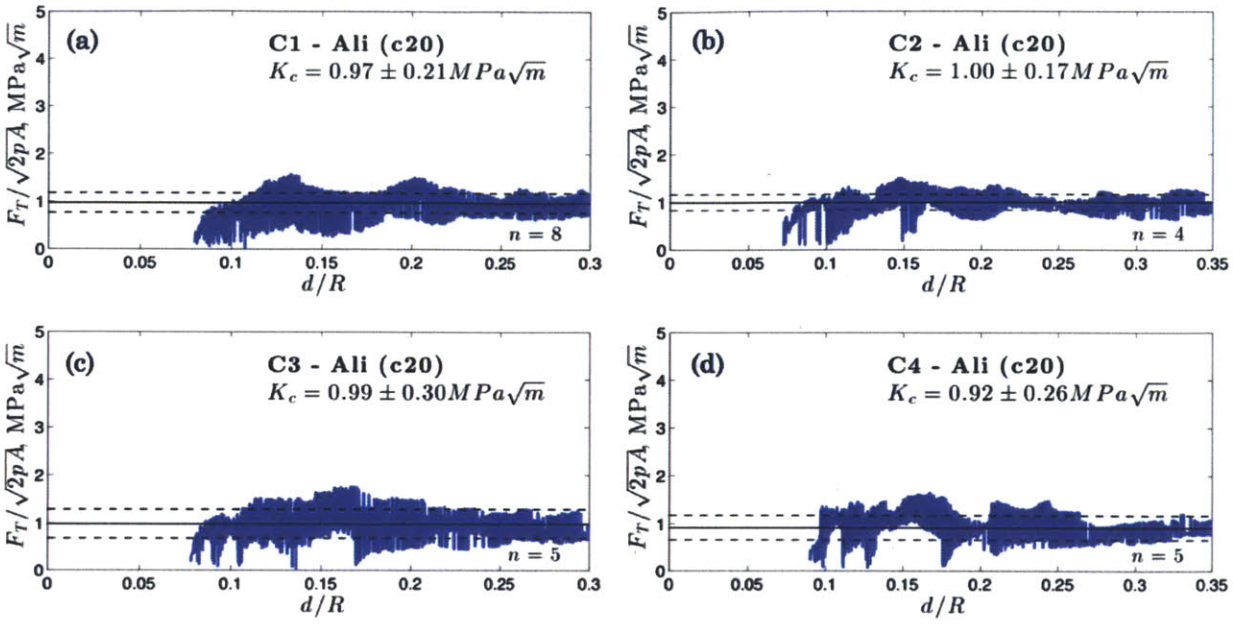

Fig. 10.8. Fracture toughness measured in the conical range of the 20 μm probe, *c20*, for alite-rich regions of clinkers (a) C1, (b) C2, (c) C3, and (d) C4. Results are similar for all clinkers, considering the standard deviations.

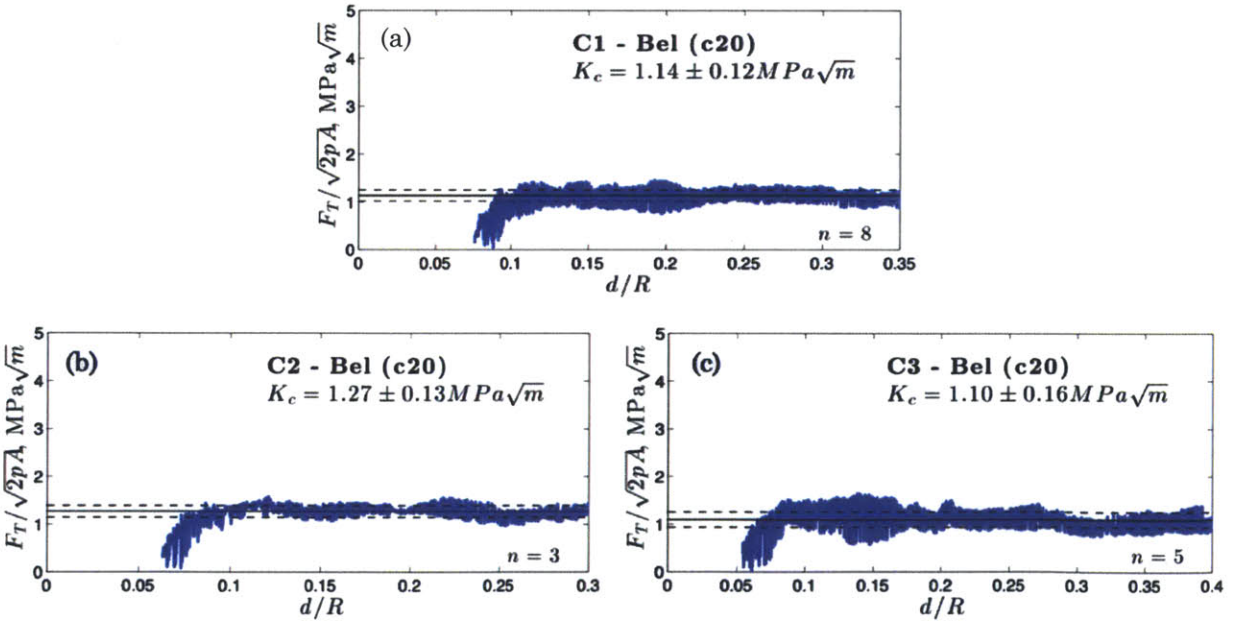

Fig. 10.9. Fracture toughness measured in the conical range of a 20 μm probe (*c20*) for belite-rich regions of clinkers (a) C1, (b) C2, (c) C3, and (d) C4. Clinker C4 is absent from this figure, as belite grains are not clustered.

The toughness measured on alite-rich regions was very similar from clinker to clinker, which suggests that the differences in clinker grindability may not be related to this scale. In addition, the average response of belite-rich regions was higher than that of alite-rich regions, which is in agreement with the grinding literature. Alite crystals are known to be more brittle and micro-cracked, in comparison with rounder and more plastic belite crystals [132,118,53]. The belite crystals also increase significantly the fine grinding energy when they are clustered [74].

10.3 Microscale: Single Alite and Belite Crystals

The microscale of clinkers is characterized by the different clinker phases with grain sizes generally ranging from a few μm up to ~65 μm. At this scale, the objective was to measure the intrinsic fracture properties of alite and belite crystals. By downscaling the microscratch test sufficiently, the testing was performed on surfaces of single grains. Investigation of the interstitial phases was not possible at this scale because of the small crystal sizes and the limitations of the equipment.

Microscratching in the Spherical Range of the 20 μm Probe

To fit scratches on single grains of both alite and belite, the scratch length was limited to 20 μm and the experimental protocol was adapted accordingly (maximum vertical force = 0.5N, loading rate = 15 N/min, horizontal tip velocity = 0.6 mm/min). Fig. 10.10 illustrates the scratch imprints located on single grains of diameters $D \geq 40\mu m$. The penetration depth into the material reached $d_{max} = 0.9\mu m$ at the end of the scratch path, which corresponds to a scratch width of $w_{max} \approx 12\mu m$. Working under the hypothesis that scale separability and the Buckle's rule-of-thumb are valid for the microscratch method (see section 10.1), the scale separability condition is met for the penetration depth but not for the scratch width.

However, the microscratch method assumes successive horizontal fracture events occurring in front of the perimeter of the probe. It follows that the fracture volume is limited to the scratch imprint, even if the stress field covers a larger volume. Therefore, it is assumed that the fracture process occurs entirely on each probed grain and that the neighboring grains do not affect significantly the stress field surrounding the scratch. This is a reasonable assumption considering that the elasticity and hardness of the four main clinker phases are not different by more than 10% (see section 2.1.1). Therefore, the microscale scratching

results are considered as the intrinsic fracture toughness of alite and belite crystals. The results for the four industrial clinkers are presented in Fig. 10.11 and Fig. 10.12.

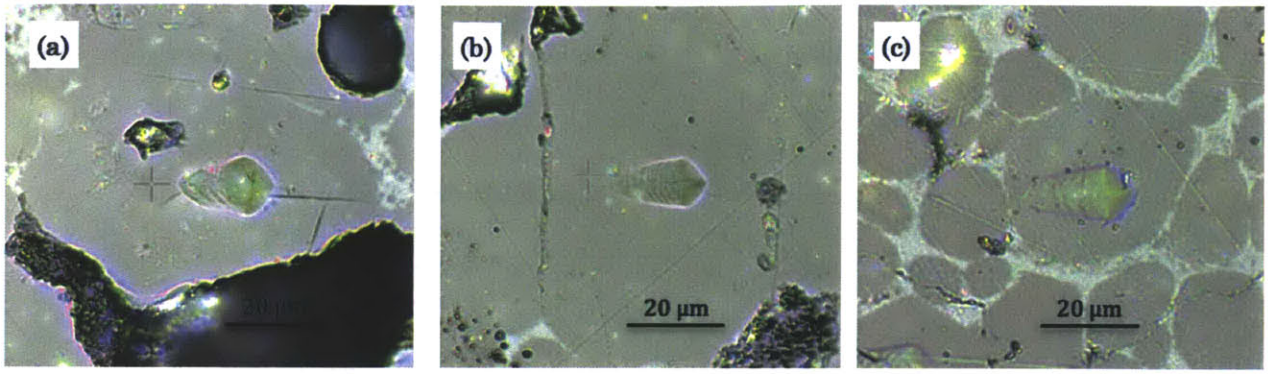

Fig. 10.10. Microscratch imprints from microscale scratching of (a) an alite grain of clinker C2, (b) an oversized alite grain of clinker C3, and (c) a belite grain of clinker C3. The tests were performed with the 20 µm probe used in the spherical range.

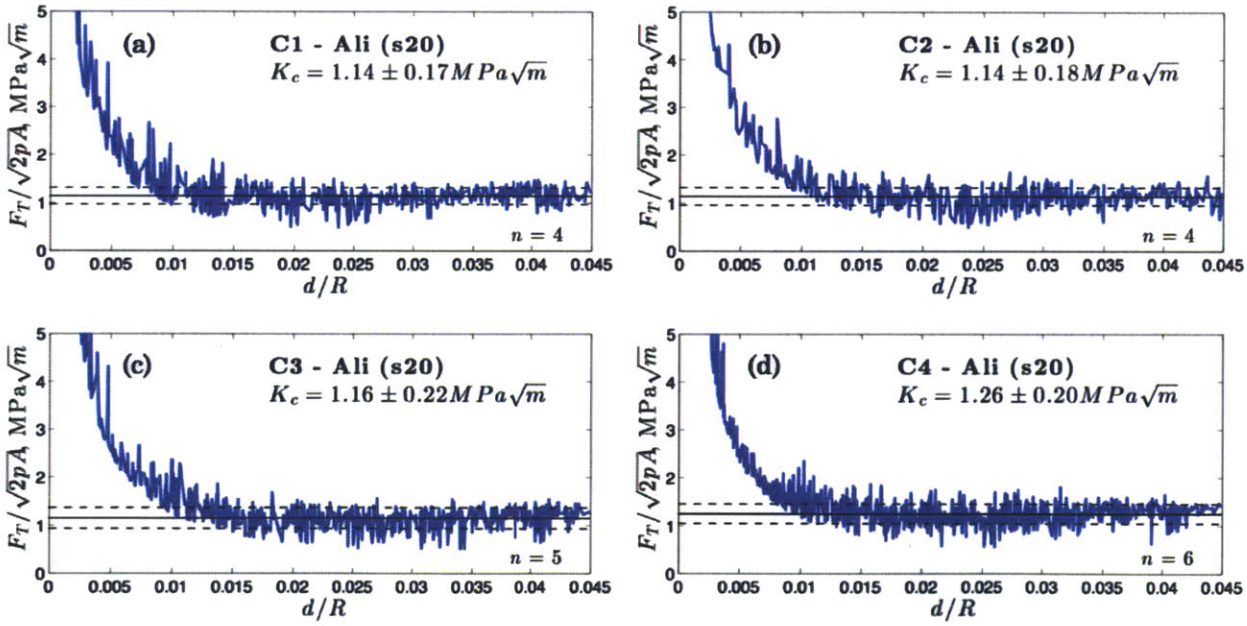

Fig. 10.11. Fracture toughness of alite grains measured with the spherical range of the 20 µm probe, *s20*, on clinkers (a) C1, (b) C2, (c) C3, and (d) C4.

The fracture toughness did not vary significantly from clinker to clinker for each phase. The average measured fracture toughness for alite crystals was ~1.2 ± 0.2 MPa.m^{½}, which is of the same magnitude as the results by Hornain and Regourd [53]. These authors performed Vickers indentation fracture tests and found a toughness of 1.7 MPa.m^{½} for alite crystals.

The values measured in the current study for belite crystals were on average higher than those obtained for alite crystals. This qualitative trend agrees with previous results [53].

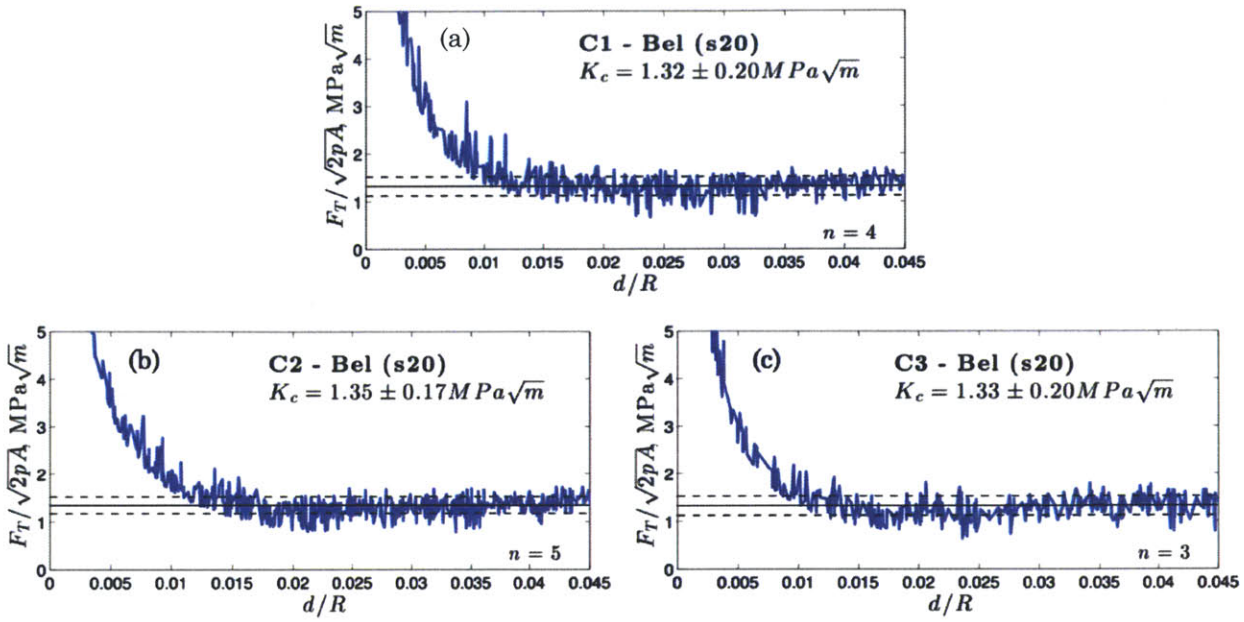

Fig. 10.12. Fracture toughness of belite grains measured with the spherical range of the 20 μm probe, *s20*, on clinkers (a) C1, (b) C2, and (c) C3.

10.4 Chapter Summary

In this chapter, the fracture properties of the studied clinkers were determined. Three characteristic scales were investigated and the results are summarized in Fig. 10.13.

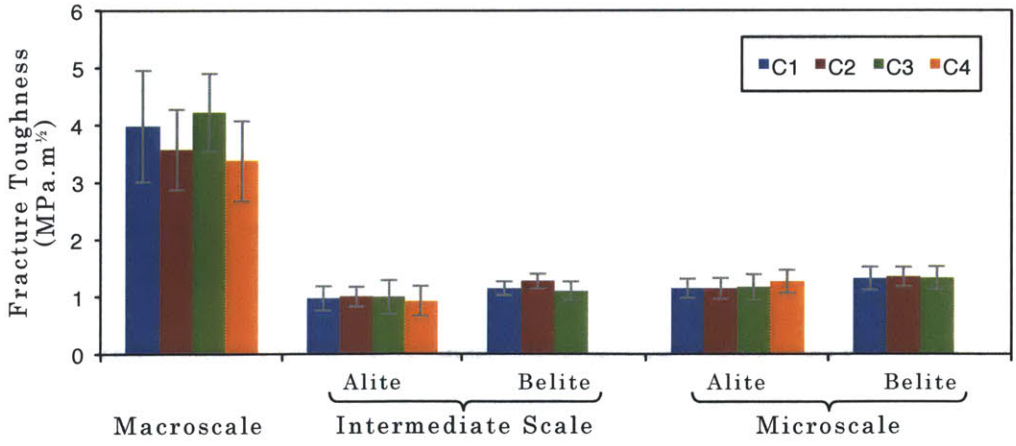

Fig. 10.13. Summary of the multi-scale investigation of fracture toughness for the four studied clinkers (*C1*, *C2*, *C3* and *C4*). Alite and belite were investigated separately at the intermediate and micro scales, but jointly at the macroscale.

The macroscale fracture toughness measured for clinker C2 and C4 were lower than those of clinkers C1 and C4. At the intermediate scale, the alite-rich regions for all the clinkers had similar toughness, with an average value slightly lower than that of the belite-rich regions. Scratch imprints at the intermediate scale were analyzed to investigate crack propagation patterns. Cracks were found to occur mainly in alite grains and at the interfaces, whereas belite grains and interstitial phases were much less affected. At the microscale, probing of single grains allowed determination the intrinsic fracture toughness. The measured toughness for alite crystals was ~1.2 ± 0.2 MPa.m^{½}, which is in agreement with previously published values. The difference in magnitude observed between the results at the macroscale and at smaller scales are further discussed in the next chapter.

Chapter 11

Discussion

In the previous chapters, a comprehensive characterization of the studied clinkers has been presented with respect to microstructure, bulk mineralogy, bulk chemistry, phase chemistry and fracture properties. This chapter combines and further explores these results. The grinding energy is first estimated from the macroscale fracture toughness. Then, the variations on fracture results over the probed scales are explored with respect to toughening mechanisms. Finally, the particularities of each clinker are highlighted to establish links between fracture properties and chemo-microstructural characteristics.

11.1 From Fracture Toughness to Grinding Energy

The macroscale fracture toughness measured on clinkers is used to provide a rough approximation of the grinding energy, E_G, as a function of the Blaine specific surface, S. The fracture energy, G_f, is considered the energy required to create surfaces, with some energy dissipated as heat. A first order approach based on LEFM is used to predict the grinding energy employed to create these surfaces:

$$G_f = K_c^2/E \tag{11.1}$$

$$E_G = S * G_f = S * K_c^2/E \tag{11.2}$$

where the Young modulus of clinker, E = 100 GPa [9]. Fig. 11.1 presents the results of this first order approximation for the four studied clinkers, along with experimental grinding energies measured in laboratory by other authors [125,123]. A comparison of these results illustrates the magnitude of the losses in the grinding process. According to the above calculations, the energy required to create the surfaces of the cement particles ranges between one-fourth and one-half of the energy provided experimentally during grinding (for

the Blaine specific surface typical of normal industrial cement, i.e., below 380 m²/kg [14]). Thus, the majority of the grinding energy is lost as heat and inefficiency. The losses are also accentuated in the fine grinding (for higher Blaine values), as shown by the exponential increase of the experimental grinding energy. The agglomeration tendency of the smaller particles can explain this behavior. A reduction in energy efficiency also occurs for small particles which are less prone to cracking and exhibit a more plastic behavior [98].

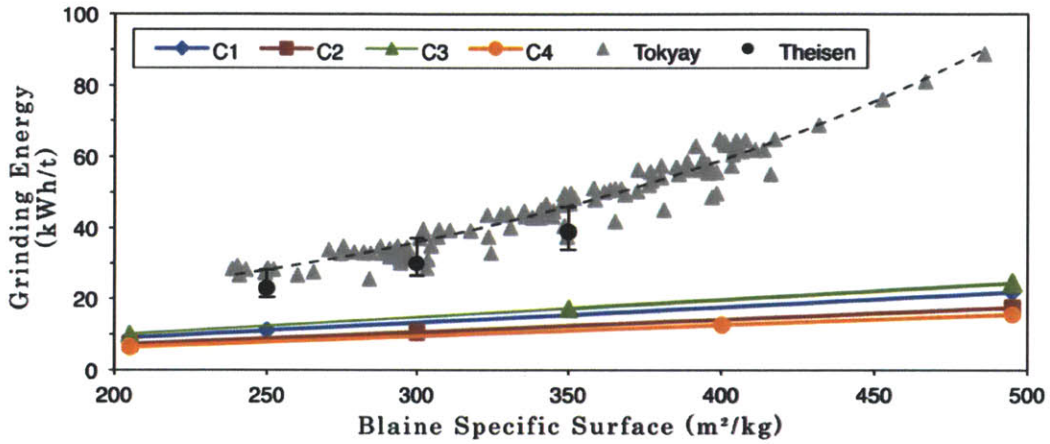

Fig. 11.1. Grinding energy as a function of the Blaine specific surface. The figure presents the LEFM first order approximation obtained for the studied clinkers, along with experimental reference data from Tokyay [125] (results from 15 types of clinkers) and from Theisen [123] (average, minimum and maximum grinding energy measured on 23 types of clinkers).

11.2 Fracture Toughness over the Scales

As presented in Chapter 10, the fracture toughness measured at the microscale was slightly higher for belite crystals than alite crystals. The measurements were performed on single grains, and the results were considered as the intrinsic K_C for each phase. The microscale toughness for each phase did not vary significantly from a clinker type to the other, and very similar results were obtained when probing a few grains at the intermediate scale. This suggests that the grindability of different clinkers is not characterized by the intrinsic fracture toughness of crystals, but rather by the microstructural particularities of the combined phases. The macroscale measurements account for these particularities, and show larger variations in the results.

In addition, the macroscale fracture toughness was higher than the toughness of single crystals by a factor of four. This toughening effect of the microstructure is not uncommon, particularly in the ceramics science. As an example, composite materials reaching ~20 MPa.m$^{1/2}$ were obtained by a combination of glass-ceramics (~1 MPa.m$^{1/2}$) and polycrystalline SiC (~2 MPa.m$^{1/2}$) [134]. In fact, the need for high-toughness ceramics triggered the investigation of different toughening mechanisms such as crack deflection, crack front roughening, crack trapping, crack bridging, particle pull out and microcracking. Since several mechanisms may occur simultaneously, single toughening mechanisms are generally investigated based on theoretical developments and idealized systems. The following sections present the mechanisms likely to occur in clinker.

11.2.1 Crack Tip Deflection

In polycrystalline brittle materials, crack propagation planes are deviated by the presence of heterogeneities such as grain boundaries or particles of a second phase, as illustrated in Fig. 11.2a. These deflections of the crack planes reduce the stress at the crack tip, when the new orientation is unfavorable to the external stress field. In order for the fracture to propagate, higher external stress must then be applied and this increases the effective fracture toughness, K^{∞}.

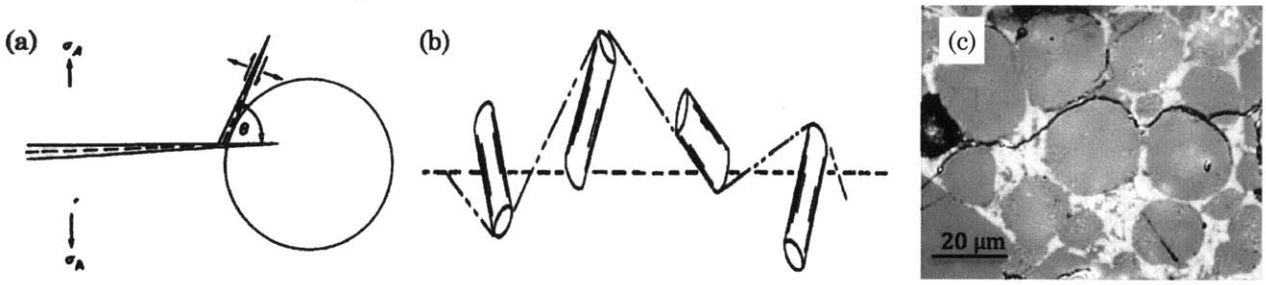

Fig. 11.2 (a) Schematic of a crack tilt upon contact with a second phase particle. (b) Schematic of a crack twist around randomly oriented rods. (c) Crack deflection following weak interfaces around the belite grains, as observed in clinker C3.

Faber and Evans [33,34] investigated this toughening phenomenon for systems composed of a matrix incorporating randomly located heterogeneities (rods, discs and spheres), as schematized in Fig. 11.2b. A toughening of $K^{\infty} \approx 2K_c$ was obtained for rods with high aspect ratio, and it was found that the toughening was dependent on the shape and density of the heterogeneities, but not on their size. Weiderhorn [134] suggested that similar toughening

must apply to normal equiaxed polycrystalline ceramic material, as is the case for aluminum oxide with polycrystalline K^{∞} of 4-5 MPa.m$^{1/2}$ compared to single-crystal K_c of 2.2 MPa.m$^{1/2}$ on the (1010) plane.

At the macroscale, clinker is a complex brittle material composed of large alite and belite crystals, and filled with much smaller crystals of the interstitial phases. Upon fracture, cracks tend to propagate in alite crystals and at the boundaries between the different phases (see section 10.2), which results in deflected crack planes as illustrated in Fig. 11.2c. Therefore, crack deflection is likely to contribute to the increased effective toughness observed for clinkers at the macroscale.

11.2.2 Crack Tip Shielding by Microcracks

Crack tip shielding occurs when compressive forces develop between the cracks' surfaces through the boundary of a process zone, as illustrated in Fig. 11.3a. Different mechanisms can be responsible for this process zone, such as plastic deformation, polymeric transformation or microcracking. In the latter case, microcracks nucleate around the principal crack because of the thermoelastic anisotropy of the surrounding material [101,31]. During the stress build-up in front of the crack tip, microcracks propagate in zones of localized residual tensile stress and stop in zones of residual compression. As suggested by Evans and Faber [31], the toughening associated with microcracking is mainly caused by the volumetric dilatation of the microfractured zone, with a small contribution from the reduction of the elastic modulus.

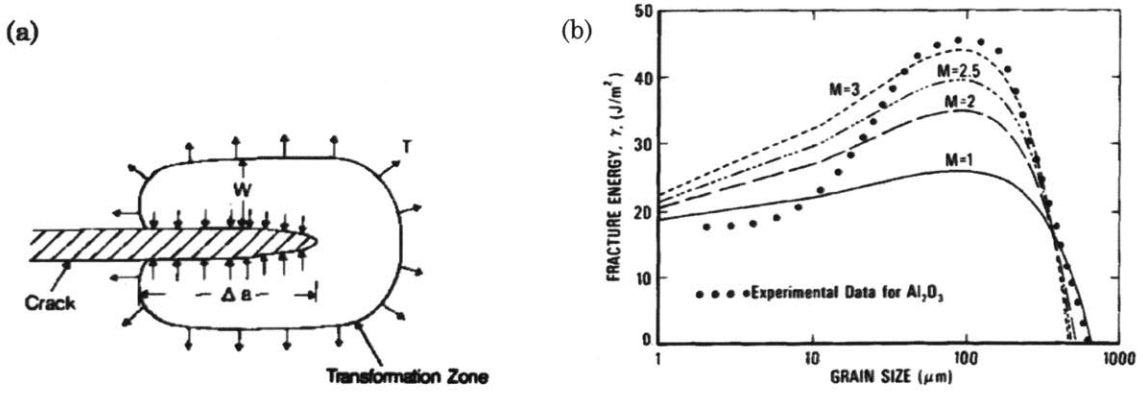

Fig. 11.3 (a) Crack tip shielding by a process zone surrounding the crack [79]. (b) Fracture energy as a function of grain size for aluminum oxide ceramics, by Rice and Freiman [100]. The model developed by the authors is fitted to experimental literature data.

Rice and Freiman [101,100] developed a model based on microcracking to explain the variation of fracture toughness as a function of the grain size. Fig. 11.3b presents their results for aluminate oxide ceramics. According to the authors, the increase of the toughening is due to the proportional increase of thermoelastic stresses with the grain size, up to a critical size where the residual stresses exceed the local strength of the material. For larger grains, the microcracking occurs during the production process, which limits the toughening phenomenon.

A different approach was pursued by Shum and Hutchinson [110], who considered the stress redistribution occurring directly from the interaction of the main crack with the nearest one or two microcracks. The authors determined the optimal configurations for the microcracks (Fig. 11.4a) and calculated a maximal theoretical toughening of $K^{\infty} \approx (1.4\ to\ 1.7)K_c$. The representativeness of this local solution over a crack front with several microcracks is left as an open issue by the authors.

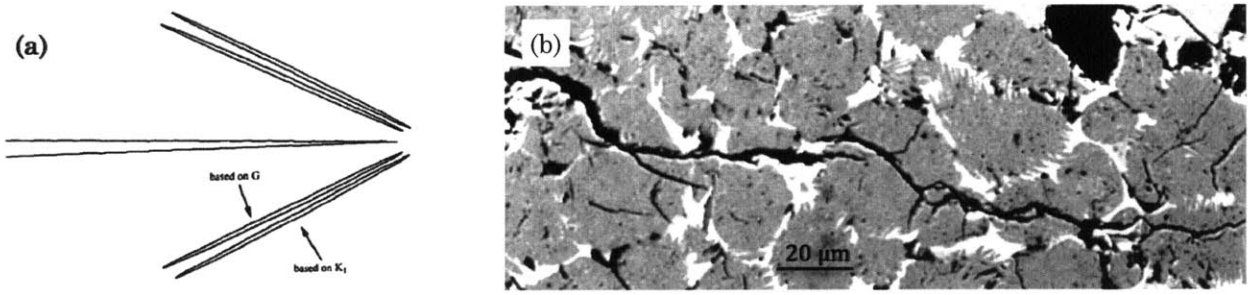

Fig. 11.4. (a) Optimal configuration for maximum toughening with two microcracks, as determined by Shum and Hutchinson [110]. (b) SEM micrograph of clinker C1 showing the presence of microcracks around a principal crack.

In the case of clinkers, quenching and crystallization of the interstitial phase (see section 2.1.2) introduces residual stresses into the multiphase microstructure. In addition, propagation of cracks in clinkers is associated with the creation of microcracks along the main crack paths, as illustrated in Fig. 11.4b. Thus, shielding by microcracks is a potential mechanism contributing to the toughening measured for clinkers at the macroscale.

11.2.3 Crack Trapping and Crack Pinning

Crack trapping occurs when the crack propagation front is deformed by the presence of heterogeneities with higher toughness. As shown in Fig. 11.5a, a semi-infinite crack

propagates uniformly until part of the crack reaches the particle of higher toughness. As the load is increased, the crack bows around the tough particle to satisfy the propagation criterion $K \leq K_c$ simultaneously for the matrix and the tough particle. Gao and Rice [41] investigated this behavior with a linear perturbation scheme and they determined a first-order solution for the crack front shape and the toughening ratio $\bar{\sigma} = K^{\infty}/K_c$ (K_c is the intrinsic toughness of the matrix and K^{∞} is the effective toughness). Different configurations of tough particles were tried, and the example shown in Fig. 11.5b was found to increase toughness by 1.87 (the tough particles have twice the toughness of the matrix).

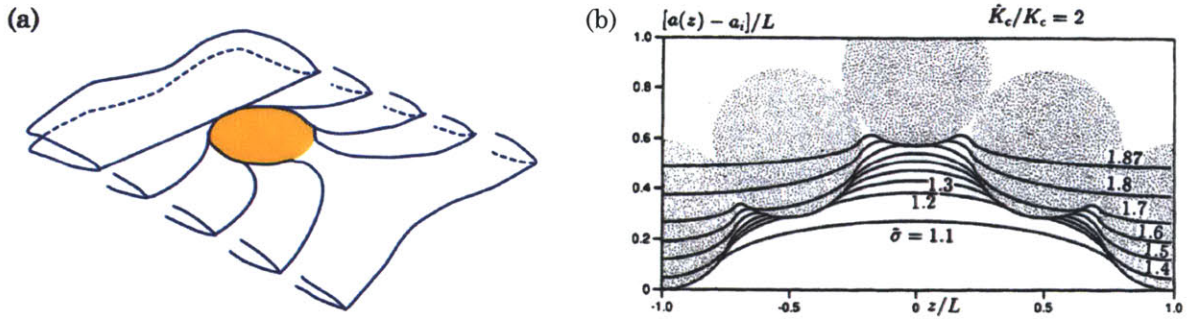

Fig. 11.5. (a) Schematic of crack bowing around a particle with higher toughness, courtesy of Laurent Brochard and inspired from [16]. (b) Crack front shape and toughening ratio $\bar{\sigma}$ for a specific configuration investigated by Gao and Rice [41].

Bower and Ortiz [16] further refined the method in a three-dimensional analysis that also included crack pinning. Crack pinning takes place in continuation of crack trapping, when the toughness of the particles exceeds a critical value. In this case, the particles are not penetrated by the crack front, which bows further until the crack joins up on itself, leaving pinned particles behind. A strong bond between the matrix and the particles reduces the stress on the crack front because the bridging particles carry part of the load (until the crack eventually penetrates the particle). In contrast, an interface weaker than the bridging particles causes particles pullout, which is associated with the development of frictional forces between the particles and the matrix.

Bower and Ortiz [16] investigated these toughening mechanisms by idealizing a reinforced material with an elastically homogeneous solid containing a regular distribution of tough circular particles. As presented in Fig. 11.6a, their results for perfectly bonded particles indicate that a combination of crack trapping and pinning increases the effective toughness up to $K^{\infty} \geq 5K_c$ (depending on the particles toughness and their relative size). The

maximum contribution of crack trapping (without any bridging particle) is around $K^{\infty} = 2K_c$ in the case of unstable crack penetration of the tough particles. The authors also investigated the pullout case, and they found that the frictional bridging toughening was limited to 20-30%.

These analyses were also validated with experimental results. The combination of crack trapping and pinning is thus a plausible explanation for the toughening observed in polycrystalline materials. However, in the case of single-phase ceramics, the origin of the tough regions assumed in the previous analysis is not clear. However, the thermal and elastic anisotropy of the grains creates compressive residual stresses in some of the grains. Evans et al. [32] suggested that these pre-stressed grains are less likely to be fractured and they can act as bridging particles.

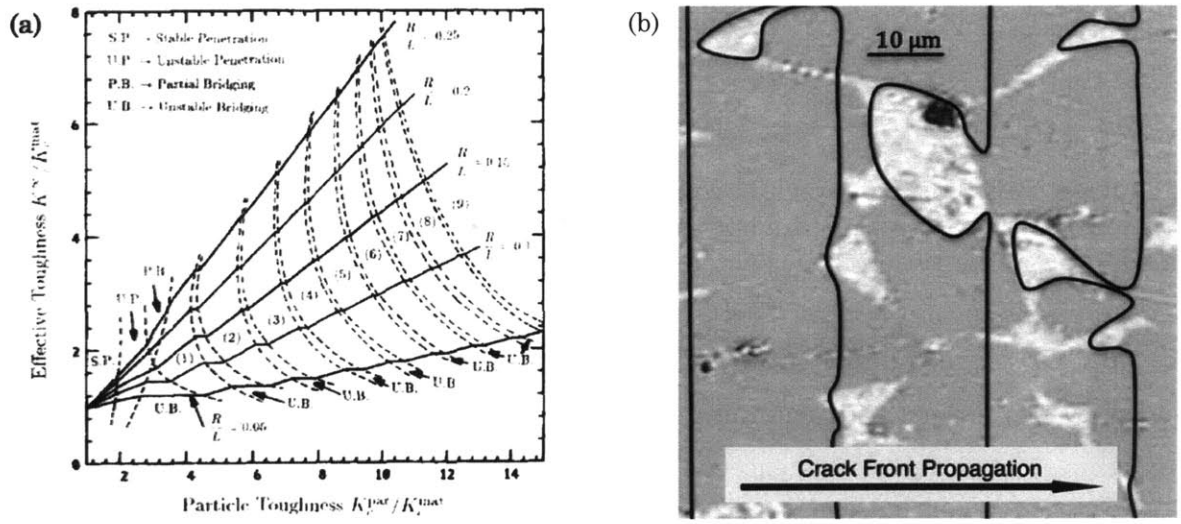

Fig. 11.6. (a) Results by Bower and Ortiz [16] for crack trapping and pinning with perfectly bonded particles. The effective toughness is plotted as a function of the pinning particle toughness and its volume fraction (parameterized with the ratio of the particle radius R over the particle spacing L). (b) Schematic of potential crack trapping and pinning in clinkers. The crack front propagates in the alite crystals (dark gray regions), bowing around the interstitial phases (light gray regions) and leaving pinning regions behind.

Clinkers are obviously more complex than the idealized model previously presented. However, the occurrence of the same mechanisms may be hypothesized, as conceptually schematized in Fig. 11.6b. In the case of clinkers, the alite crystals are considered as the matrix and the interstitial phases (aluminate + ferrite) as the tough particles. This is a reasonable assumption, considering that the toughness of the aluminate phase is roughly

twice that of alite, and the ferrite phase is estimated to be tougher, according to measurements by Hornain and Regourd [53] (see section 2.1.2).

Overall, the toughening observed for clinkers from the microscale to the macroscale was explained by the combination of crack deflection, crack tip shielding by microcracks, crack trapping and crack pinning. The quantitative evaluation of these toughening mechanisms applied to the fracture of clinkers is not pursued in this study, but this would be an interesting research direction.

11.3 Linking Fracture Properties to Clinker Characteristics

This section recalls the principal particularities of each clinker in order to interpret the differences in macroscale fracture toughness observed between the studied clinkers. The links between microstructure and fracture behavior are determined based on the existing knowledge (Chapter 2) and the toughening mechanisms previously presented. In addition, possible manufacturing conditions responsible for the given particularities are presented based on the published observations compiled by Campbell [22].

11.3.1 Clinker C1

Clinker C1 generally showed average characteristics, in comparison with the other studied clinkers. Nevertheless, it was the only clinker containing ragged belite crystals with extension of "fingers" into the matrix, as illustrated in Fig. 11.7.

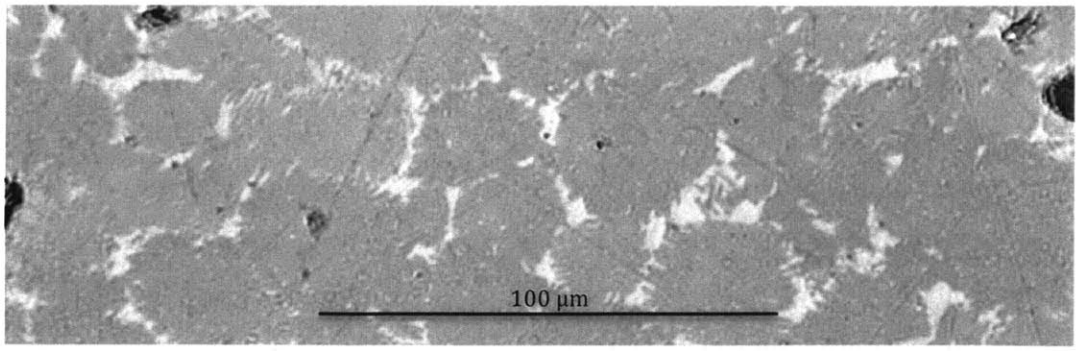

Fig. 11.7. Optical micrograph of clinker C1 showing a cluster of ragged belite crystals with extension of "fingers" into the matrix.

This type of belite is characteristic of the extension of the burning zone farther back in the kiln, which results in a slower cooling allowing the growth of these "fingers", as described by Ono, Krämer, Gilles *et al.*, cited in [22]. In addition, the macroscale fracture toughness is relatively high for clinker C1. A potential explanation is that the belite "fingers" increase the toughness of the interfaces between belite grains and the interstitial phases.

11.3.2 Clinker C2

Clinker C2 exhibits low macroscale fracture toughness (i.e., low coarse grinding energy), which was attributed to its elevated porosity. Porosity reaches 33% for this clinker, in comparison to 12-25% for the other clinkers (see section 7.2). The crack propagation in a porous medium occurs by connection of the pores, resulting in a reduced effective toughness.

The elevated porosity of clinker C2 is characteristic of poorly burned clinkers, as observed by Ono, Gilles *et al.*, Törnebohm and Hofmänner, cited in [22]. Belite content is also the highest of the studied clinkers, with 20% of the crystalline phases. This increased presence of belite is not due to the raw mix proportioning (the modified lime saturation factor LSF^* is sufficient with 1.06), but is rather another consequence of the insufficient burning. In addition, belite crystals are agglomerated in clusters which are harder to grind than individual belite grains, and play an important role in fine grinding [74]. Thus, even if the high porosity improves the coarse grindability, the overall grindability is expected to be low because of the belite nests [22].

11.3.3 Clinker C3

Clinker C3 is characterized by the highest macroscale fracture toughness, which was attributed to an increased contribution of the microcracking toughening. As previously described, the intensity of this toughening mechanism increases with grain size (up to a certain extent) and clinker C3 exhibits oversized alite crystals of the polymorphic type M_1, as illustrated in Fig. 11.8. Other authors, such as Tachihata *et al.* cited in [22], also observed elevated grinding energy for clinkers with large crystals.

The oversized crystals are associated with an elevated SO_3 content (1.6 wt% for this clinker). This SO_3 favor low supersaturation of the melt and lower viscosity, which then results in lower intensity of nucleation leading to unstable growth of larger alite crystals of the polymorph M_1 [108,109]. As cited in [22], Strunge *et al.* observed an increase by a factor

three in the alite crystal size associated with a change in SO_3 content from 0% to 2.6%. In the case of clinker C3, the oversized alite crystals are larger than 150 μm.

Another particularity of clinker C3 is the elevated alite-to-belite ratio. Thus, even if the coarse grinding energy is increased because of the crystal size, the fine grinding may require less energy than for clinkers C1 and C2, which exhibits higher contents of belite clusters.

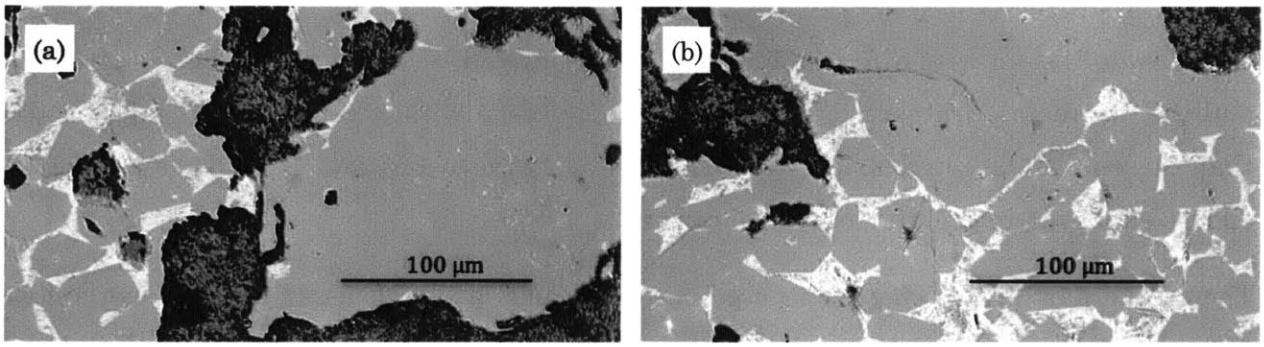

Fig. 11.8. Optical micrograph of clinker C3 showing the oversized alite crystals and the ferrite-dominated interstitial phase.

11.3.4 Clinker C4

Clinker C4 is the only clinker with low porosity (12%) and homogeneous repartition of the silicates, as illustrated in Fig. 11.9. This is an ideal clinker structure, generally associated with good production conditions, as described by Campbell [22]. Clinker C4 is also the clinker with the lowest macroscale fracture toughness. In contrast to clinker C3, the alite crystals of clinker C4 are small. Thus, a potential explanation for the inferior toughness is the reduced contribution of crack tip shielding by microcracks because of small crystal size.

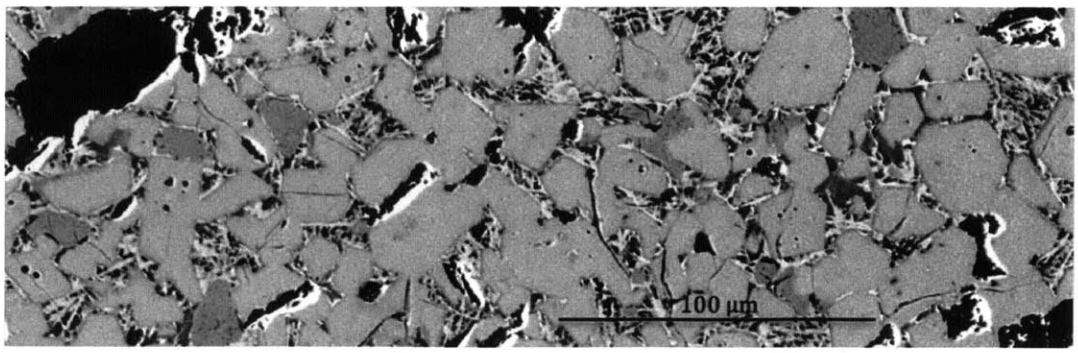

Fig. 11.9. SEM micrograph of clinker C4 showing the good repartition of the belite grains into the alite-dominated clinker matrix.

In addition, the absence of belite clusters certainly contributes to improving both the coarse and fine grindability. Also, it is interesting to note that clinker C4 comes in the form of large nodules and that the alite crystals are not microcracked. These two characteristics are usually expected to reduce grindability [22], but this was not dominant for clinker C4 at the macroscale.

11.4 Chapter Summary

This chapter began with a first order approximation of the grinding energy based on LEFM and the macroscale fracture toughness. The comparison with experimental results showed that the energy required to create surfaces was between one-fourth and one-half of the energy employed in grinding of typical cement.

The second part of this chapter focused on toughening mechanisms, in order to explain the difference between the macroscale fracture toughness and the intrinsic fracture toughness (measured at the microscale). Crack deflection is a first mechanism, which could occur in clinker because of weak interfaces. These weak paths can redirect the cracks in orientations less favorable to fracture and this reduces the stress field at the crack tip. Theoretical studies of this mechanism proposed potential toughening up to $K^{\infty} \approx 2K_c$ [33,34]. Crack tip shielding by microcracks can also be applied to clinkers, as quenching creates the residual tensile stresses necessary to generate a dilatational process zone around the crack tip. Microcracking was found to be dependent on the grain size [100], and discrete modeling of microcracks suggested possible toughening of $K^{\infty} \approx [1.4, 1.7]K_c$ [110]. Crack trapping occurs when a crack front bows around particles of higher toughness. Crack pinning follows trapping when the particle has sufficient toughness to be completely contoured by the crack front. Analytical modeling [16] showed maximum toughening on the order of $K^{\infty} \approx 2K_c$ for trapping only, and up to $K^{\infty} \geq 5K_c$ for the combination of trapping and pinning. In clinkers, the interstitial phases could hypothetically form the tough particles as the crack front propagates in the alite matrix. The combination of these four toughening mechanisms was suggested to explanation the higher toughness values obtained for clinkers at the macroscale compared to the microscale.

The last section of this chapter recalled the microstructural particularities of the studied clinkers and linked them with the fracture properties and potential manufacturing

conditions. The lower macroscale fracture toughness measured for clinkers C2 and C4 was associated with microstructural characteristics obtained with opposite burning conditions: (1) excessive porosity of clinker C2 caused by poor burning, or (2) good repartition of small-sized silicates of clinker C4 associated with good burning conditions. In addition, the oversize of alite crystals in clinker C3 was linked to the highest macroscale toughness of this clinker. An explanation for this behavior was the increased microcracking toughening occurring with larger grain size.

The macroscale toughness was associated with coarse grindability and the fine grindability was linked to properties of single crystals. The microscratch test measurements at the intermediate and micro scales showed that belite clusters and belite crystals had higher fracture toughness than their alite counterparts. Thus, the fine grinding energy of clinker C4 was expected to be the lowest because it was the only clinker generally free of belite clusters. In contrast, clinker C2 was expected to require the highest fine grinding energy because of its highest belite content and the presence of belite clusters.

Part IV

Conclusions

Chapter 12

Summary of Results and Perspectives

At the onset of this investigation, the following research question was formulated: how are chemistry, mineralogy and microstructure of cement clinkers related to fracture properties at the different characteristic scales? This research progressively developed the answer by achieving the objectives, which were (1) to characterize the microstructure of industrial clinkers with respect to the characteristic scales and particularities of the constituting crystals; (2) to investigate average chemistry and mineralogy of industrial clinkers, as well as chemistry of the constituting phases; and (3) to adapt the microscratch test method for the investigation of fracture properties of heterogeneous industrial clinkers at their different characteristic scales. This final chapter summarizes the work performed emphasizing the main findings and the research contributions, along with the future directions and the benefits for the industry.

12.1 Summary of Main Findings

In this study, the following findings emerged from the comprehensive characterization performed on the four studied industrial clinkers:

- Three characteristic scales describe cement clinkers: at the macroscale (10^{-1}, 10^{-2} m) clinkers are constituted of nodules; at the intermediate scale (10^{-3}, 10^{-4} m) the nodules are separated into porosity and matrix; and at the microscale (10^{-5}, 10^{-6} m) the clinker matrix is composed by the clinker phases.

- The non-quantified content can represent a significant proportion of cement clinkers. In addition to the crystalline phases quantified by X-ray diffraction, around 10-20% of the studied clinker was measured to be amorphous content (and possible error of the method). This is of the same magnitude as the belite and ferrite contents.

- Belite clusters and belite crystals tend to have higher fracture toughness than their alite counterparts, as measured with the microscratch tests performed at the intermediate scale and microscale. In addition, investigations of crack propagation patterns around scratch paths showed that cracks propagate generally in alite grains and at the interfaces, whereas belite grains and interstitial phases are more frequently contoured.

- Significant losses in heat and inefficiency occur in the grinding process. The energy required to create the surfaces of the cement particles was determined with a first order approximation using LEFM and the measured macroscale fracture toughness. The results were two to four times lower than experimental grinding energies.

- The grindability of clinkers depends on the microstructural arrangement of the phases. Similar results were observed for the studied clinkers regarding the intrinsic toughness of each phase, both for alite and belite. In contrast, results at the macroscale showed larger differences between clinkers. In addition, the toughness at the macroscale was three to four times higher than the intrinsic toughness, which was explained by a combination of toughening mechanisms, i.e., crack deflection, crack tip shielding by microcracks, crack trapping, and crack pinning.

- Lower macroscale fracture toughness (i.e., lower coarse grinding energy) was associated with either poorly burned clinkers showing excessive porosity or well burned clinkers having a good repartition of small-sized silicates. However, difficulties in fine grinding were expected for the poorly burned clinkers because of the increased amounts of clustered belite. In contrast, higher macroscale toughness (i.e., higher coarse grinding energy) was associated with oversized alite crystals dominated by the polymorph M_1 (formed in presence of high SO_3 content). A possible explanation for the elevated toughness is that the microcracks toughening increases with the grain size (up to a certain extend).

12.2 Technical Contributions

In the process of clinker characterization, several experimental methods were implemented, adapted, and improved. The two major contributions to these methods follow:

- *The extension of the statistical electron-probe microanalysis (EPMA) method for complete chemical and mineralogical characterization of clinkers.* In addition to the multivariate clustering previously developed for identification of the distinct phases and their average composition, the implementation of the law of mixtures on each data point enabled the retrieval of the relative abundance of the identified phases. The validity of this approach was validated for industrial clinkers with quantitative X-ray diffraction and X-ray fluorescence.

- *The scaling of the microscratching method to reduce the scratch length from the initial 3 mm down to 20 μm.* The multi-scale fracture toughness investigation of clinkers triggered this downscaling, which required adjustment of the experimental protocol and validation with reference materials. In addition, improvements of the microscratching experimental procedure are proposed with respect to adequate sample holding and moisture control of the Lexan reference material.

12.3 Industrial Benefits

This work employed industrial clinkers to represent the industrial reality and to facilitate technology transfer. Thus, the statistical EPMA method has a potential for transfer to the cement industry, since it could be used for quality control at cement plants to provide simultaneously the bulk chemistry, the chemistry of the phases and their abundance. The characterization resulting from this single experiment would be equivalent to the information obtained from three independent tests.

At the same time, the cement industry is looking for ways to increase the efficiency of its clinker grinding processes. Thus, the industry can potentially use the microscratching method and the findings of this study to optimize clinker production for efficient grinding.

12.4 Limitations and Perspectives

The work performed in this research recognizes some limitations, which are also directions for further investigations. The statistical EPMA testing required with the proposed method is a relatively long process. However, the energy dispersive spectrometry (SEM-EDS) provides a rapid alternative to obtain equivalent measurements, which can be treated with the exact same method. In addition, the phase quantification does not yet distinguish

between the interstitial phases, and this limitation could be solved by extension of the phase repartition model, developed in this study, to an additional dimension.

The implementation of the microscratching method to clinkers is limited by their complex microstructure (i.e., large pores and limited available bulk surfaces). Scale separability could not be met for the macro and intermediate scales, and the results are thus considered as local fracture responses. Also, the hypothesis was made that scale separability and the Buckle's rule-of-thumb are valid for the microscratch method. Verification of this hypothesis is of interest for future research.

Finally, the relations established in this study, between clinker particularities and fracture toughness at the different scales, provide valuable information which further work could strengthen. This work includes the investigation of additional clinkers types and the use of conventional grindability measurements (e.g., Bond workability), both of which were not possible in this study. In addition, the proposed toughening mechanisms qualitatively explain the difference in magnitude between the macroscale fracture toughness and the intrinsic toughness of single crystals. Additional work is needed to obtain quantitative understanding of these toughening mechanisms applied to clinker.

12.5 Conclusion

In conclusion, this study proposes alternative approaches for clinker analysis with respect to characterization and grinding. Even though the proposed methods may need additional refinement before field implementation, there is good potential for applications as part of quality control in cements plants. Such an eventuality would be of great interest, as a fast growing database could be used to establish further links between the microstructure, chemistry, mineralogy and fracture properties of cement clinkers.

Bibliography

[1] Abuhaikal M. and Ulm F.-J. (2011). *Nano-ChemoMechanical Assessment of Rice Husk Ash Cement by Wavelength Dispersive Spectroscopy and Nanoindentation*, Masters Thesis, Massachusetts Institute of Technology, Department of Civil and Environmental Engineering, Cambridge, MA.

[2] Accuratus (2002). Ceramic Materials and Ceramic Components: Material Characteristics. Available: http://www.accuratus.com.

[3] Akono A.-T. (2012). Personal Communication.

[4] Akono A.-T., Randall N.X., and Ulm F.-J. (2012). Experimental determination of the fracture toughness via microscratch tests: Application to polymers, ceramics, and metals. *Journal of Materials Research*, 27(2): 485–493.

[5] Akono A.-T., Reis P.M., and Ulm F.-J. (2011). Scratching as a Fracture Process: From Butter to Steel. *Physical Review Letters*, 106(20): 204–302.

[6] Akono A.-T. and Ulm F.-J. (2012). Fracture scaling relations for scratch tests of axisymmetric shape. *Journal of the Mechanics and Physics of Solids*, 60(3): 379–390.

[7] Akono A.-T. and Ulm F.-J. (2011). Scratch test model for the determination of fracture toughness. *Engineering Fracture Mechanics*, 78(2): 334–342.

[8] Armstrong J.T. (1995). CITZAF - A package of correction programs for the quantitative electron microbeam X-ray analysis of thick polished materials, thin-films, and particles. *Microbeam Analysis*, 4(3): 177–200.

[9] Armstrong J.T., et al. (2012). Quantitative X-Ray Microanalysis: Problem Solving Using EDS and WDS Techniques, Lecture Notes. *Lehigh Microscopy School.*

[10] ASTM International (2004). *Standard Specification for Portland Cement (ASTM Standard C150-04)*, West Conshohocken, PA, USA.

[11] ASTM International (2006). *Standard test method for determination of the proportion of phases in portland cement and portland-cement clinker using XRD analysis (ASTM Standard C1365-06)*, West Conshohocken, PA, USA.

[12] ASTM International (2000). *Standard Test Method for Fineness of Hydraulic Cement by Air-Permeability Apparatus (ASTM Standard C204-00)*, West Conshohocken, PA, USA.

[13] Bayles J. and Gouda G.R. (1981). Study of Clinker Grinding in a Ball Mill. In *Proceedings of the 3rd International Conference on Cement Microscopy*. 106–121.

[14] Bhatty J.I. and Tennis P.D. (2008). *U.S. and Canadian Cement Characteristics: 2004, PCA R&D SN2879*, Portland Cement Association.

[15] Bond F.C. (1961). Crushing and grinding calculations. *British Chemical Engineering*, 6: 378–385, 543–548.

[16] Bower A.F. and Ortiz M. (1991). A three-dimensional analysis of crack trapping and bridging by tough particles. *Journal of the Mechanics and Physics of Solids*, 39(6): 815–858.

[17] Brindley G. (1945). The effect of grain or particle size on x-ray reflections from mixed powders and alloys, considered in relation to the quantitative determination of crystalline substances. *Philosophical Magazine*, 36: 37–41.

[18] Buehler (2010). Quality At Work - Geological & Mineralogy Guide. Available: http://www.buehler.com/sites/default/files/resources/Geological-Mineralogy Guide.pdf.

[19] Burger W. and Burge M.J. (2008). Digital Image Processing: An Algorithmic Introduction Using Java, First Edition. *Texts in Computer Science*: 1–564.

[20] Bye G.C. (1999). *Portland cement: Composition, production and properties* 2nd ed., London: Thomas Telford Publishing.

[21] Callister W. (1994). *Materials science and engineering: an introduction* 3rd ed., New York; Chichester: Wiley.

[22] Campbell D.H. and Portland Cement Association (1999). *Microscopical examination and interpretation of portland cement and clinker*, Skokie, Ill.: Portland Cement Association.

[23] Celik I.B. and Oner M. (2006). The influence of grinding mechanism on the liberation characteristics of clinker minerals. *Cement and Concrete Research*, 36(3): 422–427.

[24] Cline J.P. and Von Dreele R.B. (1998). The Certification of SRMs 1878a and 1879a for Analysis of Quartz and Cristobalite Content. *Denver X-Ray Conference, Colorado Springs, CO.*

[25] Colville A.A. and Geller S. (1971). Crystal Structure of Brownmillerite, Ca2FeAlO5. *Acta Crystallographica Section B-Structural Crystallography and Crystal Chemistry*, B27: 2311–2315.

[26] Constantinides G, et al. (2006). Grid indentation analysis of composite microstructure and mechanics: Principles and validation. *Materials Science and Engineering A-Structural Materials Properties Microstructure and Processing*, 430(1-2): 189–202.

[27] Constantinides Georgios and Ulm Franz-Josef (2006). *Invariant Mechanical Properties of Calcium-Silicate-Hydrates (C-S-H) in Cement-Based Materials: Instrumented Nanoindentation and Microporomechanical Modeling*, Ph.D. Thesis, Massachusetts Institute of Technology, Department of Civil and Environmental Engineering, Cambridge, MA.

[28] Crumbie A., Walenta G., and Fuellmann T. (2006). Where is the iron? Clinker microanalysis with XRD Rietveld, optical micro scopy/point counting, Bogue and SEM-EDS techniques. *Cement and Concrete Research*, 36(8): 1542–1547.

[29] Dempster A.P., Laird N.M., and Rubin D.B. (1977). Maximum likelihood from incomplete data via the EM algorithm. *Journal of the Royal Statistical Society, Series B*, 39: 1–38.

[30] Drouin D., et al. (2007). CASINO V2.42 - A fast and easy-to-use modeling tool for scanning electron microscopy and microanalysis users. *Scanning*, 29(3): 92–101.

[31] Evans A. and Faber K. (1984). Crack Growth Resistance of Microcracking Brittle Materials. *Journal of the American Ceramic Society*, 67(4): 255–260.

[32] Evans A. G., Heuer A.H., and Porter D.L. (1977). The Fracture Toughness of Ceramics. In *Advances in Research on the Strength and Fracture of Materials. ICF4.* Waterloo, Canada, 539–556.

[33] Faber K.T. and Evans A G (1983). Crack deflection processes—I. Theory. *Acta Metallurgica*, 31(4): 565–576.

[34] Faber K.T. and Evans A G (1983). Crack deflection processes—II. Experiment. *Acta Metallurgica*, 31(4): 577–584.

[35] Fives FCB (2009). Some secrets of the Horomill (R) for efficient and smooth grinding. Available: www.fivesgroup.com/fivesFCB.

[36] Fraley C. and Raftery A.E. (2010). *MCLUST Version 3 for R: Normal Mixture Modeling and Model-Based Clustering*, Department of Statistics, University of Washington, Seattle, WA: Technical Report No. 504.

[37] Fraley C. and Raftery A.E. (1999). MCLUST: Software for model-based cluster analysis. *Journal of Classification*, 16(2): 297–306.

[38] Fraley C. and Raftery A.E. (2002). Model-based clustering, discriminant analysis, and density estimation. *Journal of the American Statistical Association*, 97(458): 611–631.

[39] François D., Pineau A., and Zaoui A. (2013). *Mechanical Behaviour of Materials - Volume II: Fracture Mechanics and Damage*, Dordrecht: Springer Netherlands.

[40] Frigione G., Zenone F., and Esposito M. V (1983). The Effect of Chemical-Composition on Portland-Cement Clinker Grindability. *Cement and Concrete Research*, 13(4): 483–492.

[41] Gao H. and Rice J.R. (1989). A first-order perturbation analysis of crack trapping by arrays of obstacles. *Journal of applied mechanics*, 56(4): 828–836.

[42] Genc O. and Benzer A.H. (2009). Single particle impact breakage characteristics of clinkers related to mineral composition and grindability. *Minerals Engineering*, 22(13): 1160–1165.

[43] Gobbo L. and Sant'Agostino L. (2009). *Aplicacao da difracao de raios-x e metodo de Rietveld no estudo de cimento Portland*. PhD Thesis, University of Sao Paulo, Institute of Geosciences, Sao Paulo, Brazil.

[44] Gogotsi G.A. (2003). Fracture toughness of ceramics and ceramic composites. *Ceramics International*, 29(7): 777–784.

[45] Goldstein J. (2008). *Scanning electron microscopy and x-ray microanalysis*, New York: Springer.

[46] Gouda G.R. (1979). Effect of Clinker Composition on Grindability. *Cement and Concrete Research*, 9(2): 209–218.

[47] Griffith A.A. (1921). The Phenomena of Rupture and Flow in Solids. *Philosophical Transactions of the Royal Society A Mathematical Physical and Engineering Sciences*, 221(582-593): 163–198.

[48] Harding D., Oliver W., and Pharr G. (1994). Cracking during nanoindentation and its use in the measurement of fracture toughness. *Materials Research Society Symposium Proceedings*, 356(1): 663–668.

[49] Heinrich K.F.J. and Newbury D. (1991). *Electron Probe Quantitation*, New York: Plenum Press.

[50] Hill A. and Agrawal C. (1990). Positron lifetime spectroscopy characterization of thermal history effects on polycarbonate. *Journal of materials science*, 25: 5036–5042.

[51] Hills L.M. (2007). *Clinker Microstructure and Grindability: Updated Literature Review*, Portland Cement Association, PCA R&D SN2967.

[52] Hills L.M. (1995). *The Effect of Clinker Microstructure on Grinding: Literature Review Database*, Portland Cement Association, PCA R&D SN2026.

[53] Hornain H. and Regourd M. (1980). Cracking and Grindability of Clinker. In *Proceedings of the 7th International Congress on the Chemistry of Cement*. I276–I281.

[54] Huang Q., et al. (1994). Neutron powder diffraction study of the crystal structure of HgBa2Ca4Cu5O12+Delta at room temperature and at 10 K. *Physica C: Superconductivity*, 227(1-2): 1–9.

[55] Impact Crushers (2011). Ball Mill, Ball Mill for sale in China, Ball Mill Cost & Price. Available: http://www.impact-crushers.com/grinding-machines/ball-mill.html.

[56] International Energy Agency (2009). Cement Technology Roadmap 2009. Available: http://www.iea.org/publications/freepublications/publication/Cement_Roadmap.pdf.

[57] Irwin G.R. (1957). Analysis of Stresses and Strains Near the End of a Crack Traversing a Plate. *Journal of Applied Mechanics, Transactions of ASME*, 24: 361–364.

[58] James M.N., et al. (2012). Fatigue crack growth and craze-induced crack tip shielding in polycarbonate. *Polymer*, 53(7): 1558–1570.

[59] Jansen D., et al. (2011). A remastered external standard method applied to the quantification of early OPC hydration. *Cement and Concrete Research*, 41(6): 602–608.

[60] Jansen D., et al. (2012). Does Ordinary Portland Cement contain amorphous phase? A quantitative study using an external standard method. *Powder Diffraction*, 26(01): 31–38.

[61] Jost K.H., Ziemer B., and Seydel R. (1977). Redetermination of Structure of Beta-Dicalcium Silicate. *Acta Crystallographica Section B-Structural Science*, 33: 1696–1700.

[62] Jupe A.C., et al. (2001). The site occupancy of Mg in the brownmillerite structure and its effect on hydration properties: an X-ray/neutron diffraction and EXAFS study. *Journal of Applied Crystallography*, 34: 55–61.

[63] Kawamura S., et al. (1982). The Estimation of Clinker Grindability by Microscopy (Ono method). In *CAJ Review of the 36th General Meeting, Technical Session.* 57–59.

[64] Knapen E., et al. (2009). Effect of free water removal from early-age hydrated cement pastes on thermal analysis. *Construction and Building Materials*, 23(11): 3431–3438.

[65] Kocaba V. (2009). *Development and evaluation of methods to follow microstructural development of cementitious systems including slags.* PhD thesis, Ecole Polytechnique Federale de Lausanne.

[66] Krakowiak K.J., Lourenço P.B., and Ulm Franz-Josef (2011). *Assessment of the mechanical microstructure of masonry clay brick by nanoindentation.* PhD Thesis, University of Minho, Civil Engineering Department, Braga, Portugal, and Massachusetts Institute of Technology, Department of Civil and Environmental Engineering, Cambridge, MA, USA.

[67] Kristmann M. (1978). Portland-Cement Clinker Mineralogical and Chemical Investigations: 2. Electron-Microprobe Analysis. *Cement and Concrete Research*, 8(1): 93–102.

[68] De la Torre A.G., et al. (2006). Quantitative phase analysis of ordinary Portland cements using synchrotron radiation powder diffraction. *Zeitschrift Fur Kristallographie*: 587–592.

[69] De La Torre A G, et al. (2002). The superstructure of C3S from synchrotron and neutron powder diffraction and its role in quantitative phase analyses. *Cement and Concrete Research*, 32(9): 1347–1356.

[70] De la Torre Á.G., et al. (2007). In situ synchrotron powder diffraction study of active belite clinkers. *Journal of Applied Crystallography*, 40(6): 999–1007.

[71] De la Torre A.G. and Aranda M A G (2003). Accuracy in Rietveld quantitative phase analysis of Portland cements. *Journal of Applied Crystallography*, 36: 1169–1176.

[72] De La Torre A.G., Bruque S., and Aranda M.A.G. (2001). Rietveld quantitative amorphous content analysis. *Journal of Applied Crystallography*, 34(2): 196–202.

[73] Liao W., Tanaka N., and Shintani H. (1993). Fracture toughness of porous-machinable-ceramic/resin composites prepared for dental applications. *Journal of Materials Science Letters*, 12: 457–458.

[74] Maki I., et al. (1993). Clinker grindability and textures of alite and belite. *Cement and Concrete Research*, 23(5): 1078–1084.

[75] Maki I., et al. (1992). Effect of MgO and SO3 on the Impurity Concentration in Alite in Portland-Cement Clinker. *Journal of the American Ceramic Society*, 75(11): 3163–3165.

[76] Maki I. and Goto K. (1982). Factors Influencing the Phase Constitution of Alite in Portland-Cement Clinker. *Cement and Concrete Research*, 12(3): 301–308.

[77] Manzano H., et al. (2011). Impact of Chemical Impurities on the Crystalline Cement Clinker Phases Determined by Atomistic Simulations. *Crystal Growth & Design*, 11(7): 2964–2972.

[78] McLachlan G.J. and Peel D. (2000). *Finite mixture models*, New York: Wiley.

[79] McMeeking R.M. and Evans A.G. (1982). Mechanics of Transformation-Toughening in Brittle Materials. *Journal of the American Ceramic Society*, 65(5): 242–246.

[80] Miller F.M. (1980). Dusty clinker and grindability problems. *Rock Products*, April: 152–157.

[81] Miller M., et al. (2008). Surface roughness criteria for cement paste nanoindentation. *Cement and Concrete Research*, 38(4): 467–476.

[82] Mitchell L.D., Margeson J.C., and Whitfield P.S. (2006). Quantitative Rietveld analysis of hydrated cementitious systems. *Powder Diffraction*, 21(2): 111–113.

[83] Mondal P. and Jeffrey J.W. (1975). Crystal-Structure of Tricalcium Aluminate, Ca3Al2O6. *Acta Crystallographica*, B31: 689.

[84] Mouton P.R. (2011). *Unbiased Stereology: A Concise Guide*, JHU Press.

[85] Mumme W.G., et al. (1995). Rietveld Crystal-Structure Refinements, Crystal-Chemistry and Calculated Powder Diffraction Data for the Polymorphs of Dicalcium Silicate and Related Phases. *Neues Jahrbuch Fur Mineralogie-Abhandlungen*, 169(1): 35–68.

[86] National Institute of Standards & Technology (2010). *Certificate of Analysis for Standard Reference Material 2688: Portland Cement Clinker*, Gaithersburg, MD 20899, USA.

[87] Nishi F. and Takeuchi Y. (1975). Al6O18 Rings of Tetrahedra in Structure of Ca8.5AaAl6O18. *Acta Crystallographica Section B-Structural Science*, 31: 1169–1173.

[88] Nishi F., Takeuchi Y., and Maki I. (1985). Tricalcium Silicate Ca3O[SiO4] - the Monoclinic Superstructure. *Zeitschrift Fur Kristallographie*, 172(3-4): 297–314.

[89] De Noirfontaine M.N., et al. (2006). Polymorphism of tricalcium silicate, the major compound of Portland cement clinker 2. Modelling alite for Rietveld analysis, an industrial challenge. *Cement and Concrete Research*, 36(1): 54–64.

[90] Ono Y. (1981). Microscopical Observation of Clinker for the Estimation of Burning Condition, Grindability and Hydraulic Activity. In *Proceedings of the 3rd International Conference on Cement Microscopy*. 198–210.

[91] Ono Y. (1995). *Ono's Method: Fundamental Microscopy of Portland Cement Clinker*, Ohsaku, Sakura, Chiba, Japan: Chichibu Onoda Cement Corporation.

[92] Opoczky L. and Gavel V. (2004). Effect of certain trace elements on the grindability of cement clinkers in the connection with the use of wastes. *International Journal of Mineral Processing*, 74: S129–S136.

[93] Opoczky L. and Mrakovics K. (1976). Role of Structure and The Chemical-Mineralogical Composition of Cement Clinker in Coarse and Fine Grinding. *Freiberger Forschungshefte A.*, (553): 71–81.

[94] Pecharsky V.K. and Zavalij P.Y. (2009). *Fundamentals of Powder Diffraction and Structural Characterization of Materials* Springer, ed., Springer US.

[95] Petersen I.F. (1980). The Pore Structure and Grindability of Clinkers. In *Proceedings of the 7th International Congress on the Chemistry of Cement*. 73–78.

[96] Port Plastics Polycarbonate Forming Guide. Available: http://www.portplastics.com/architect/page22.html.

[97] Posposil Z. (1979). The effect of clinker temperature on grindability. *Zement-Kalk-Gips*, 32(3): 49–51.

[98] Prasher C.L. (1987). *Crushing and Grinding Process Handbook*, Chichester, Great Britain: John Wiley & Sons Ltd.

[99] Rice J.R. (1968). A path independent integral and the approximate analysis of strain concentration by notches and cracks. *Journal of Applied Mechanics*, 35(2): 379–386.

[100] Rice R.W. and Freiman S.W. (1981). Grain-Size Dependence of Fracture Energy in Ceramics: II, A Model for Noncubic Materials. *Journal of the American Ceramic Society*, 64(6): 350–354.

[101] Rice R.W., Freiman S.W., and Becher P.F. (1981). Grain-Size Dependence of Fracture Energy in Ceramics: I, Experiment. *Journal of the American Ceramic Society*, 64(6): 345–350.

[102] SABIC Innovative Plastics (2009). Lexan* Sheet - Processing Guide. Available: http://www.mulfordplastics.com/_literature_77025/Lexan_Sheet_Processing_Guide.

[103] Le Saout G., Kocaba V., and Scrivener K. (2011). Application of the Rietveld method to the analysis of anhydrous cement. *Cement and Concrete Research*, 41(2): 133–148.

[104] Sarkar S.L. and Roy D.M. (1985). Electron-Microprobe Analyses of Nigerian Clinkers. *Cement and Concrete Research*, 15(4): 662–668.

[105] Scheubel B. (1985). Microscopically Determinable Parameters and their Relationship to Kiln System and Clinker Grindability. In *Proceedings of the 7th International Conference on Cement Microscopy*. 131–153.

[106] Schneider C.A., Rasband W.S., and Eliceiri K.W. (2012). NIH Image to ImageJ: 25 years of image analysis. *Nature Methods*, 9(7): 671–675.

[107] Schneider M., et al. (2011). Sustainable cement production-present and future. *Cement and Concrete Research*, 41(7): 642–650.

[108] Schreyer M., et al. (2011). Three approaches to total quantitative phase analysis of organic mixtures using an external standard. *Journal of Applied Crystallography*, 44(1): 17–24.

[109] Shanghai Shibang Machinery Co. Ltd. (2010). Cement grinding in a vertical roller mill. Available: http://www.iballmill.com/blog/cement-grinding-in-a-vertical-roller-mill/.

[110] Shum D.K.M. and Hutchinson J.W. (1990). On toughening by microcracks. *Mechanics of Materials*, 9(2): 83–91.

[111] Sorrentino F. (2011). Chemistry and engineering of the production process: State of the art. *Cement and Concrete Research*, 41(7): 616–623.

[112] De Souza V.C.G., et al. (2008). The influence of mineralogical, chemical and physical properties on grindability of commercial clinkers with high MgO level. *Cement and Concrete Research*, 38(8-9): 1119–1125.

[113] De Souza V.C.G., Koppe J.C., and Coimbra Leite Costa J.F. (2010). Effect of the foreign ions on Vickers micro-hardness of the crystalline phases in the co-processed clinkers. *Rem-Revista Escola De Minas*, 63(2): 299–306.

[114] Speakman S.A. (2010). Fundamentals of Rietveld Refinement, Lecture Notes. *Massachusetts Institute of Technology*. Available: http://prism.mit.edu/xray/tutorials.htm.

[115] Stanek T. and Sulovsky P. (2002). The influence of the alite polymorphism on the strength of the Portland cement. *Cement and Concrete Research*, 32(7): 1169–1175.

[116] Suherman P.M., et al. (2002). Determination of amorphous phase levels in Portland cement clinker. *Powder Diffraction*, 17(3): 178–185.

[117] Tavares L.M. (2004). Optimum routes for particle breakage by impact. *Powder Technology*, 142(2-3): 81–91.

[118] Tavares L.M. and Cerqueira M.C. (2006). Statistical analysis of impact-fracture characteristics and microstructure of industrial Portland cement clinkers. *Cement and Concrete Research*, 36(3): 409–415.

[119] Tavares L.M., Cerqueira M.C., and Less J.J. (2009). Analysis of the grinding behaviour of various Portland cement clinkers. *ZKG International*, 62(4): 95–103.

[120] Taylor D. (1984). Thermal-Expansion .4. Binary Oxides with the Silica Structures. *Transactions and Journal of the British Ceramic Society*, 83(5): 129–134.

[121] Taylor H.F.W. (1997). *Cement Chemistry*, London: Thomas Telford Publishing.

[122] Taylor H.F.W. (1989). Modification of the Bogue calculation. *Advances in Cement Research*, 2(6): 73–77.

[123] Theisen K. (1993). Estimation of cement clinker grindability. In *Proceedings of the 15th International Conference on Cement Microscopy*. 1–14.

[124] Titterington D.M., Smith A.F.M., and Makov U.E. (1985). *Statistical analysis of finite mixture distributions*, Chichester; New York: Wiley.

[125] Tokyay M. (1999). Effect of chemical composition of clinker on grinding energy requirement. *Cement and Concrete Research*, 29(4): 531–535.

[126] Tsurumi T., et al. (1994). Crystal structure and hydration of belite. *Ceramic Transactions*, 40: 19–25.

[127] U.S. Geological Survey (2010). Cement statistics, in Historical statistics for mineral and material commodities in the United States: U.S. Geological Survey Data Series 140 T. D. Kelly & G. R. Matos, eds. *Historical statistics for mineral and material commodities in the United States: U.S. Geological Survey Data Series 140.* Available: http://pubs.usgs.gov.libproxy.mit.edu/ds/2005/140/.

[128] Ulm F.-J., et al. (2007). Statistical indentation techniques for hydrated nanocomposites: Concrete, bone, and shale. *Journal of the American Ceramic Society*, 90(9): 2677–2692.

[129] Vandamme M., Ulm Franz-Josef, and Fonollosa P. (2010). Nanogranular packing of C-S-H at substochiometric conditions. *Cement and Concrete Research*, 40(1): 14–26.

[130] Velez K., et al. (2001). Determination by nanoindentation of elastic modulus and hardness of pure constituents of Portland cement clinker. *Cement and Concrete Research*, 31(4): 555–561.

[131] Venkateswaran D. and Gore V.K. (1991). Application of Microstructural Parameters to the Grindability Prediction of Industrial Clinkers. In *Proceedings of the 13th International Conference on Cement Microscopy*. 60–70.

[132] Viggh E.O. (1994). Estimation of grindability of portland cement clinker. *World Cement*, 25(10): 44–46,48,66–67,73–74.

[133] Whitfield P.S. and Mitchell L.D. (2003). Quantitative Rietveld analysis of the amorphous content in cements and clinkers. *Journal of Materials Science*, 38(21): 4415–4421.

[134] Wiederhorn S.M. (1984). Brittle Fracture and Toughening Mechanisms in Ceramics. *Ann Rev Mater Sci*, 14(10): 373–403.

[135] Winburn R., Lerach S., and Jarabek B. (2000). Quantitative XRD analysis of coal combustion by-products by the Rietveld method. Testing with standard mixtures. *Adv. X-ray Anal*, 42(C): 387–396.

[136] Wong H.S. and Buenfeld N.R. (2006). Monte Carlo simulation of electron-solid interactions in cement-based materials. *Cement and Concrete Research*, 36(6): 1076–1082.

[137] Wood M. and Weidlich J. (1982). Empirical Evaluation of Fracture Toughness: The Toughness of Quartz. *American Mineralogist*, 67(1964): 1065–1066.

[138] Young R.A. (1995). *The Rietveld Method* R. A. Young, ed., Oxford University Press.

[139] Zeisel H.G. (1953). Entwicklung eines Verfahrens zur Bestimmung der Mahlbarkeit. *Schriftenreihe der Zementindustrie*, 14: 31–72.